Dynamic Simulation of the Mitral Valve

Xingshuang Ma

School of Mathematics and Statistics

University of Glasgow

A thesis submitted for the degree of

Doctor of Philosophy

October, 2013

to mum and dad

Acknowledgements

The work in this PhD thesis was carried out at the School of Mathematics and Statistics at University of Glasgow, in Scotland, UK. It has been financially supported by China Scholarship Council studentship, fee waiver funding from the University of Glasgow and the Jim Gatheral scholarship for a three-months visit in New York University. All these support are gratefully acknowledged.

I would like to express my sincere and deep gratitude to Prof. Xiaoyu Luo for your supervision, support and for introducing me to the interesting field of bio-mathematics. I would like to express my deep and genuine gratitude to Prof. Boyce Griffith and Prof. Charles Peskin in New York University for your constant support and patience in helping me solve problems with IBAMR issues and your kindness during my stay in New York University. I am also very appreciated to Prof. Colin Berry and the cardiovascular imaging team in Institute of Cardiovascular and Medical Sciences for helping me obtain high resolution clinical images. I have learned a lot during these years, and without all your help I wouldn't be able to finish my work and thesis. Thank you all!

I would like to acknowledge Prof. David Fearn and Dr. Silvia Schievano

for agreeing to be examiner of this thesis and thank you for your precious advices and suggestions.

I especially want to acknowledge Dr. Hao Gao for sharing your skills and expertise in programming and image segmentation, and for all your help with correcting my thesis. Many thanks to all my friends and colleagues in all the fun things we had done in my PhD years.

Finally, I would like to thank my parents and my fiancé Jinnan, for your constant support, tolerance and selfless love.

Contents

List of Figures

Chapter 1

Introduction

Cardiovascular diseases are the leading cause of mortality in industrialized nations, including the United Kingdom and the United States. In 2007, cardiovascular disease accounted for 34% of deaths in the UK, totalling just over 193,000 people. When the functioning of a cardiac valve is sufficiently impaired, valve repair or replacement is required. Approximately 39,000 patients have cardiac surgery in the UK annually, among which heart valve operations are the second most common, behind only coronary bypass procedures. An improved understanding of human mitral valve biomechanics is urgent and important for the optimization of medical therapies and surgical procedures aimed at restoring normal mitral valve functioning in patients with valvular heart diseases.

1.1 Mitral Valve

The human mitral valve (MV) is a complex apparatus consisting of four components: a large antero-medial leaflet and a smaller postero-lateral leaflet, each

connected via multiple fibrous chordae tendineae to papillary muscles that are finger-like projections embedded into the underlying left ventricular myocardium, see Fig.1.1(a),(b).

The circumference of the heart valve attachment to the heart is referred to as the annulus, which is a saddle-shaped fibrous ring that seamlessly transitions into the two leaflets. The anterior leaflet is the biggest and taller leaflet that sits adjacent to the aorta, however, it's annulus length is smaller. It tucks under the posterior leaflet during closure pushing the posterior leaflet towards the outside of the valve Kunzelman et al. [1993]. The posterior leaflet is wider at the annulus but shorter in length. The chordae tendineae is a complex web of collagen chords that attach all over the leaflets of the mitral valve and tether to papillary muscles, which are believed to lengthen during iso-volumetric contraction and shorten during ejection as well as during iso-volumetric relaxation. The alignment of chordae tendineae and papillary muscles prevent the prolapse of the mitral valve leaflets at systole, and additionally assist in maintaining the geometry and functioning of the left ventricle. The mitral valve opens to allow blood to fill the left ventricle during diastole and early systole, and mitral valve closure regulates and prevents systolic regurgitation of blood from the left ventricle into the left atrium. This function requires the coordinated action of these interrelated components, and alterations in the structure or function of the leaflets, chordae, or papillary muscles may impede left ventricular filling, induce mitral regurgitation, and alter left ventricular function which may lead to eccentric ventricular hypertrophy, pulmonary oedema and, in instances of acute onset, the heart attack. Berdajs and Turina [2011]; Muresian [2009].

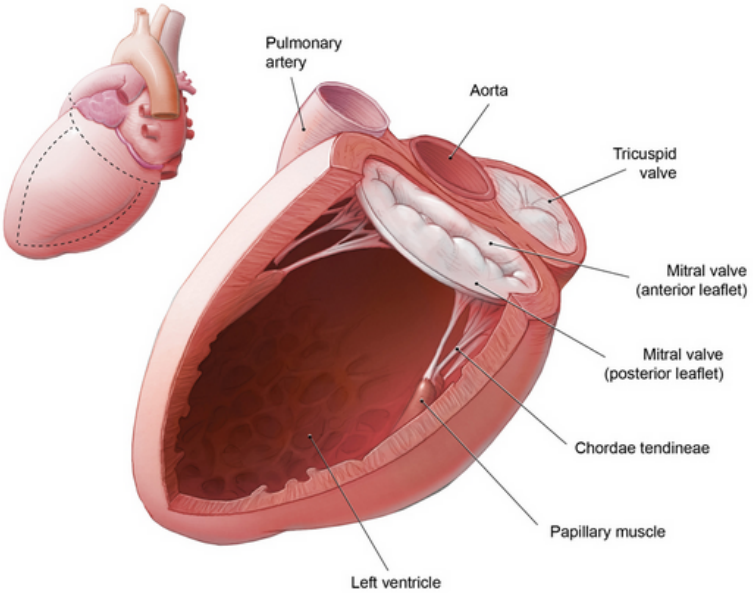

(a)

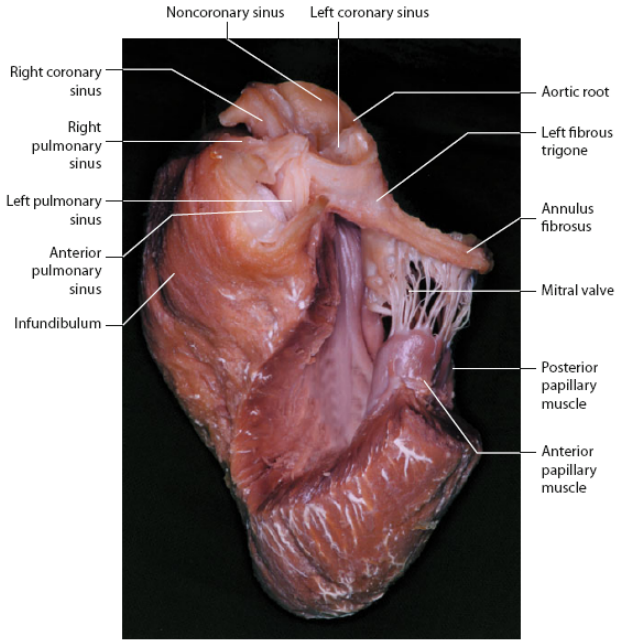

(b)

Figure 1.1: (a) Mitral valve is composed of the anterior and posterior leaflets, the chordae tendineae, the papillary muscles. The mitral valve opens during diastole to allow the blood flow from the left atrium to the left ventricle. During ventricular systole, the mitral valve closes and prevents backflow of the left atrium. Kanjanauthai; (b) Clinic anatomy of mitral valve including fibrosus annulus, mitral valve leaflets, posterior papillary muscle, anterior papillary muscle Berdajs and Turina [2011]

1.2 Literature review

Pathological alterations affecting any component of the mitral valve apparatus can lead to altered valve function. For example, the remodelling that occurs after a posterolateral myocardial infarction can alter mitral valve function by creating conformational abnormalities in the mitral annulus and in the posteromedial papillary muscle, leading to mitral regurgitation and ultimately requiring valve repair or replacement Einstein et al. [2010]. Left ventricular dilation lead to mitral annulus enlargement and incomplete mitral leaflet apposition, though the valve leaflets remain normal in structure and function Wang et al. [2012].

When the normal functioning of a cardiac valve is impaired, surgical repair or replacement is required. There are two basic types of valves that can be used for valve replacement: mechanical or bioprosthetic valves. Mechanical valves are quite durable, but they can induce thrombosis, and their use therefore necessitates sustained anticoagulation therapy(blood thinners), e.g. warfarin, which requires monthly blood tests to monitor. Bioprostheses, in contrast, are less prone to thrombogenesis but generally fail 10 to 15 years post-implantation because of structural degradation. An ideal valve replacement would produce a minimum pressure drop, yield a small regurgitant volume, minimize turbulence, induce low shear stresses, and avoid stagnation and flow separation Yoganathan et al. [2005]. More than 50 types of prosthetic valves have been developed since 1950 Vongpatanasin et al. [1996]. Yet, six decades later, we still use devices that are less than satisfactory. The complex physiology and three-dimensional anatomy of the mitral valve and its surrounding structure present substantial challenges when performing these surgical procedures. Studies showed that the changes in

anterior mitral leaflet geometry could perturb the stress patterns, which in theory may affect repair device durability Bothe et al. [2010a,b]; Wang et al. [2012]. In order to better diagnose, treatment, successfully replace or repair the mitral leaflet and develop effective prosthetic devices, it is important to understand the valve physiology and patho-physiology.

Although there have been numerous studies on heart valves, the mitral valve has been less extensively studied in comparison to the aortic valve, presumably because of the complex structure, its stronger interaction with blood flow and non-stop ventricular motion. Comprehensive assessment of mitral valve physiology and patho-physiology requires detailed modelling of patient anatomy, tissue properties and dynamics, and for such assessments to be clinically useful, they must be based on non-invasive imaging data. Echo-cardiography has been historically preferred in the literature for cardiac diagnostic applications Gabriel et al. [2005] because it offers good temporal resolution, is safe, and is relatively inexpensive. However, it is not an ideal tool for quantification of cardiac function due to its dependency on acoustic windows and operator skill. Nuclear cardiology is said to provide an accurate assessment of left ventricle function with good reproducibility using gated perfusion single-photon emission computed tomography, but the exposure to ionising radiation is unsuitable when repeated measurements are required Alfakih et al. [2004]. By contrast, magnetic resonance imaging (MRI), which now is rapidly gaining acceptance as an accurate and highly reproducible method, provides much higher image quality, primarily because of the higher spatial resolution offered by MRI and its lack of speckle texture, and simplifies the determination of subject- and patient-specific anatomy. Nowadays, the diagnostics obtained using MRI have matured to a level show-

ing very good details of valve motion and blood flow velocities in vivo. However, such imaging modalities do not yield information on the loads applied to the valve that arise from the coupled fluid and structural dynamics of the valve and the blood Lau et al. [2010]. While in vivo stresses in soft tissues cannot be directly measured, an accurate numerical prediction may be directly measured and obtained by combining quantitative information on tissue micro-structure, material behaviour, loading conditions, and in vivo deformation using engineering analysis May-Newman and Yin [1998]. Such data could be used to develop quantitative methods for determining patient-specific medical and surgical strategies for the treatment of valvular heart diseases.

Dynamic modelling of mitral valve bio-mechanics is challenging by the large deformations experienced by the leaflets, the anisotropic non-linear elastic behaviour of the valvular tissue, and the pulsatile haemo-dynamic loads during the cardiac cycle. In order to predict the stress-strain behaviour of the mitral valve, one needs to establish proper material models. Previous, numerical simulations of the mitral valve have been conducted. Kunzelman, Einstein and co-workers were the first to use a three-dimensional computational approach to simulate normal mitral function Einstein et al. [2003, 2005]; Kunzelman et al. [1993], the biomechanics underlying valvular disease Kunzelman et al. [1997, 1998], and surgical interventions Kunzelman et al. [1997, 1998]; Reimink et al. [1996]. Three-dimensional dynamic modelling of the ovine mitral valve has also been performed by Lim et al. [2005], who focused on the asymmetric stress pattern of the mitral valve. Prot et al. reported their work on mitral valve simulations in a series of studies using a transversely isotropic strain-energy functional with the nonlinear finite element (FE) code ABAQUS Prot and Skallerud [2006, 2009]; Prot et al. [2009,

2008]. Recently, their model has been applied to predict the mechanical difference between the healthy mitral valve and the valve in a hypertrophic obstructive cardiomyopathic heart Prot et al. [2010], and active muscle contraction Skallerud et al. [2011] . Kim and co-workers Kim [2009]; Kim et al. [2007, 2008] carried out dynamic simulations of a pericardial bioprosthetic heart valve based on a FE shell model, although their primary focus is on the aortic valve. Maisano et al. [2005] and Votta et al. [2006, 2007] used patient-specific FE models to analyze the effects of annuloplasty procedures. The biomechanical response of the valve to the Alfieri stitch technique was reported by Dal Pan et al. [2005] and Votta et al. [2008]. The effects of the annular contraction on mitral valve stress were modelled by Stevanella et al. [2011a,b]. Urankar [2009] used the LS-DYNA code to model mitral valve fibre stress under various loading and surgical conditions. Kaazempur-Mofrad and Weinberg used FE shell models and fully three-dimensional FE models to predict the dynamic behaviour of the mitral valve Weinberg [2005]. Their work incorporated fibre direction as an additional degree of freedom to model the large-deformation and anisotropic behaviour of mitral valves, and their method was demonstrated using an existing constitutive law for mitral valve tissue Weinberg and Kaazempur Mofrad [2007]. Wenk et al. [2010] developed a FE model of the left ventricle, mitral apparatus, and chordae tendineae from magnetic resonance (MR) images obtained from sheep. Krishnamurthy et al. [2009] used inverse FE analysis and radiopaque markers sewn to the mitral annulus to show that, unlike isolated leaflets, the in vivo elastic response of the anterior mitral leaflet is linear over a physiologic range of pressures. Arnoldi et al. [2010] developed mitral valve model-construction software with a graphical user interface (GUI), in which they integrated FE computations

with four-dimensional echocardiographic image processing in a high-performance computing (HPC) environment. They found this approach to accelerate the process of mitral valve modelling for patient-specific analysis. Wang et al. [2012] presented a patient-specific finite element model of a healthy human mitral valve reconstructed from multi-slice computed tomography scans(MSCT) with detailed mitral leaflet thickness, chordal information and mitral annulus dynamic motion. There are also several recent review papers on mitral valve research, each with different foci Einstein et al. [2010]; Sacks et al. [2009a,b]; Weinberg et al. [2010]. In the last decades, mitral valve material properties have also been investigated. Due to the scarcity and complications associated with human valve tissue, it is difficult to experimentally determine the mechanical properties of normal, healthy human mitral valve leaflets. A lot of studies are based on animal valves (e.g. porcine, sheep, dog...), which can provide a reasonable substitute as the size, collagen composition, and fibrous architecture of valves are quite similar to human. R.P.Cochran [1991] focused on the central region of the anterior and posterior leaflets where the fibres are oriented along the circumferential axis, parallel to the mitral annulus. Kunzelman and Cochran [1992] discussed the stress/strain characteristics of porcine mitral valve tissue along parallel and perpendicular collagen orientation. May-Newman and Yin [1995, 1998] carried out biaxial mechanical tests on porcine mitral valve and demonstrated that the tissue was stiffer and less extensible along circumferential direction and propose strain energy function describing mitral valve as an initially and locally transversely isotropic material. Liao and Vesely [2003]; Ritchie et al. [2006] have performed mechanical tests on different kinds of chordae and highlighted differences in mechanical behaviour depending on size and type of porcine mitral chordae. Prot and Skallerud

[2006, 2009]; Prot et al. [2009, 2010, 2008] performed mechanical tests on porcine and human mitral apparatus and especially compared the differences in material properties between porcine and human, healthy and diseased human mitral valve. Wang et al. [2012] conducted biaxial test for healthy human mitral leaflets and used a constitutive model in which mitral tissue is assumed to be composed of a matrix material with two families of embedded fibres.

There is large inter-subject variability in the anatomy of the MV apparatus which plays an important role in order to determine the stress state in the leaflets. The mitral annulus shape and its dynamic behaviour during the cardiac cycle have been studied in animals and humans using different imaging techniques such as two-dimensional echo-cardiography, MRI (Flachskampf et al. [2000]; Green et al. [1999]; Kaplan et al. [2000]; Prot and Skallerud [2006]; Salgo et al. [2002]; Tibayan et al. [2003]) etc. All of the above studies assume that the annulus is symmetric, either flat or with saddle height. However, in reality the annulus ring is irregular and asymmetric in three-dimensions. The current tendency is to obtain subject-specific mitral leaflets and spatial shape of annulus for dynamic modelling Arnoldi et al. [2010]; Ma et al. [2012]; Stevanella et al. [2011b]; Wang et al. [2012].

1.3 Work summary

The present work focuses on constructing mitral valve fluid-structure interaction models with immersed boundary method. In these models, the blood is described as a viscous incompressible fluid, and the mitral valve and its substructures are described as elastic or hypo-elastic solid structures. In chapter 1 we introduce the mitral valve anatomy and review the research background. In chapter 2

we explain the mathematical and numerical formulations of immersed boundary method and finite element immersed boundary method that we use for mitral valve modelling.

In chapter 3, we model the dynamics of a prosthetic mitral valve using a staggered-grid version Griffith [2012a,b]; Griffith et al. [2009] of a formally second-order accurate immersed boundary method Griffith [2005]; Lai and Peskin [2000]. Herein we use an experimentally measured pressure gradient to drive flow through the model valve during the diastolic phase of the cardiac cycle, and to provide a realistic pressure load for the closed valve during the systolic phase of the cardiac cycle, enabling us to perform more realistic simulations. In this work, we demonstrate that when bending rigidity are included in both the mitral leaflets and chordae, the computational results has better agreements with experimental measurements. In addition, non-physical oscillations that occur upon valve closure are greatly reduced when bending forces are included in the model. These findings highlight the importance of accounting for the bending stiffness in the dynamic simulation of the mitral valve prosthesis. Furthermore, the final goal of mitral valve prosthesis analysis is to lead to better diagnosis and treatment for patient valvular heart diseases Luo et al. [2012]. However, without comprehensive understanding of native mitral valve, such analysis still has limitations because of the relatively simple three-dimensional anatomy and the linear material properties of the mitral valve. In such cases, the patient-specific mitral valve dynamic modelling is urgent and necessary for the optimization of therapies to restore normal mitral valve functioning in patients with valvular heart diseases.

In chapter 4, an in-vivo human mitral valve geometry model is derived from magnetic resonance imaging (MRI) data, and then is analysed using the immersed

boundary method under a physiological left-atrium-ventricle pressure loading. An initial validation of the model is provided by comparing the computed opening shape and flow rates to clinical measurements from the volunteer who provided the anatomical data for constructing the mitral valve. The convex (with respect to the left ventricle) shape near annulus and concave shape near free edge of valve are observed in our simulation during diastole and systole when assigning physiological thickness McDonald et al. [2002] to the anterior leaflet and posterior leaflet, which match perfectly with clinical observations Karlsson et al. [1998]; Kvitting et al. [2010]; Ryan et al. [2008]. These results suggest that differences in the thickness of the leaflets play an important role in maintaining the physiological curvature of the mitral valve Ma et al. [2012]. These features bring out a question that is the relatively simple isotropic material fibre model sufficient to describe the mitral valve leaflets. The real valve is anisotropic, with collagen fibres distributed along the circumferential direction. To better model this nonlinear mechanical behaviour of the mitral valve leaflets, it is of importance to use experimentally characterised strain-energy functions for material properties. Extensions of the immersed boundary method that permit such finite-element-based elasticity models have been developed over the past decade Boffi et al. [2008]; Liu et al. [2006]; Zhang and Gay [2007]; Zhang et al. [2004], and one such extension of the immersed boundary method was already implemented within the IBAMR software Griffith and Luo [2012] used to perform the simulations described in chapter 5.

In chapter 5, the in-vivo human mitral valve geometry model was improved by incorporating spatial annulus ring from integrating physical information from cardiac MRI data. This mitral valve model is then simulated under a physiological

pressure loading with a finite element version of the immersed boundary method that is able to incorporate experimentally oriented constitutive laws for elasticity models Griffith and Luo [2012]. A hypo-elastic transversely isotropic material constitutive law is used to characterize the mechanical behaviour of the mitral valve tissue based on recent biaxial tests on healthy human leaflets by Wang et al. [2012]. Simulation results exhibit better agreement and reduced oscillations in flow rate compared with experiment measurements and previous simulation Ma et al. [2012] and show that the maximum principal stress and strain is carried by the collagen fibres in the mitral leaflets in deep systole. These results show that the methodology in this study could generate a patient-specific finite element mitral valve model that closely replicated the in vivo mitral valve dynamic motion during diastole and systole. This model may be further developed to study mitral valve mechanics and disease to bring more insight of diagnosis, treatment, and prevention of patient valvular heart diseases.

Chapter 2

Methodology

The immersed boundary method is a mathematical formulation and numerical approach to fluid-structure interaction problems in which an elastic structure is immersed in a viscous incompressible fluid. This method was originally introduced by Peskin to study blood flow through heart valves Peskin [1977]. The immersed boundary formulation of such problems uses a Lagrangian description of the deformation and elasticity of the immersed structure along with an Eulerian description of the momentum, velocity and incompressibility of the coupled viscous incompressible fluid, which is modelled by incompressible Navier-Stokes equations.

2.1 The immersed boundary method

2.1.1 The continuous formulation

We assume that the fluid possesses a uniform mass density ρ and dynamic viscosity μ, and that the immersed elastic structure is neutrally buoyant.

Let $\mathbf{x} = (x, y, z) \in \Omega$ denote Cartesian physical coordinates, in which $\Omega \in \mathbb{R}^3$ is the physical domain; let $\mathbf{s} = (r, s) \in U$ denote Lagrangian material coordinates attached to the structure, in which $U \in \mathbb{R}^2$ is the Lagrangian curvilinear coordinate domain; and let $\mathbf{X}(\mathbf{s}, t) \in \Omega$ denote the physical position of material point $\mathbf{s}$ at time t. The physical region occupied by the structure at time t is $\mathbf{X}(U, t) \subseteq \Omega$, and the physical region occupied by the fluid at time t is $\Omega \setminus \mathbf{X}(U, t)$. The equations of motion for the coupled fluid-structure system are

$$\rho \left(\frac{\partial \mathbf{u}}{\partial t}(\mathbf{x}, t) + \mathbf{u}(\mathbf{x}, t) \cdot \nabla \mathbf{u}(\mathbf{x}, t) \right) = -\nabla p(\mathbf{x}, t) + \mu \nabla^2 \mathbf{u}(\mathbf{x}, t) + \mathbf{f}(\mathbf{x}, t), \tag{2.1}$$

$$\nabla \cdot \mathbf{u}(\mathbf{x}, t) = 0, \tag{2.2}$$

$$\mathbf{f}(\mathbf{x}, t) = \int_U \mathbf{F}(\mathbf{s}, t)\, \delta(\mathbf{x} - \mathbf{X}(\mathbf{s}, t))\, \mathrm{d}\mathbf{s}, \tag{2.3}$$

$$\frac{\partial \mathbf{X}}{\partial t}(\mathbf{s}, t) = \int_\Omega \mathbf{u}(\mathbf{x}, t)\, \delta(\mathbf{x} - \mathbf{X}(\mathbf{s}, t))\, \mathrm{d}\mathbf{x}, \tag{2.4}$$

$$\mathbf{F}(\cdot, t) = \mathcal{F}[\mathbf{X}(\cdot, t)]. \tag{2.5}$$

Eqs. (2.1) and (2.2) are the incompressible Navier-Stokes equations, which are written in terms of the Eulerian velocity field $\mathbf{u}(\mathbf{x}, t) = (u(\mathbf{x}, t), v(\mathbf{x}, t), w(\mathbf{x}, t))$ and the Eulerian pressure field $p(\mathbf{x}, t)$, along with a body force $\mathbf{f}(\mathbf{x}, t)$ that is the Eulerian elastic force density applied by the structure to the fluid. Eq. (2.5) indicates that the Lagrangian elastic force density generated by the elasticity of the structure is determined by a time-independent functional of the configuration of the immersed structure; this particular Lagrangian force functional is discussed below. Eqs. (2.3) and (2.4) are Lagrangian-Eulerian interaction equations that use integral transformations with three-dimensional Dirac delta function kernels, $\delta(\mathbf{x}) = \delta(x)\, \delta(y)\, \delta(z)$, to couple the Lagrangian and Eulerian descriptions. Specif-

ically, Eq. (2.3) converts the Lagrangian elastic force density $\mathbf{F}$ into the equivalent Eulerian elastic force density $\mathbf{f}$. Notice that $\mathbf{F}$ and $\mathbf{f}$ have totally different characters: $\mathbf{F}(\mathbf{s},t)$ is a force density with respect to the curvilinear coordinate system (i.e. $\mathbf{F}(\mathbf{s},t)\,\mathrm{d}r\,\mathrm{d}s$ has units of force), whereas $\mathbf{f}(\mathbf{x},t)$ is a force density with respect to the physical coordinate system (i.e. $\mathbf{f}(\mathbf{x},t)\,\mathrm{d}x\,\mathrm{d}y\,\mathrm{d}z$ has units of force). Nonetheless, $\mathbf{F}$ and $\mathbf{f}$ are equivalent as densities Peskin [2002]. Eq. (2.4) states that the structure moves at the local fluid velocity, i.e.,

$$\frac{\partial \mathbf{X}}{\partial t}(\mathbf{s},t) = \mathbf{u}(\mathbf{X}(\mathbf{s},t),t), \tag{2.6}$$

which is the no-slip condition of a viscous fluid. Note that the no-slip condition is used to determine the motion of the immersed elastic structure rather than to constrain the motion of the fluid.

Along the boundary of the physical domain Ω, we impose no-slip boundary conditions on the tangential components of the fluid velocity, along with either Dirichlet boundary conditions on the normal component of the velocity or prescribed normal traction boundary conditions. Here, the no-slip condition is used to constrain the motion of the fluid. Since the fluid is incompressible and Newtonian, the combination of no-slip tangential velocity boundary conditions and normal traction boundary conditions is equivalent to a prescribed-pressure boundary conditions Griffith [2012b].

The elasticity of these immersed structures is described by systems of elastic fibres that resist extension, compression, and bending. We choose the Lagrangian curvilinear coordinates (r,s) so that each fixed value of s labels a particular fibre, and we compute the total elastic forces generated by the immersed fibres as the

sum of a stretching force density and a bending force density. Let $T = T(\mathbf{s})$ be the fibre tension, so that $T\,\mathrm{d}r\,\mathrm{d}s$ has units of force, and let $\boldsymbol{\tau} = \boldsymbol{\tau}(\mathbf{s}) = \frac{\partial \mathbf{X}/\partial s}{|\partial \mathbf{X}/\partial s|}$ be the unit tangent vector aligned with the fibres. We compute $\mathbf{F}$ by

$$\mathbf{F} = \frac{\partial}{\partial s}(T\boldsymbol{\tau}) + \frac{\partial^2}{\partial s^2}\left(\kappa \frac{\partial^2}{\partial s^2}\mathbf{X}\right), \tag{2.7}$$

in which $\kappa = EI$ is the bending stiffness coefficient, with E denoting the Young's modulus and I denoting the cross-sectional moment of inertia.

2.1.2 The spatial discretization

In the numerical treatment of the continuous immersed boundary equations of motion, the Eulerian variables are discretized on a uniform, staggered-Cartesian grid and the Lagrangian variables are discretized on a fibre-aligned mesh which moves with the structure Griffith [2009, 2012a,b].

To simplify the exposition, we assume that the physical domain Ω is the unit cube, discretized on a regular $N \times N \times N$ Cartesian grid with grid spacings $\triangle x = \triangle y = \triangle z = h = \frac{1}{N}$. The Cartesian grid cells are indexed $i, j, k = 0, 1..., N-1$. The positions of the centres of the Cartesian grid cells are $\mathbf{x}_{i,j,k} = ((i+\frac{1}{2})h, (j+\frac{1}{2})h, (k+\frac{1}{2})h)$, and the positions of the centers of edges of the Cartesian grid cells are, respectively, $\mathbf{x}_{i+\frac{1}{2},j,k} = ((i+1)h, (j+\frac{1}{2})h, (k+\frac{1}{2})h)$, $\mathbf{x}_{i,j+\frac{1}{2},k} = ((i+\frac{1}{2})h, (j+1)h, (k+\frac{1}{2})h)$, $\mathbf{x}_{i,j,k+\frac{1}{2}} = ((i+\frac{1}{2})h, (j+\frac{1}{2})h, (k+1)h)$. Similarly, let (l, m) label an individual curvilinear mesh node, and let the curvilinear mesh spacings be denoted by Δr, Δs.

In a staggered-grid discretization, the pressure is defined at the centers of the Cartesian grid cells and the edge-normal components of the velocity are defined at

the centres of the edges of the Cartesian grid cells. Let $u_{i+\frac{1}{2},j,k}$, $v_{i,j+\frac{1}{2},k}$ and $w_{i,j,k+\frac{1}{2}}$ denote staggered-grid approximations to the components of the Eulerian velocity field that are defined at positions $\mathbf{x}_{i+\frac{1}{2},j,k}$, $\mathbf{x}_{i,j+\frac{1}{2},k}$, and $\mathbf{x}_{i,j,k+\frac{1}{2}}$, respectively; let $p_{i,j,k}$ denote a cell-centred approximation to the pressure defined at positions $\mathbf{x}_{i,j,k}$; let $\mathbf{X}_{l,m}$ and $\mathbf{F}_{l,m}$ denote approximations to the position and Lagrangian elastic force density at node (l,m) of the Lagrangian curvilinear mesh.

The discretizations of the Lagrangian-Eulerian interaction equations, Eqs.(2.4) and Eqs.(2.3) both employ the same regularized four-point delta function of Peskin Peskin [2002], denoted $\delta_h = \delta_h(x)\,\delta_h(y)\,\delta_h(z)$. The discretization of Eqs.(2.4) are

$$U_{l,m} = \sum_{i,j,k} u_{i-\frac{1}{2},j,k}\,\delta_h(\mathbf{x}_{i-\frac{1}{2},j,k} - \mathbf{X}_{l,m})\,h^3, \tag{2.8}$$

$$V_{l,m} = \sum_{i,j,k} v_{i,j-\frac{1}{2},k}\,\delta_h(\mathbf{x}_{i,j-\frac{1}{2},k} - \mathbf{X}_{l,m})\,h^3, \tag{2.9}$$

$$W_{l,m} = \sum_{i,j,k} w_{i,j,k-\frac{1}{2}}\,\delta_h(\mathbf{x}_{i,j,k-\frac{1}{2}} - \mathbf{X}_{l,m})\,h^3, \tag{2.10}$$

and the discretization of Eqs.(2.3) are

$$(f_x)_{i+\frac{1}{2},j,k} = \sum_{l,m} (F_x)_{l,m}\;\delta_h(\mathbf{x}_{i+\frac{1}{2},j,k} - \mathbf{X}_{l,m})\,\Delta r\,\Delta s, \tag{2.11}$$

$$(f_y)_{i,j+\frac{1}{2},k} = \sum_{l,m} (F_y)_{l,m}\;\delta_h(\mathbf{x}_{i,j+\frac{1}{2},k} - \mathbf{X}_{l,m})\,\Delta r\,\Delta s, \tag{2.12}$$

$$(f_z)_{i,j,k+\frac{1}{2}} = \sum_{l,m} (F_z)_{l,m}\;\delta_h(\mathbf{x}_{i,j,k+\frac{1}{2}} - \mathbf{X}_{l,m})\,\Delta r\,\Delta s. \tag{2.13}$$

2.1.3 The temporal discretization

The time stepping scheme that we use is similar to that of Griffith [2012a]; however, in the present work, we employ an Adams-Bashforth scheme to enable us to attain second-order accuracy in time while solving the incompressible Navier-Stokes only once per time step.

Let $\nabla_h \cdot$, ∇_h, and ∇_h^2 denote standard staggered-grid finite-difference approximations to the divergence, gradient, and Laplace operators, respectively. We denote by $\mathbf{X}^n$, $\mathbf{u}^n$, and $p^{n-\frac{1}{2}}$ approximations to the values of $\mathbf{X}$ and $\mathbf{u}$ at time t^n, and to the value of p at time $t^{n-\frac{1}{2}}$.

Given $\mathbf{X}^n$, $\mathbf{u}^n$, and $p^{n-\frac{1}{2}}$, we obtain $\mathbf{X}^{n+1}$, $\mathbf{u}^{n+1}$, and $p^{n+\frac{1}{2}}$ by first computing

$$\frac{\tilde{\mathbf{X}}^{n+1} - \mathbf{X}^n}{\Delta t} = \mathcal{R}^n \mathbf{u}^n, \tag{2.14}$$

in which $\mathcal{R}^n = \mathcal{R}(\mathbf{X}^n)$ is the *velocity restriction* operator, for which $\mathbf{U}^n = (U^n, V^n, W^n) = \mathcal{R}^n \mathbf{u}^n$. And $\tilde{\mathbf{X}}^{n+1}$ is a preliminary value of $\mathbf{X}^{n+1}$ for calculating sub-step to the half-time level of $\mathbf{X}^{n+\frac{1}{2}}$. To obtain a time step-centered approximation to $\mathbf{X}$, we compute

$$\mathbf{X}^{n+\frac{1}{2}} = \frac{\tilde{\mathbf{X}}^{n+1} + \mathbf{X}^n}{2}. \tag{2.15}$$

We next solve

$$\rho\left(\frac{\mathbf{u}^{n+1}-\mathbf{u}^{n}}{\Delta t}+\mathbf{A}^{n+\frac{1}{2}}\right)=-\nabla_h p^{n+\frac{1}{2}}+\mu\nabla_h^2\frac{\mathbf{u}^{n+1}+\mathbf{u}^{n}}{2}+\mathbf{f}^{n+\frac{1}{2}}, \tag{2.16}$$

$$\nabla_h\cdot\mathbf{u}^{n+1}=0, \tag{2.17}$$

$$\mathbf{f}^{n+\frac{1}{2}}=\mathcal{S}\left(\mathbf{X}^{n+\frac{1}{2}}\right)\mathbf{F}\left(\mathbf{X}^{n+\frac{1}{2}}\right), \tag{2.18}$$

$$\frac{\mathbf{X}^{n+1}-\mathbf{X}^{n}}{\Delta t}=\mathcal{R}\left(\mathbf{X}^{n+\frac{1}{2}}\right)\frac{\mathbf{u}^{n+1}+\mathbf{u}^{n}}{2}, \tag{2.19}$$

for $\mathbf{X}^{n+1}$, $\mathbf{u}^{n+1}$, and $p^{n+\frac{1}{2}}$, in which $\mathbf{A}^{n+\frac{1}{2}}=\frac{3}{2}\mathbf{u}^{n}\cdot\nabla_h\mathbf{u}^{n}-\frac{1}{2}\mathbf{u}^{n-1}\cdot\nabla_h\mathbf{u}^{n-1}$ is an approximation to the nonlinear advection term computed by a version of the piecewise parabolic method (PPM) Colella and Woodward [1984]; Rider et al. [2007]. Here, $\mathcal{S}^n=\mathcal{S}\left(\mathbf{X}^n\right)$ is the *force prolongation* operator, for which $\mathbf{f}^{n+\frac{1}{2}}=(f_x^{n+\frac{1}{2}},f_y^{n+\frac{1}{2}},f_z^{n+\frac{1}{2}})=\mathcal{S}^{n+\frac{1}{2}}\mathbf{F}^{n+\frac{1}{2}}$. Notice that by construction, $\mathcal{S}$ and $\mathcal{R}$ are adjoint operators. This property ensures that the semi-discrete scheme conserves energy during Lagrangian-Eulerian interaction Peskin [2002].

This scheme must be modified during the first time step because time step-lagged values of $\mathbf{u}$ and p are not available. During the initial time step, we first solve

$$\rho\left(\frac{\tilde{\mathbf{u}}^{n+1}-\mathbf{u}^{n}}{\Delta t}+\mathbf{A}^{n}\right)=-\nabla_h\tilde{p}^{n+\frac{1}{2}}+\mu\nabla_h^2\frac{\tilde{\mathbf{u}}^{n+1}+\mathbf{u}^{n}}{2}+\mathbf{f}^{n}, \tag{2.20}$$

$$\nabla_h\cdot\tilde{\mathbf{u}}^{n+1}=0, \tag{2.21}$$

$$\mathbf{f}^{n}=\mathcal{S}\left(\mathbf{X}^{n}\right)\mathbf{F}\left(\mathbf{X}^{n}\right), \tag{2.22}$$

$$\frac{\tilde{\mathbf{X}}^{n+1}-\mathbf{X}^{n}}{\Delta t}=\mathcal{R}\left(\mathbf{X}^{n}\right)\mathbf{u}^{n}, \tag{2.23}$$

for $\tilde{\mathbf{X}}^{n+1}$, $\tilde{\mathbf{u}}^{n+1}$, and $\tilde{p}^{n+\frac{1}{2}}$, where $\mathbf{A}^n = \mathbf{u}^n \cdot \nabla_h \mathbf{u}^n$. We then compute

$$\mathbf{X}^{n+\frac{1}{2}} = \frac{\tilde{\mathbf{X}}^{n+1} + \mathbf{X}^n}{2}, \tag{2.24}$$

and finally solve Eqs. (2.16)–(2.19) for $\mathbf{X}^{n+1}$, $\mathbf{u}^{n+1}$, and $p^{n+\frac{1}{2}}$, except that we use $\mathbf{A}^{n+\frac{1}{2}} = \mathbf{u}^{n+\frac{1}{2}} \cdot \nabla_h \mathbf{u}^{n+\frac{1}{2}}$ with $\mathbf{u}^{n+\frac{1}{2}} = \frac{1}{2}\left(\tilde{\mathbf{u}}^{n+1} + \mathbf{u}^n\right)$.

2.2 FE version of the immersed boundary method

2.2.1 The continuous formulation

To use an Eulerian description of the fluid and a Lagrangian description of the elasticity of the immersed structure, it is necessary to describe the stress of the fluid-structure system in both Eulerian and Lagrangian forms. Let $\sigma = \sigma(\mathbf{x}, t)$ denote the Cauchy stress tensor of the coupled fluid-structure system. Then

$$\sigma(\mathbf{x}, t) = \begin{cases} \sigma^{\mathrm{f}}(\mathbf{x}, t) + \sigma^{e}(\mathbf{x}, t) & \text{for } x \in \mathbf{X}(U, t) \\ \sigma^{\mathrm{f}}(\mathbf{x}, t) & \text{otherwise,} \end{cases} \tag{2.25}$$

$\sigma^{\mathrm{f}}(\mathbf{x}, t)$ is the stress tensor of a viscous incompressible fluid defined as

$$\sigma^{\mathrm{f}}(\mathbf{x}, t) = -p\mathbb{I} + \mu[\nabla \mathbf{u} + (\nabla \mathbf{u})^{\top}], \tag{2.26}$$

in which $p = p(\mathbf{x}, t)$ is the fluid pressure, μ is the dynamic viscosity of the fluid, and $\mathbf{u} = \mathbf{u}(\mathbf{x}, t)$ is the Eulerian velocity field. $\sigma^{e}(\mathbf{x}, t)$ is the stress tensor that describes the elasticity of the immersed structure. With respect to the Lagrangian material coordinate system, it is convenient to use the first Piola-Kirchhoff elastic

stress tensor $\mathbb{P}^e(\mathbf{s},t)$, which is defined as

$$\int_{\partial V} \mathbb{P}^e(\mathbf{s},t)\mathbf{N}dA(\mathbf{s})) = \int_{\partial \mathbf{X}_{(V,t)}} \sigma^e(\mathbf{x},t)\mathbf{n}da(\mathbf{x}) \tag{2.27}$$

for any smooth region $V \subset U$, in which $\mathbf{N} = \mathbf{N}(\mathbf{s})$ is the outward unit normal along ∂V, and $\mathbf{n} = \mathbf{n}(\mathbf{x},t)$ is the outward normal along $\partial \mathbf{X}(V,t)$. The hypo-elastic mechanical behaviour can be characterized by a strain-energy functional $W^e = W^e(\mathbb{F})$, in which $\mathbb{F} = \mathbb{F}(\mathbf{s},t) = \nabla_{\mathbf{S}}\mathbf{X}(\mathbf{s},t) = \frac{\partial \mathbf{X}}{\partial s}(\mathbf{s},t)$ is the deformation gradient associated with the mapping $\mathbf{X} : (U,t) \to \Omega$. For such constitutive laws, $\mathbb{P}^e(\mathbf{s},t) = \frac{\partial W^e}{\partial \mathbb{F}}(\mathbf{s},t)$.

The weak formulation of the equations of motion for the coupled fluid-structure system are

$$\rho\left(\frac{\partial \mathbf{u}}{\partial t}(\mathbf{x},t) + \mathbf{u}(\mathbf{x},t)\cdot\nabla\mathbf{u}(\mathbf{x},t)\right) = -\nabla p(\mathbf{x},t) + \mu\nabla^2\mathbf{u}(\mathbf{x},t) + \mathbf{f}(\mathbf{x},t), \tag{2.28}$$

$$\nabla\cdot\mathbf{u}(\mathbf{x},t) = 0, \tag{2.29}$$

$$\mathbf{f}(\mathbf{x},t) = \int_U \mathbf{F}(\mathbf{s},t)\,\delta(\mathbf{x}-\mathbf{X}(\mathbf{s},t))\,\mathrm{d}\mathbf{s}, \tag{2.30}$$

$$\int_U \mathbf{F}(\mathbf{s},t)\cdot\mathbf{V}(\mathbf{s})\mathrm{d}\mathbf{s} = -\int_U \mathbb{P}^e(\mathbf{s},t) : \nabla_s\mathbf{V}(\mathbf{s})\mathrm{d}\mathbf{s}, \forall\mathbf{V}(\mathbf{s}), \tag{2.31}$$

$$\frac{\partial \mathbf{X}}{\partial t}(\mathbf{s},t) = \int_\Omega \mathbf{u}(\mathbf{x},t)\,\delta(\mathbf{x}-\mathbf{X}(\mathbf{s},t))\,\mathrm{d}\mathbf{x}. \tag{2.32}$$

in which $\mathbf{f}(\mathbf{x},t)$ and $\mathbf{F}(\mathbf{s},t)$ are the Eulerian and Lagrangian elastic force densities, and $V(\mathbf{s})$ is an arbitrary Lagrangian test function that is not assumed to vanish on ∂U.

2.2.2 The spatial and temporal discretization

Herein, we use a interpolatory finite element basis discretization of the Lagrangian equations and the same uniform, staggered-grid discretization of the Eulerian equations as described in IB method in previous section.

Briefly, let $u_{i+\frac{1}{2},j,k}$, $v_{i,j+\frac{1}{2},k}$, and $w_{i,j,k+\frac{1}{2}}$ denote staggered-grid approximations to the components of the Eulerian velocity field that are defined at positions $\mathbf{x}_{i+\frac{1}{2},j,k}$, $\mathbf{x}_{i,j+\frac{1}{2},k}$, and $\mathbf{x}_{i,j,k+\frac{1}{2}}$, respectively; and let $\nabla_h \cdot$, ∇_h, and ∇_h^2 denote standard staggered-grid finite-difference approximations to the divergence, gradient, and Laplace operators, respectively, in which h is the Cartesian grid spacing. Let $\tau_h = \cup_e U^e$ be a triangulation of U composed of elements U^e. We denote the nodes of mesh by $\{\mathbf{s}\}_{l=1}^M$, and time-depend physical positions of the nodes of the Lagrangian mesh by $\{\mathbf{X}_l(t)\}_{l=1}^M$. Using the Lagrangian basis functions, we define an approximation to $\mathbf{X}(\mathbf{s},t)$ by

$$\mathbf{X}_h(\mathbf{s},t) = \sum_{l=1}^{M} \mathbf{X}_l(t)\phi_l(\mathbf{s}) \tag{2.33}$$

in which $\phi_l(\mathbf{s})$ is the interpolatory Lagrangian basis function. An approximation to the deformation gradient is given by

$$\mathbb{F}_h(\mathbf{s},t) = \frac{\partial \mathbf{X}_h(\mathbf{s},t)}{\partial \mathbf{s}} = \sum_{l=1}^{M} \mathbf{X}_l(t)\frac{\partial \phi_l(\mathbf{s})}{\partial \mathbf{s}} \tag{2.34}$$

Using $\mathbb{F}_h(\mathbf{s},t)$, we compute directly $\mathbb{P}_h^e(\mathbf{s},t)$, which is approximation to the first Piola-Kirchhoff stress tensor. We approximate the Lagrangian force density

$\mathbf{F}(\mathbf{s},t)$ by

$$\mathbf{F}_h(\mathbf{s},t) = \sum_{l=1}^{M} \mathbf{F}_l(t)\phi_l(\mathbf{s}) \tag{2.35}$$

The nodal values $\mathbf{F}_l(t)_{l=1}^{M}$ must be determined from $\mathbb{P}_h^e(\mathbf{s},t)$. By restricting the test functions to be linear combinations of the Lagrangian basis functions, we have that Eqs.(2.31) become,

$$\sum_{l=1}^{M} \left(\int_U \phi_l(\mathbf{s})\phi_m(\mathbf{s})\mathrm{d}\mathbf{s} \right) \mathbf{F}_l(t) = -\int_U \mathbb{P}_h^e(\mathbf{s},t) \bigtriangledown_{\mathbf{s}} \phi_m(\mathbf{s})\mathrm{d}\mathbf{s} \tag{2.36}$$

To compute an approximation to $\mathbf{f} = (f_x, f_y, f_z)$ on the Cartesian grid, we construct for each element $U^e \in \tau_h$ a Gaussian quadrature rule with N^e quadrature points $\mathbf{s}_Q^e \in U^e$ and weights w_Q^e, $Q = 1, ..., N^e$. We then compute f_x, f_y and f_z on the edges of the Cartesian grid cells via

$$(f_x)_{i+\frac{1}{2},j,k} = \sum_{U^e \in \tau_h} \sum_{Q=1}^{N^e} F_x(\mathbf{s}_Q^e,t)\, \delta_h(\mathbf{x}_{i+\frac{1}{2},j,k} - \mathbf{X}\left(\mathbf{s}_Q^e,t\right))\, w_Q^e \tag{2.37}$$

$$(f_y)_{i,j+\frac{1}{2},k} = \sum_{U^e \in \tau_h} \sum_{Q=1}^{N^e} F_y(\mathbf{s}_Q^e,t)\, \delta_h(\mathbf{x}_{i,j+\frac{1}{2},k} - \mathbf{X}\left(\mathbf{s}_Q^e,t\right))\, w_Q^e \tag{2.38}$$

$$(f_z)_{i,j,k+\frac{1}{2}} = \sum_{U^e \in \tau_h} \sum_{Q=1}^{N^e} F_z(\mathbf{s}_Q^e,t)\, \delta_h(\mathbf{x}_{i,j,k+\frac{1}{2}} - \mathbf{X}\left(\mathbf{s}_Q^e,t\right))\, w_Q^e \tag{2.39}$$

in which Lagrangian force density $\mathbf{F}(\mathbf{s},t) = (F_x(\mathbf{s},t), F_y(\mathbf{s},t), F_z(\mathbf{s},t))$. We use the shorthand

$$\mathbf{f} = \mathcal{S}\mathbf{F} \tag{2.40}$$

in which $\mathcal{S}$ is the *force prolongation* operator defined by (2.37), (2.38) and (2.39). A corresponding *velocity restriction operator* $\mathcal{R} = \mathcal{R}(\mathbf{X})$ is used to determine the

motion of the nodes of the Lagrangian mesh from the Cartesian grid velocity field via

$$\frac{\mathrm{d}\mathbf{X}}{\mathrm{d}t} = \mathcal{R}\mathbf{u} \tag{2.41}$$

$\frac{\partial \mathbf{X}}{\partial t}(\mathbf{s},t)$ is an approximation to the L^2 projection of the Lagrangian vector field $\mathbf{U}^{IB}(\mathbf{s},t) = (U^{IB}(\mathbf{s},t), V^{IB}(\mathbf{s},t), W^{IB}(\mathbf{s},t))$ with

$$U^{IB}(\mathbf{s},t) = \sum_{i,j,k} u_{i-\frac{1}{2},j,k}\, \delta_h(\mathbf{x}_{i-\frac{1}{2},j,k} - \mathbf{X}(\mathbf{s},t))\, h^3, \tag{2.42}$$

$$V^{IB}(\mathbf{s},t) = \sum_{i,j,k} v_{i,j-\frac{1}{2},k}\, \delta_h(\mathbf{x}_{i,j-\frac{1}{2},k} - \mathbf{X}(\mathbf{s},t))\, h^3, \tag{2.43}$$

$$W^{IB}(\mathbf{s},t) = \sum_{i,j,k} w_{i,j,k-\frac{1}{2}}\, \delta_h(\mathbf{x}_{i,j,k-\frac{1}{2}} - \mathbf{X}(\mathbf{s},t))\, h^3, \tag{2.44}$$

$\delta_h(\mathbf{x})$ is the one dimensional smoothed delta function of Peskin Peskin [2002].

The Lagrangian-Eulerian interaction is different from previous immersed boundary method in a way: first, the nodal values of $\mathbf{F}$ are interpolated from the mesh nodes to quadrature points within each element; then $\delta_h(\mathbf{x})$ is used to spread those interpolated force densities from the quadrature points to the Cartesian grid. It is similar for the velocity: first, the Cartesian velocity field is interpolated to the quadrature points using $\delta_h(\mathbf{x})$; these samples of $\mathbf{U}^{IB}$ are then used to compute the right-hand-side of an L^2-projection equation, and the solution of this projection equation determines $\frac{\partial \mathbf{X}}{\partial t}(\mathbf{s},t)$. In this approach, the Lagrangian structure is watertight if quadrature points are dense enough.

The finite element version of immersed boundary method has the same temporal discretization with immersed boundary method as described in previous section in this chapter.

2.3 Summary of IB and IB-FE method

The finite element version of immersed boundary method combines a Cartesian grid finite difference method for incompressible fluid dynamics with a nodal finite element method for non-linear elasticity. In conventional immersed boundary method (Griffith et al. [2009]; Luo et al. [2012]; Ma et al. [2012]), regularized delta functions are used by the immersed boundary method both to spread forces generated by the immersed structure from the nodes of the Lagrangian mesh to the Eulerian grid and also to interpolate velocities from the Eulerian grid to the nodes of the Lagrangian mesh. A significant limitation of this approach is that if the physical spacing of the Lagrangian nodes is too large in comparison to the background Eulerian grid, severe "leaks" will develop at fluid-structure interfaces Griffith and Luo [2012]. An empirical solution that generally prevents such leaks is to make the Lagrangian mesh to be approximately twice as fine as the Eulerian mesh Peskin [2002]. As high Eulerian resolution is needed to capture the thin boundary layers characteristic of flows, therefore, following the empirical rule will result in dense Lagrangian meshes that may generate significant numerical stiffness in the discretized equations and excessively small time steps. Moreover, when an initially "watertight" structure exhibits large deformations, the structure mesh may ultimately yield leaks as the simulation progresses.

One advantage of using the finite element version of immersed boundary method is to discretize the equations of Lagrangian-Eulerian interaction that overcomes this long existing limitation. Specifically, rather that spreading forces directly from and interpolating velocities directly to the nodes of the Lagrangian mesh, we instead spread forces from and interpolating velocities to quadrature points within

the interiors of the Lagrangian finite element mesh. This takes advantage of the additional geometrical information provided by the finite element description of the structure which provides information not only on the nodes of the Lagrangian mesh, but also on the material points within the mesh. Therefore, any mesh that has a quadrature scheme with sufficient orders can prevent leaks effectively. Numerical examples from Griffith and Luo [2012] demonstrate that this approach permits the use of Lagrangian meshes that are at least four times as coarse as the background Eulerian grid without leaks, which enables the analysis tailored to requirements of the structure rather than restricted by the background Eulerian mesh. In our simulations described in chapter 4 and chapter 5, we have twice dense meshes with finite element version of immersed boundary method compared to the previous work that used conventional immersed boundary method, but the time step is twice as large as the previous one, which shows that by adopting finite element spatial discretization the computational efficiency is significantly improved.

Another advantage of using the finite element version of immersed boundary method is that we can incorporate experimentally based constitutive laws for material properties. In conventional application of immersed boundary method, the elasticity of the immersed structure is considered to be systems of fibres that resist extension, compression, and exert bending stiffness. Such descriptions are easy to use, but may not be able to fully capture the hypo-elastic anisotropic material properties for subject-specific biological tissue.

Chapter 3

Effect of bending stiffness in a dynamic model of a polyurethane prosthetic mitral valve

In this chapter, we investigate the behaviour of a dynamic fluid-structure interaction model of a chorded polyurethane mitral valve prosthesis, focusing on the effects on valve dynamics including descriptions of the bending stiffness of the valve leaflets and artificial chordae tendineae Luo et al. [2012]. Each of the chordae is attached at one end to the valve annulus, and at the other to one of two chordal attachment points. These attachment points correspond to the positions where the chords of the real prosthesis would attach to the left-ventricular wall, although in our study, these attachment points were kept fixed in space to facilitate comparison between our simulations and earlier results obtained from an experimental test rig. In our simulations, a pressure gradient measured in this experimental rig drives flow through the model valve during diastole, and provides

a realistic pressure load during systole. The previous modelling studies of this mitral valve prosthesis show that the valve presents an unrealistically large orifice at beginning of diastole, and does not close completely at the end of diastole with unrealistic flutter. In this chapter, the immersed boundary method is first tested for flows in collapsible channel problem, and an excellent quantitative agreement is obtained with a well-tested in-house ALE code. We then show that, using immersed boundary method, including a description of the chordal bending stiffness enables the model valve to close properly at the end of the diastolic phase of the cardiac cycle and yields predicted flow rate which matches closely with corresponding experimental measurements. Valve over-opening is eliminated only by incorporating a description of the bending stiffness of the valve leaflets and of the chordae into the model. Thus, bending stiffness, even in such a thin structure, plays a significant role in the dynamic behaviour of the polyurethane mitral valve prosthesis.

3.1 Introduction

Heart disease is the major cause of death in the developed world. It is known, for instance, that the remodelling that occurs after a posterolateral myocardial infarction can alter mitral valve function by creating conformational abnormalities in the mitral annulus and in the posteromedial papillary muscle, leading to mitral regurgitation and ultimately requiring valve repair or replacement Einstein et al. [2010]. Each year, approximately 250,000 valve replacement procedures are carried out worldwide Yoganathan AP [2004]. More than 50 types of prosthetic valves have been developed since 1950 Vongpatanasin et al. [1996]. Yet,

six decades later, we still use devices that are less than satisfactory. Understanding valve mechanics using computational modelling represents an important step towards improved valve designs, and could lead to better diagnosis, treatment, and prevention of valvular heart diseases.

A fully three-dimensional fluid-structure interaction model of a polyurethane prosthetic mitral valve Griffith et al. [2009]; Watton et al. [2007, 2008]; Yin et al. [2010] has been studied by the heart group at University of Glasgow. In these studies, the dynamic behaviour of a three-dimensional chorded mitral prosthesis is modelled using the immersed boundary (IB) method, which accounts for the fluid-structure interaction between the blood flow and the mitral valve leaflets, although the mechanical structure of the mitral valve prosthesis is less complicated compared to the native valves. A major limitation of these earlier models is that, with the exception of Griffith et al. Griffith et al. [2009], they employ a first-order accurate IB method that results in excessive numerical dissipation.

In this chapter, we model the prosthetic mitral valve using a staggered-grid version Griffith [2012a,b]; Griffith et al. [2009] of a formally second-order accurate immersed boundary method Griffith [2005]; Lai and Peskin [2000]. We first verify the implementation of this simulation methodology by simulating the flow within a collapsible channel. Excellent quantitative agreement is obtained with the results from a well-tested in-house arbitrary Lagrangian-Eulerian (ALE) code Luo et al. [2008]. We then use this method to model the dynamics of the prosthetic mitral valve. Unlike previous work, in which the flow rate was specified at the inlet Griffith et al. [2009]; Watton et al. [2007, 2008], herein we use an experimentally measured pressure gradient to drive flow through the model valve during the diastolic phase of the cardiac cycle, and to provide a realistic pressure load

for the closed valve during the systolic phase of the cardiac cycle, enabling us to perform more realistic simulations. In this chapter, we consider the effects on the dynamics of the valve of including models of the bending rigidity of the chordae and of the leaflets. We demonstrate that when both bending effects are included in our model, our computational results agree well with experimental measurements. Our simulations therefore indicate that incorporating a model of the bending stiffness is highly important, even for structures as thin as mitral valve leaflets. Although we only present results using IB models of heart valve dynamics, we expect that our findings would also hold for other approaches for modelling the fluid dynamics of heart valves.

3.2 Mathematical formulation

In this chapter, we use the immersed boundary method as mentioned in chapter 2, with a Lagrangian description of the structure and an Eulerian description of the momentum, viscosity and incompressibility of the coupled fluid-structure system, to simulate the dynamics of a chorded polyurethane mitral valve prosthesis.

3.2.1 Continuous and discrete elasticity modelling

To describe the elasticity of the immersed structure, it is convenient to assume that the structure is described in terms of overlapping families of elastic fibres and that the Lagrangian material coordinates $\mathbf{s} = (r, s)$ have been chosen so that a fixed value of $r = r^0$ labels a particular fibre. The elastic forces generated by the immersed structure are the sum of the fibre forces due to extension and

bending:

$$\mathbf{F} = \mathbf{F}_s + \mathbf{F}_b = \frac{\partial}{\partial s}(T\boldsymbol{\tau}) + \frac{\partial^2}{\partial s^2}\left(\kappa \frac{\partial^2}{\partial s^2}\mathbf{X}\right), \tag{3.1}$$

in which $T = T(\mathbf{s})$ is the fibre tension, and $\boldsymbol{\tau}(\mathbf{s})$ is the unit tangent vector aligned in the fibre direction and κ is the bending stiffness coefficient, which is defined as

$$\kappa = \frac{EI}{\triangle \mathbf{s}^3} \tag{3.2}$$

with E denoting the Young's modulus and I denoting the cross-sectional moment of inertia. For the planar element of uniform thickness h, with fibres in r and s directions, and $\triangle r$, $\triangle s$ denoting the lengths of fibres within each element, we can compute the bending stiffness as

$$\kappa_s = \frac{EI_s}{\triangle s^3} = \frac{E\triangle r h^3}{12\triangle s^3}, \kappa_r = \frac{EI_r}{\triangle r^3} = \frac{E\triangle s h^3}{12\triangle r^3} \tag{3.3}$$

In this paper, we use a 4-node quadrilateral element to represent the valve leaflets; see Fig.3.1($Left$). Each element is comprised of 8 fibre segments, and the bending stiffness is computed from the 3-node beam element consists of a pair of adjacent fibres, as shown in Fig.3.1($Right$). See Watton et al. [2007] for a detailed description of this method for generating elastic fibres from quadratic elements. Note that in Eqs.(3.1), $\mathbf{F}_s$ corresponds to forces generated by extension- and compression-resistant elastic elements, which results in a membrane-type force, and $\mathbf{F}_b$ corresponds to forces generated by bending-resistant elastic elements, which results in a shell-like force. A linear elastic response is assumed, as justified by an earlier comparison between simulation and experiment Watton et al. [2007].

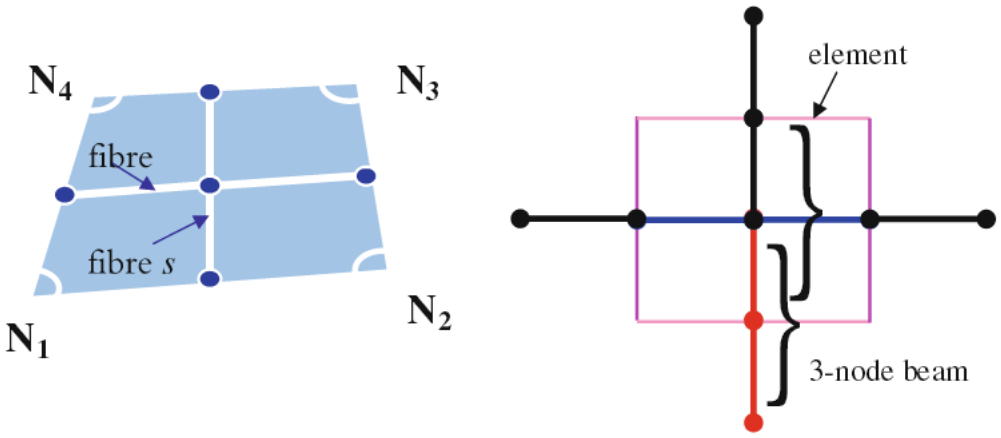

Figure 3.1: (*Left*) The 4-node element is spanned by four fibre segments; (*Right*) the bending stiffness for a 3-node beam is computed from a pair of adjacent fibre segments located within and across the element boundaries in each direction Luo et al. [2012]

3.2.2 Feedback forcing

We provide an additional Eulerian feedback-forcing term to ensure that any Dirichlet boundary conditions are satisfied at the inlet and the outlet. This additional body force, which is non zero only in the vicinity of the physical boundaries, is of the form

$$\mathbf{f}_B(\mathbf{x},t) = k(\mathbf{u}_b(\mathbf{x},t) - \mathbf{u}(\mathbf{x},t)) \tag{3.4}$$

in which $\mathbf{u}_b(\mathbf{x},t)$ is the prescribed velocity along the boundary $\partial\Omega$ of the Eulerian domain. At open boundaries, where we impose normal traction boundary conditions, we employ feedback forcing for only the tangential components of the velocity in the vicinity of $\partial\Omega$. We choose $k = \frac{\rho}{2\triangle t}$, which is approximately the largest value of k permitted by our semi-implicit time discretization.

3.2.3 Implementation

The simulations described herein employ the open-source Immersed Boundary Method with Adaptive Mesh Refinement (IBAMR) software framework (http://ibamr.googlecode.com), which provides an adaptive and distributed-memory parallel implementation of the IB method as well as infrastructure for developing FSI models that use the IB method. IBAMR leverages functionality provided by other freely available software libraries, including SAMRAI (https://computation.llnl.gov/casc/SAMRAI), PETSc (http://www.mcs.anl.gov/petsc), and *hypre* (http://www.llnl.gov/CASC/hypre).

3.3 Method verification: collapsible channel flow

3.3.1 Model description and parameters

In this section, we verify a formally second-order accurate cell-centred IB method Griffith [2005]; Griffith and Peskin [2005]; Griffith et al. [2009, 2007] implemented in the IBAMR software framework against an in-house ALE code Luo et al. [2003] on a collapsible channel flow problem. This problem is chosen because the rich dynamic behaviour of collapsible channel flows makes simulating fluid-structure interaction in such systems extremely challenging, and because, for this particular example, the ALE code satisfies the geometrical conservation law exactly Liu et al. [2012]. The numerical model consists of flow in a channel in which part of the upper wall is replaced by an elastic beam in the plane strain configuration; see Fig.3.2. The rigid channel has width D, and part of the upper wall of length L , scaled by the channel width D, is replaced by an elastic beam that is subject to

an external pressure load $\bar{p_e}$. The lengths of the upstream and downstream rigid parts of the channel are L_u and L_d, respectively, also defined in reference to the channel width D. Steady Poiseuille flow with average velocity U_0 is prescribed as a boundary condition at the inlet. The extensional and bending stiffness of the beam are EA and EJ, respectively, in which E is the Young's modulus for the plane strain problem, A is the cross-sectional area of the beam (which is equivalent to the beams thickness because the beam has unit width in the z direction), and J is the moment of inertia of the cross-section of the beam. Pretension in the beam is assumed to be zero, and the damping and rotational inertia of the beam are ignored. In the ALE code, the beam is discretized using 6-node triangular elements, whereas in the IB simulation, the beam is represented using systems of extension-, compression-, and bending-resistant elastic elements.

We mark that the physical systems modelled by the IB method and by the ALE code are slightly different. Specifically, the IB model describes a collapsible channel that is immersed in fluid, i.e. a system that includes inertial effects both within the channel and outside of the channel. In contrast, the ALE model excludes inertial effects in the exterior of the channel, thereby effectively treating the region exterior to the channel as a constant pressure reservoir Luo et al. [2008]. The dynamic behaviour of the two models therefore differs. However, if the system is stable and admits only a single steady solution, then as $t \to \infty$, transient effects will decay, and the equilibrium results of the two models will be identical. Hence, for verification purposes, we consider a stable flow case used by Liu et al. [2009a], with dimensionless parameters $c_\lambda = \frac{EA}{\rho U_0^2} = 2400$, $Re = \frac{D\rho U_0^2}{\mu} = 500$, $p_e = \frac{\bar{p_e}}{\rho U_0^2} = 1.95$, $L_u = 5$, $L_d = 30$, and $L = 5$. The corresponding dimensional parameters are $E = 0.4785$ MPa, $U_0 = 0.05$ m/ s, $\rho = 10^3$ Kg/ m^3, $\mu = 10^{-3}$ Pa,

$D = 0.01$ m, $A = 10^{-4}$ m^2, and $\bar{p_e} = 4.875$ Pa.

3.3.2 Results

The un-deformed state is used as the initial configuration. Because the wall stiffness is quite large, the largest stable time step for this problem is approximately 5×10^{-5} s. Figure 3.3(a) shows that in the IB model, the wall oscillates for approximately 17 s before settling to a steady state. This quasi-steady solution agrees very well with the results computed from a finite element model using ALE code Cai and Luo [2003] and also with results obtained using ADINA (Watertown, Massachusetts, United States); see Figure 3.3(b).

We remark that although steady-state problems, such as the one considered in this section, are well suited for use as verification tests for the IB methods, the IB method is primarily intended for simulating dynamic problems, and the performance of the IB method may not be competitive with numerical methods specifically developed for steady-state flow problems. The strength of the IB method, and of its implementation in the IBAMR software, is its ability to enable fully coupled fluid-structure interaction simulations in the dynamic setting for complex three-dimensional geometries, as demonstrate in the following section.

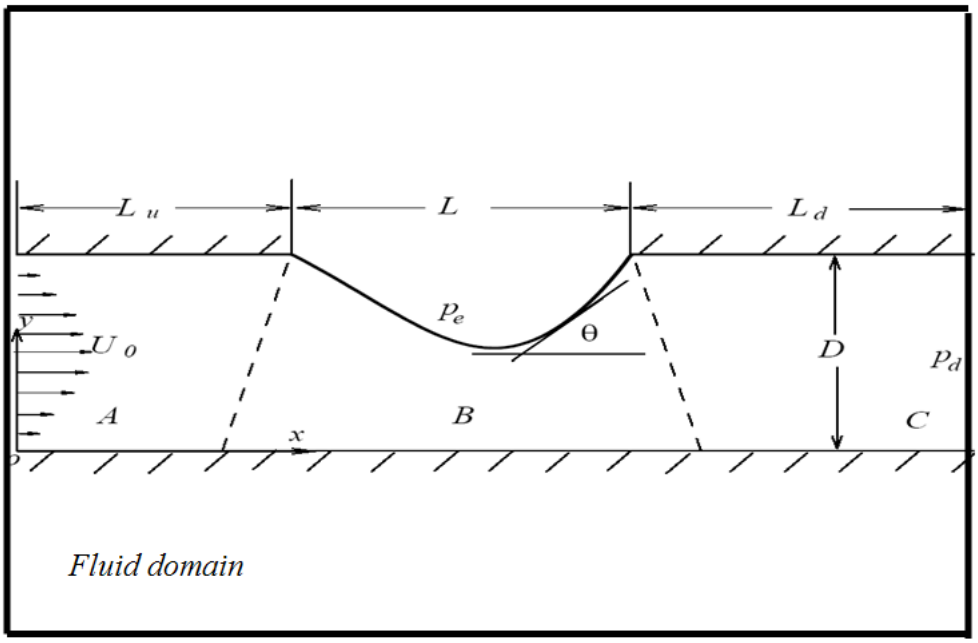

Figure 3.2: The configuration of the collapsible channel flow problem (not to scale). In section B, part of the solid upper wall is replaced by an elastic beam. In the IB version of this model, fluid is present both in the interior of the channel and in the space exterior to the channel; in the ALE model, the exterior space is treated as a constant-pressure reservoir

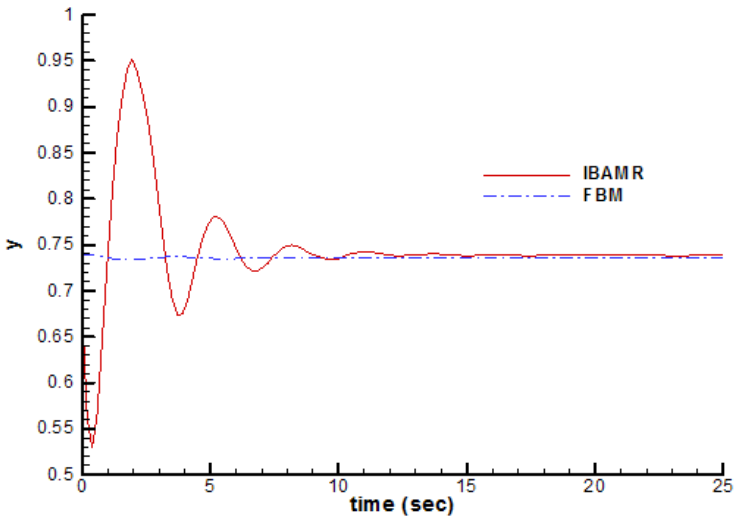

(a)

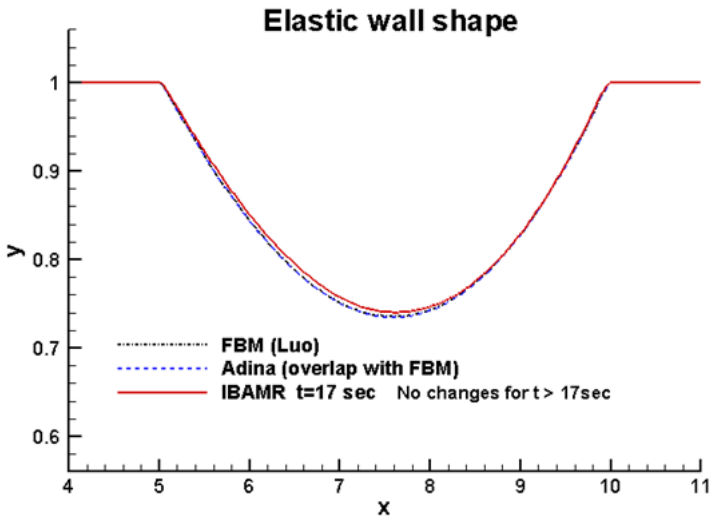

(b)

Figure 3.3: (a) The y-position of the centre of elastic beam as a function of time, and (b) The shape of the elastic wall at time t = 17 s. These results show that the transient solution determined by the IB method implemented in the IBAMR code approaches the steady solution determined by an in-house ALE code (FBM) and also the steady solution determined by ADINA. At equilibrium, all three codes produce results that are in excellent quantitative agreement. In the IB model, the elastic beam is initially flat and aligned with the rigid portions of the upper channel wall (i.e. with y = 1). The equilibrium shape shown in panel (b) therefore represents a large deformation from this initial configuration.

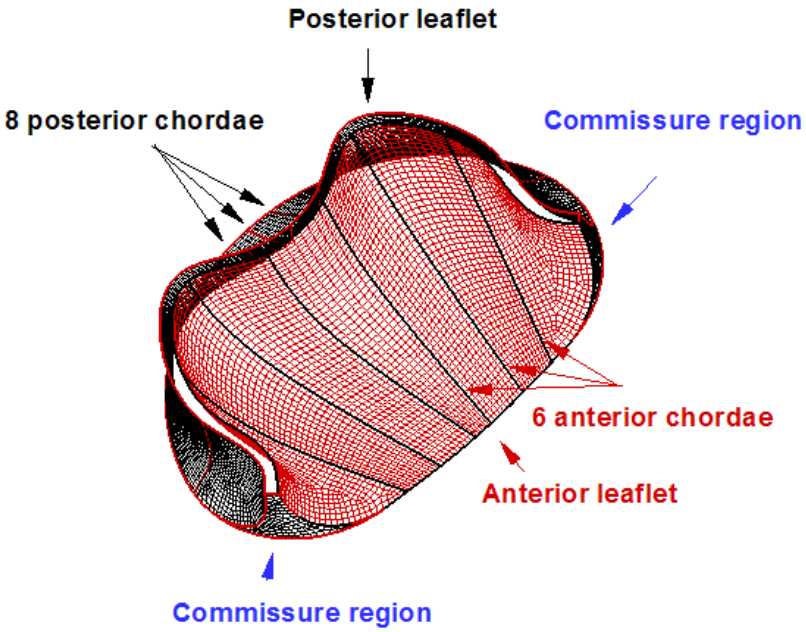

(a)

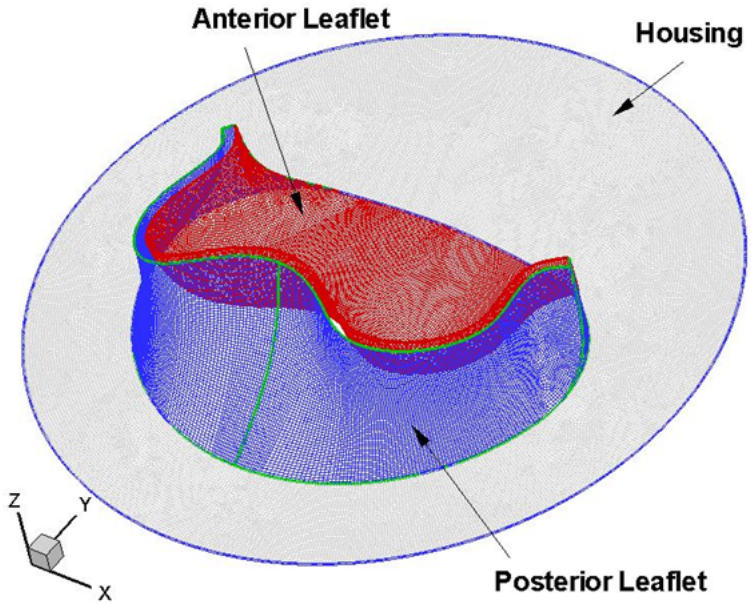

(b)

Figure 3.4: (a) The mitral valve mesh, and (b) The mitral valve mounted on a rigid housing disc. The anterior leaflet has 22,328 fibre segments, the posterior leaflet has 25,614 fibre segments and the housing disc has 43,404 fibre segments

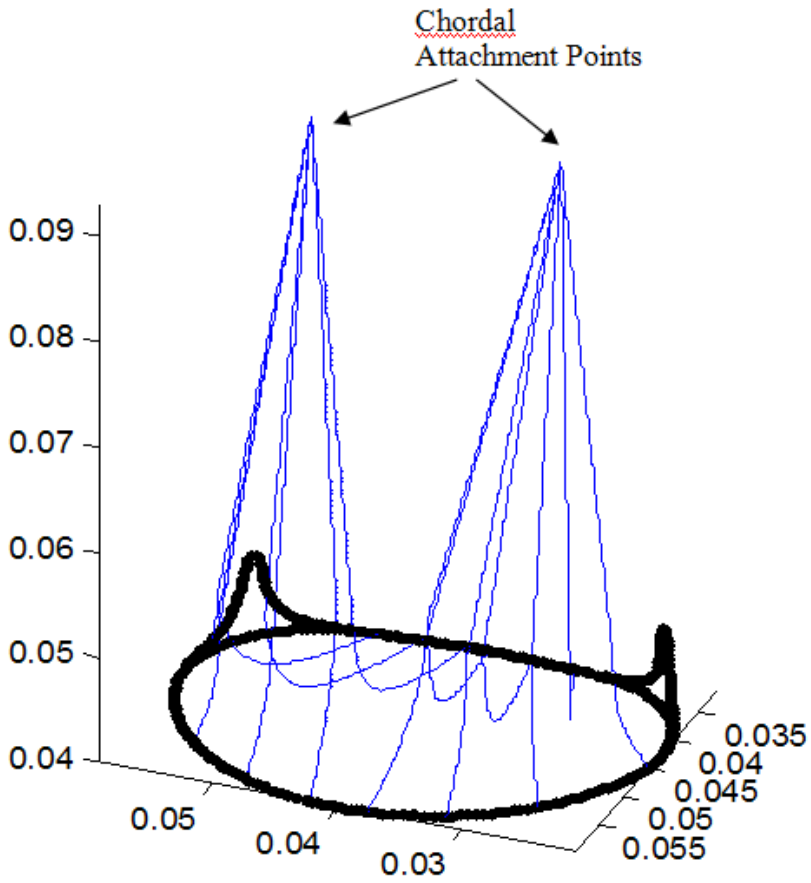

Figure 3.5: The valve annulus and artificial chordae tendineae. The semi-rigid D-shaped annulus, shown in *black*, has a post height of 7.5 mm. The model chordae, which appear in *blue*, are comprised of a total of 1,802 fibre segments. Each chord is fixed at one end to the nearly rigid annular ring and at the other to one of two chordal attachment points (CAPs). In this study, these CAPs are fixed in space to facilitate comparison between simulation and experiment

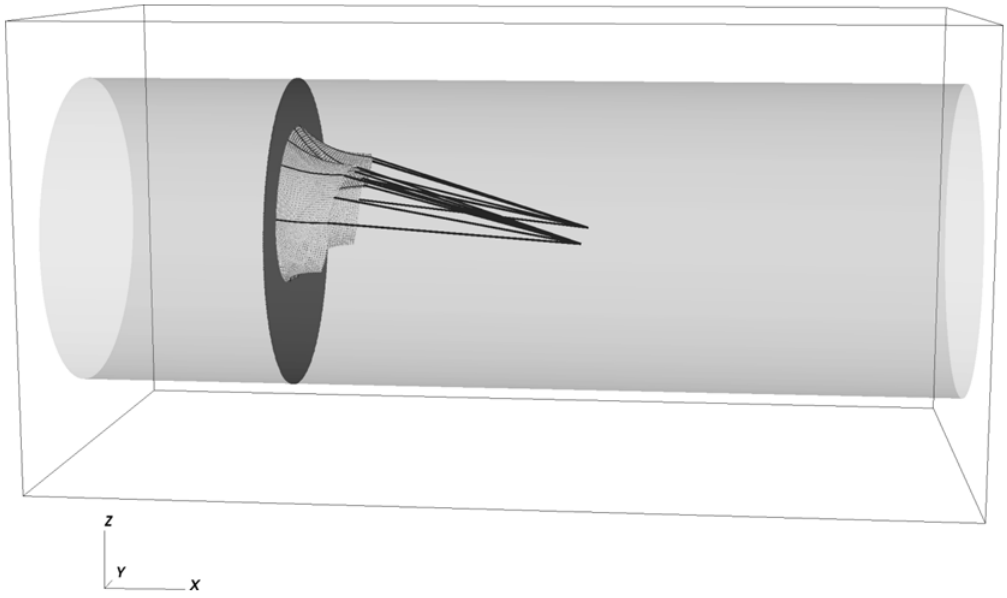

Figure 3.6: The mitral valve and the housing disc mounted in a semi-rigid circular tube of length 16 cm and diameter 5.6 cm. The valve housing is placed 4 cm downstream of the inlet of the tube. These structure are embedded in a 16 cm $\times$ 8 cm $\times$ 8 cm fluid box. A time-dependent transvalvular pressure difference is imposed across the model valve by prescribing pressure boundary conditions at the inlet and outlet of the tube

3.4 Dynamic simulation of the mitral valve prosthesis

3.4.1 Model description and parameters

The mitral valve prosthesis that we model is the same as that considered by Watton Watton et al. [2007, 2008] and by Griffith Griffith et al. [2009] and is shown in Figure 3.4. The valve prosthesis developed by D. Wheatley's group in the Department of Cardiac Surgery at University of Glasgow Wheatley et al. [2001] is made of the polyurethane material PurSpan (DSM Biomedical, Berkeley, California, United States) and incorporates artificial chordae tendineae made of Bionate 750D that originate from the valve annulus and traverse each leaflet before exiting at the free margins of the leaflets to attach to the papillary muscle regions of the left-ventricular wall. The prosthetic valve has a total of 14 artificial chordae, with eight in the posterior leaflet and six in the anterior leaflet. The valve is mounted on a rigid D-shaped annulus that attaches to the left ventricle, see Figure 3.5. The geometry of the model mitral valve is generated using the SolidWorks CAD software (Concord, Massachusetts, United States). For the purposes of the IB simulation, the model valve is further discretized as a surface that is spanned by overlapping collections of one-dimensional fibre segments, see Figure 3.1.

Each of the chordae has a cross-sectional area of 0.4 mm^2 and a Young's modulus of 30 Mpa. The leaflets have a mean thickness of 0.125 mm and are modelled as a linear elastic material with a Young's modulus of 5.4 MPa Watton et al. [2007]. Following Watton Watton et al. [2007], we assume that the valve leaflets

possess a constant stiffness and uniform thickness and that the material exhibits a linear elastic response. These approximations were tested in earlier work by Watton, who found them to be acceptable for the physiological regime of interest Watton et al. [2007]. Each chord is attached at one end to the fixed points of the annular ring and at the other to one of two chordal attachment points that are fixed in space. The mitral annulus is fixed to a housing disc that is mounted in a semi-rigid circular tube. All of these structures are immersed in a rectangular 16 cm $\times$ 8 cm $\times$ 8 cm fluid box; see Figure 3.6.

In previous work using a formally second-order accurate cell-centred IB method Griffith et al. [2009], we performed simulations using a version of this model that included a model of the bending stiffness of the chordae. In those simulations, we imposed motion of the chordal attachment points that was derived from medical imaging data, and we prescribed the experimentally measured flow rate at the inlet of the tube along with zero-pressure boundary conditions at the outlet. We found that the peak pressure was significantly reduced in comparison to the peak pressure of earlier simulations that used a first-order accurate version of the IB method. Specifically, the transvalvular pressure difference required to open the valve was about 4 mmHg, which compares favourably to the corresponding value of 12 mmHg obtained by Watton Watton et al. [2007]. We noted, however, that during the systolic phase of the cardiac cycle, the transvalvular pressure gradient was much smaller than the experimentally measured values. This is an important drawback of using flow rate as a boundary condition: the pressure load across the valve cannot be properly established.

In this chapter, we overcome this problem by imposing time-dependent pressure boundary conditions at both the inlet and outlet of the model. Specifically, we

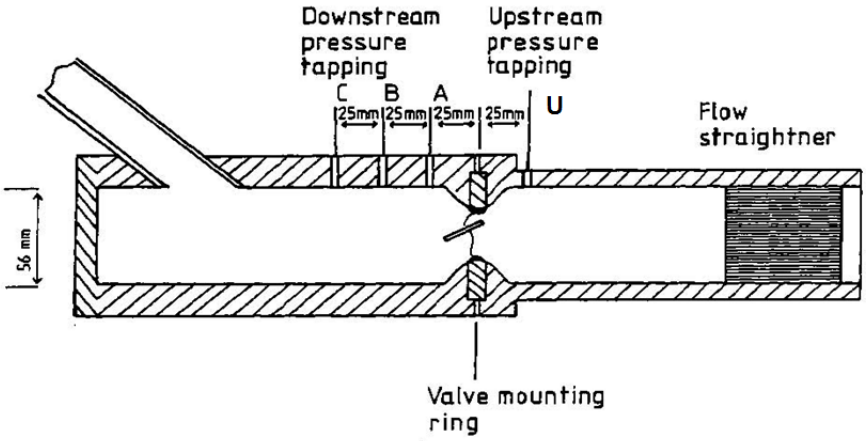

(a)

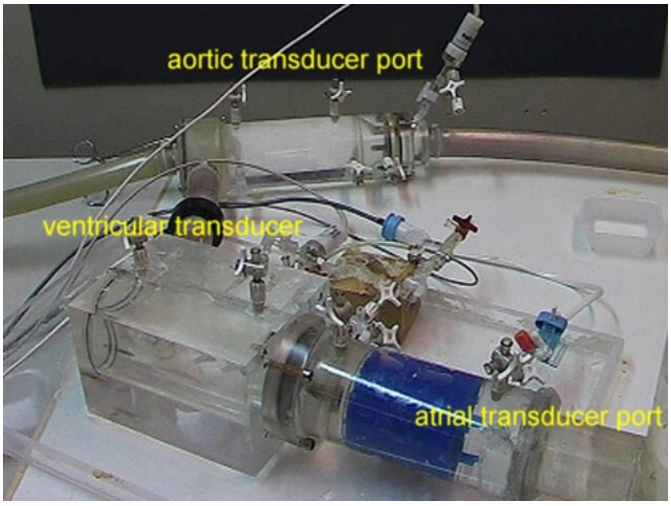

(b)

Figure 3.7: (a) Schematic diagram of the experimental apparatus described by Fisher et al. Fisher et al. [1986], in which flow is driven by a computer-controlled pump that generates pulsatile inflow. (b) The prosthetic mitral valve function test apparatus developed by D. Wheatley's group in the Department of Cardiac Surgery at University of GlasgowWheatley et al. [2001]. To avoid turbulence, the tubular Perspex section upstream from the valve is filled with straws that act as flow strengtheners. In the experiments, the flow volume was 80 ml per cycle, with a cycle duration of 0.75 s, and the mean downstream pressure was 95 mmHg. The transvalvular pressure difference was measured between stations U and B.

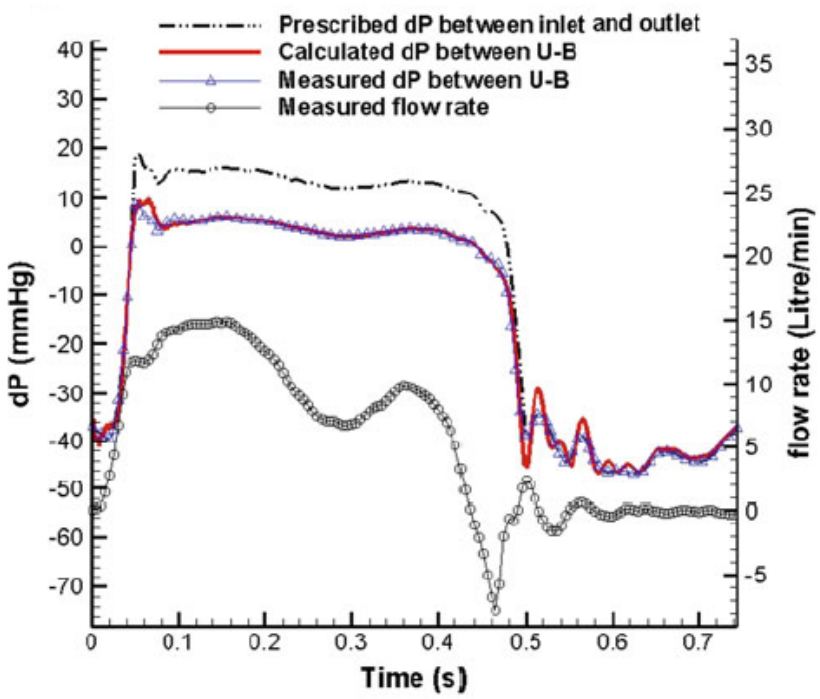

Figure 3.8: The prescribed transvalvular pressure difference, which is imposed over the 16 cm tube (*dashdot*), and the computed pressure difference between stations U and B (*solid*) are compared to the experimentally recorded pressure difference (*solidwiththriangles*). The corresponding experimental flow rate is also shown (*solidwithcircles*)

impose a pressure difference $dP_{exp}(t)$ based on measurement obtained from experiments that used a prototype of the valve prosthesis by D. Wheatley's group Wheatley et al. [2001]. A schematic diagram and the experimental apparatus is shown in Figure 3.7(a), Figure 3.7(b). For a detailed description of the experimental apparatus used, see Fisher et al. [1986]. The measured pressure difference $dP_{exp}(t)$ was determined from two pressure transducers: one that was placed at 2.5 cm upstream of the valve, identified as station U in Figure 3.7(a), and another that was placed 5 cm downstream of the valve, identified as station B in Figure 3.7(a). Notice, however, that we employ a flow chamber that is 16 cm long. This length was chosen to reduce the influence of the boundary conditions on the dynamics of the model. A consequence of this, however, is that we cannot use the experimental pressure measurements directly as boundary conditions for the model. Were we to do so, the simulated pressure difference in the model measured at stations U and B would generally be smaller than the experimentally measured difference in pressures at those locations. Moreover, the corresponding flow rates would also be smaller. Rather than using the experimental measurements directly as boundary conditions for our model, we instead set $dP(t) = dP_{exp}(t)+dP_{shift}(t)$, in which $dP_{shift}(t)$ is an additional driving pressure that is intended to offset the additional flow resistance presented by the longer flow chamber used in the simulations. The value of $dP_{shift}(t)$ is empirically determined so that the difference in the computed pressure between stations U and B is in good agreement with the experimental measurements, see Figure 3.8.

Boundary conditions are also required for the portions of the fluid box that are exterior to the inlet and outlet of the flow chamber. Solid-wall boundary conditions are prescribed along the portions of the $x = 0$ cm and $x = 16$ cm boundaries

that are exterior to the circular tube, and zero-pressure boundary conditions are imposed along the remainder of the domain boundary.

Our simulations use a formally second-order accurate staggered-grid IB method Griffith [2012a,b]; Griffith et al. [2009]. The time step size was set to be $\triangle t = 1.25 \times 10^{-5}$ s . This time step size was empirically determined to be approximately the largest stable time step size permitted by the model. Therefore, computing a complete 0.75 s cardiac cycle requires 6 million time steps, which required approximately 4 days on a Dell Unix workstation (dual quad-core Intel Xeon X5450 3.0 GHz processors).

3.4.2 Results

To investigate the effect on valve dynamics of accounting for the bending stiffness of the leaflets, two simulations are carried out. In one simulation, we include the bending stiffness of the chordae but not of the valve leaflets; in the other simulation, we account for both chordal and leaflet bending stiffness. The simulated valve opening sequences, as viewed from the inlet boundary of the circular tube in which the valve is mounted, are shown in Figure 3.9 and Figure 3.10 panels (a) and (b). The corresponding experimental recordings are shown in Figure 3.9 and Figure 3.10 panel (c). Note that while the valve is open, the posterior chordae are clearly more taut than the anterior chordae. This is a consequence of the particular design of this mitral prosthesis. Specifically, the motion of the posterior leaflet is more constrained than that of the anterior leaflet. Notice that this phenomenon is observed both in the simulations and in the experiment. This design defect also causes large strain and stress, as discussed in previous studies

Watton et al. [2007, 2008].

Figure 3.9 and Figure 3.10 clearly demonstrate that the best agreement between simulation and experiment is obtained when both the chordal and the leaflet bending stiffness are included in the model. In particular, the model that includes leaflet and chordae bending rigidity does not suffer from over-opening at the beginning of diastolic phase. From our previous research Watton et al. [2007, 2008], when we neglect the bending stiffness of the leaflets, the leaflets are overly flexible, permitting the development of a much larger orifice in comparison to the experimental results. In fact, in the case when only leaflets bending rigidity is included, part of the anterior leaflet still exceeds the boundary of the annulus while in the case when both leaflets and chordae bending stiffness are included, such over-opening phenomenon is not observed. These results also suggest that chordal bending rigidity plays an important role in proper valve closure. The fact that the chordae exert forces that act to close the valve is clearly seen in the side view in Figure 3.11 at $t = 0.4$ s. A similar phenomenon can also be seen in the experimental pictures around this time; see Figure 3.9 and Figure 3.10(c).

The fluid pressure field generated by the model is shown in Figure 3.12 at times when the valve is fully open and is fully closed. The valve opens at a driving pressure difference of approximately 8 mmHg, and is subject to a significant, physiological pressure load when closed. These diastolic loading conditions are substantially more realistic than those of the earlier simulations.

The flow rates yielded by the model with and without leaflet bending stiffness are shown in Figure 3.13. It is interesting to see that if we only include the chordal stiffness, the computed flow rate is much larger than the experimental data, because the valve over-opens and yields an unrealistically low resistance

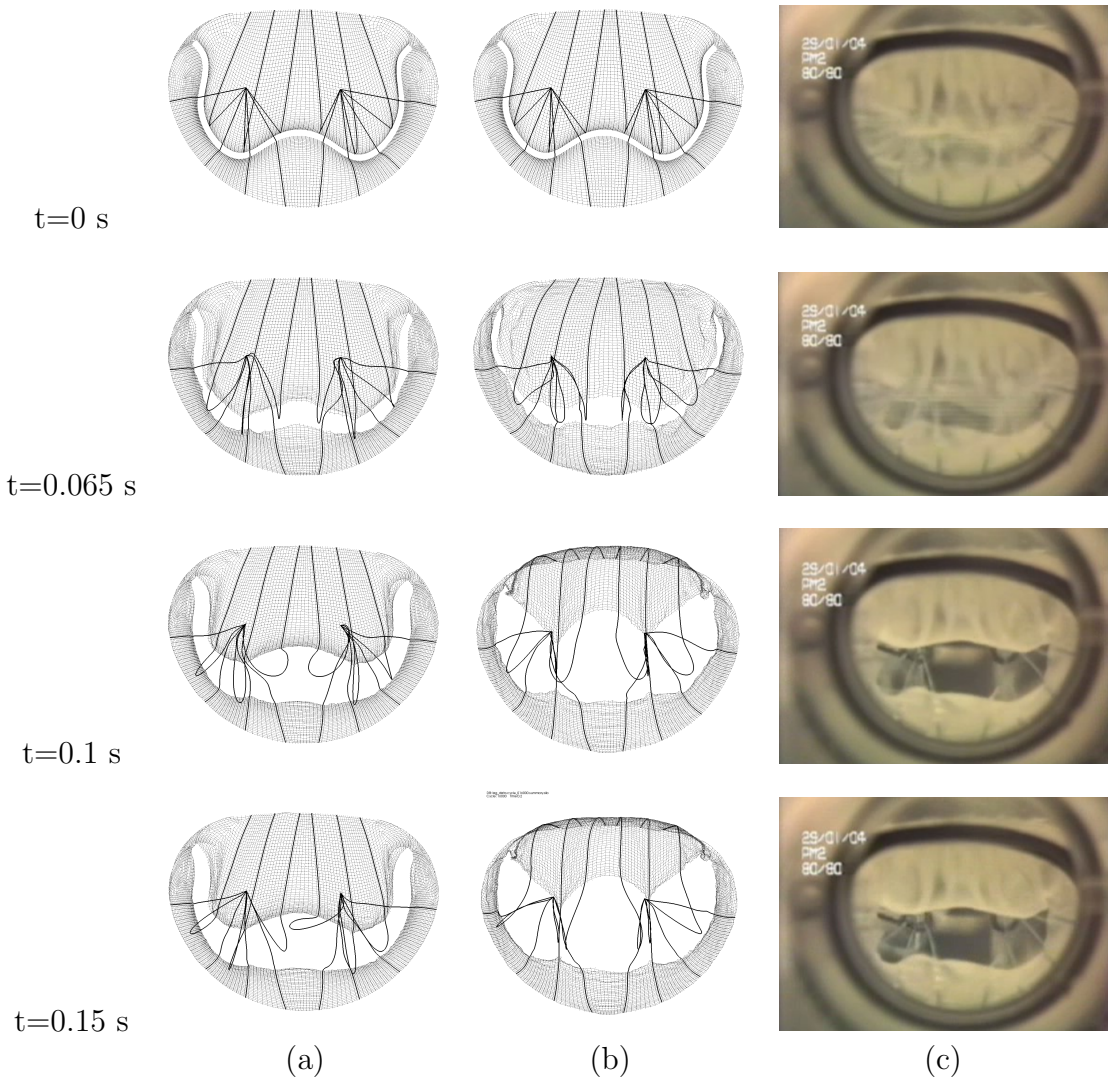

Figure 3.9: View of the mitral valve from the inflow boundary during first half cycle (0 - 0.1 s). (a) The model valve with both chordal and leaflet bending stiffness, (b) the model valve with only chordal bending stiffness, and (c) the experimental recording. The bending stiffness of the chordae assist in valve closure; however, to prevent over-opening of the valve leaflets, it is necessary also to include leaflet bending stiffness in the model.

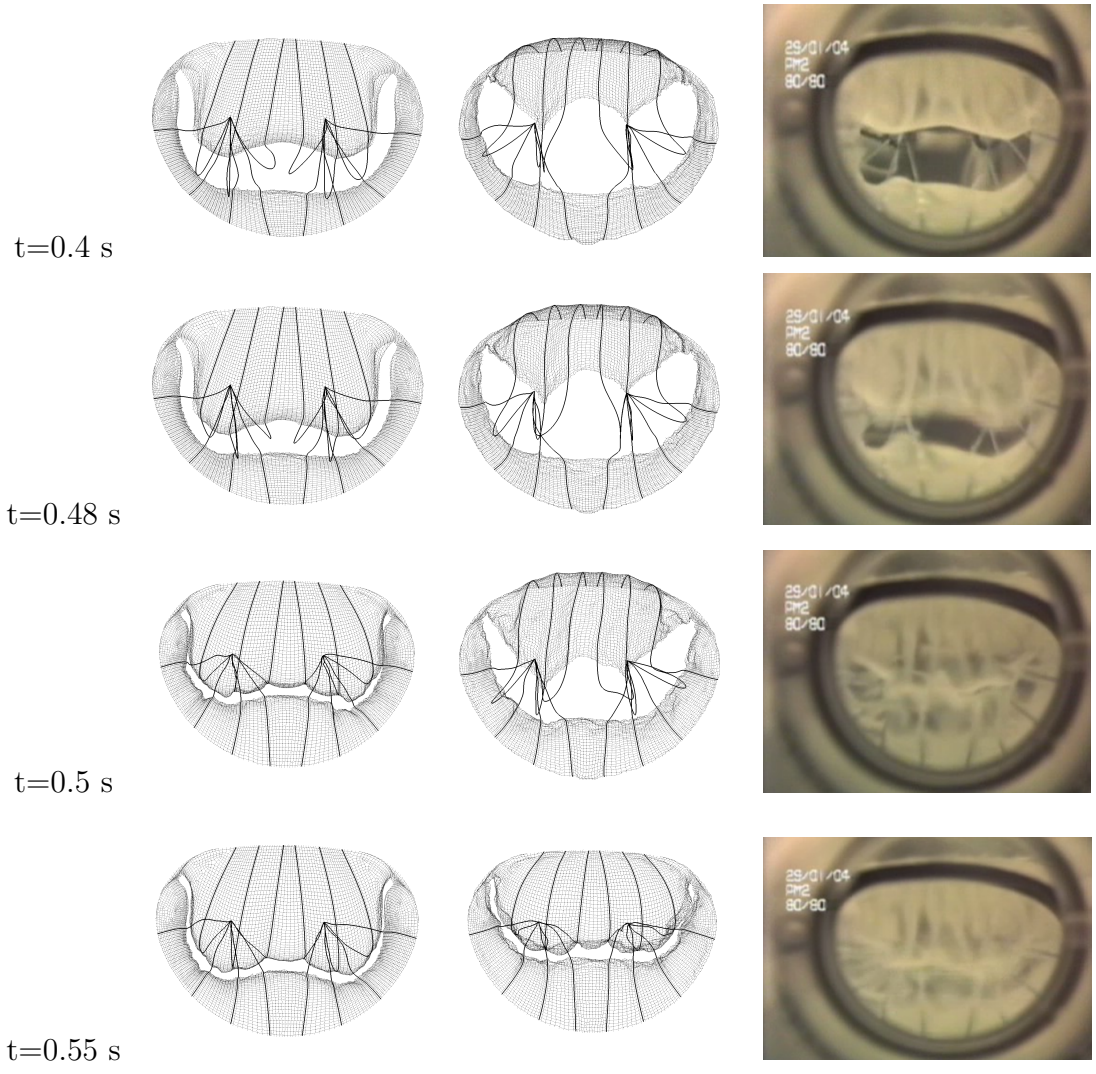

Figure 3.10: View of the mitral valve from the inflow boundary during second half cycle (0.15 - 0.55 s). (a) The model valve with both chordal and leaflet bending stiffness, (b) the model valve with only chordal bending stiffness, and (c) the experimental recording. The bending stiffness of the chordae assist in valve closure; however, to prevent over-opening of the valve leaflets, it is necessary also to include leaflet bending stiffness in the model.

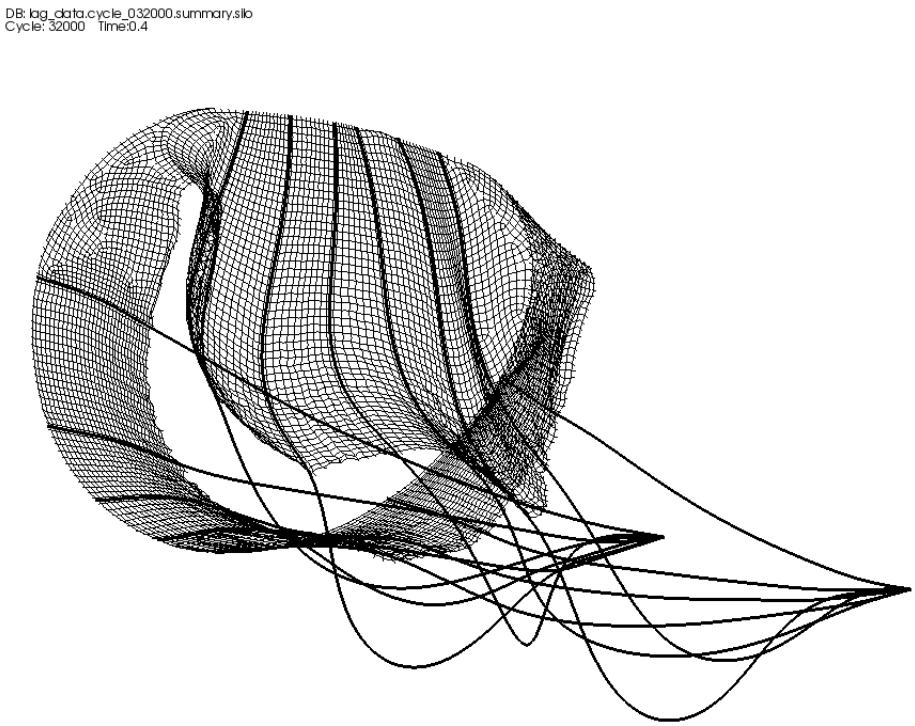

Figure 3.11: View of the model mitral valve, with both leaflet and chordal bending stiffness, showing that the chordae help to close the valve at $t = 0.4$ s

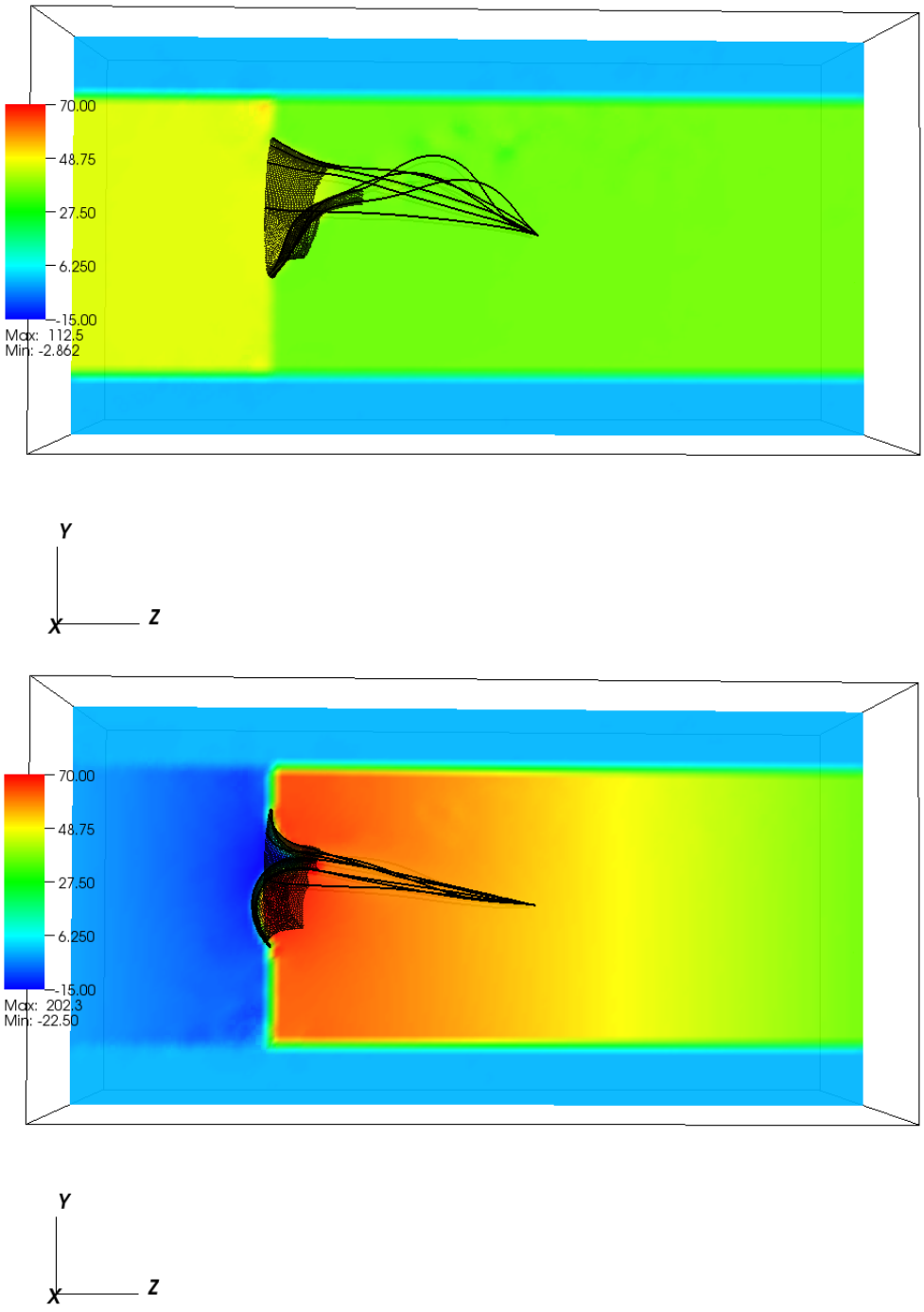

Figure 3.12: The fluid pressure field along a plane bisecting the model valve, shown when the mitral valve is fully open and fully closed. We remark that a realistic pressure load can be established when the valve is closed only by using pressure boundary conditions at both the inlet and the outlet of the model

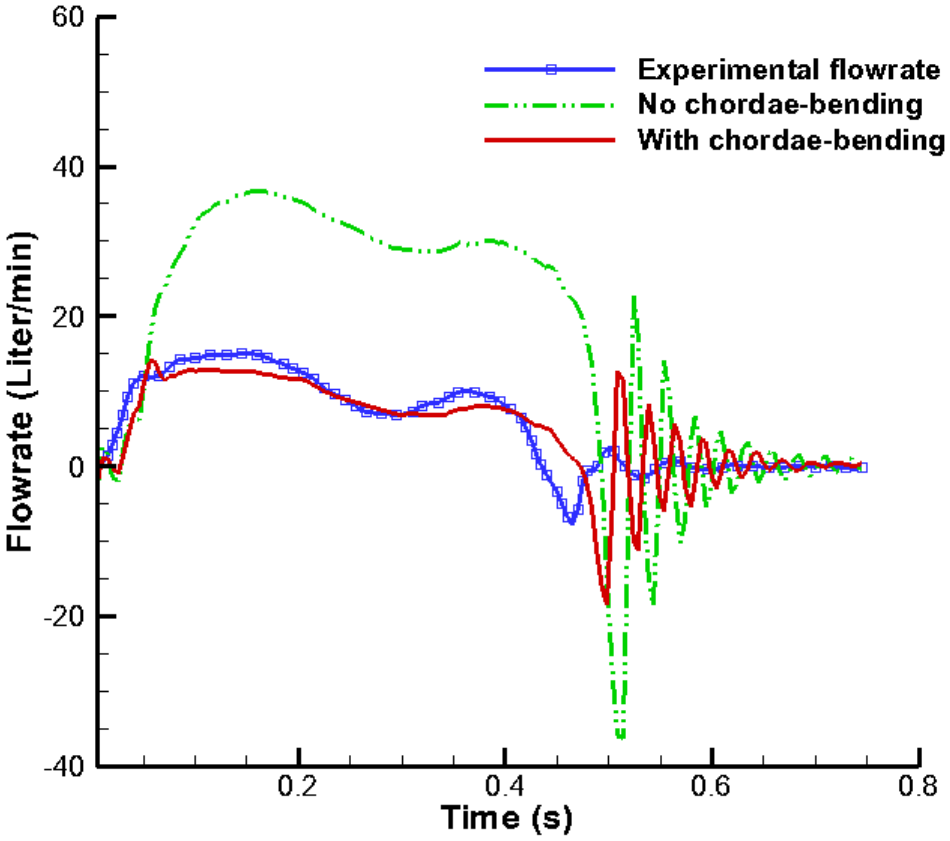

Figure 3.13: Flow rates computed by the IB MV models with and without chordae-bending stiffness, along with flow rates measured from the experimental test rig shown in Figure 3.7. Agreement between the model results and the experimental data is best when the model includes both chordal and leaflet bending stiffness

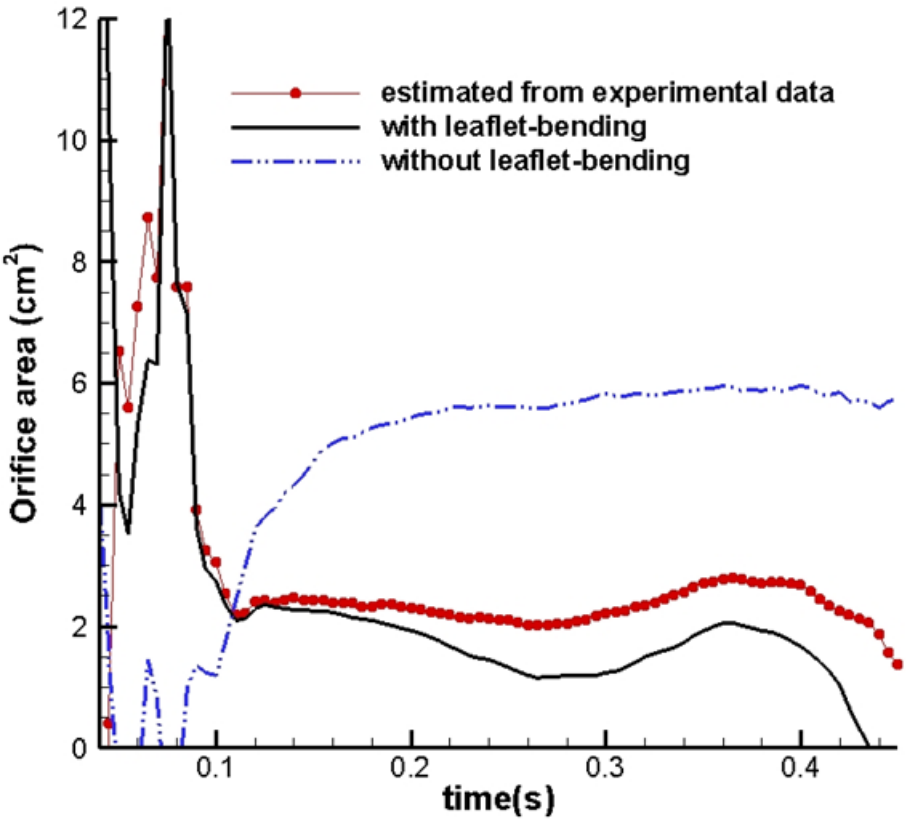

Figure 3.14: Effective valve orifice area as a function of time during the opening phase, estimated with the Gorlin formula as described in results

to forward flow. Adding bending stiffness to the leaflets leads to a much closer agreement between simulation and experiments, including reduced oscillations in the flow record after valve closure.

The simulated and experimental effective valve orifice areas are plotted in Figure 3.14. These quantities are estimated using the Gorlin formula Gorlin and Gorlin [1951b],

$$A = C\frac{Q}{\sqrt{dP_{UB}}} \tag{3.5}$$

in which A is the effective orifice area in cm^2, Q is the flow rate in ml/ s, dP_{UB} is the pressure difference between stations U and B in mmHg, and $C = 1/(0.7 * 44.5 * 0.06)$ is an empirical constant Rapaport [1985]. It should be mentioned that the Gorlin formula is derived from a simplified description of fluid dynamics that can result in inaccuracies if the flow transients are strong, as occurs during valve opening and closure. We remark that the normal orifice area of a native mitral valve is 4-6 cm^2, whereas the estimated orifice area in both the experiment and in the simulation with leaflet bending forces is only about 2.5 cm^2, suggesting the need for further improvement to the current design.

3.5 Discussion and conclusion

In this study, we presented simulation results obtained via a fluid-structure interaction model of a chorded prosthetic mitral valve, and we compared these results to measurements obtained from corresponding experiments using a real valve prosthesis. Our model accounted for both the chordal and leaflet bending stiffness, and it used a formally second-order accurate immersed boundary method. Previous simulations by this group using a first-order accurate immersed bound-

ary method and periodic boundary conditions Watton et al. [2007, 2008]; Yin et al. [2010] suggested that the model mitral valve would not close unless additional pressure is added. This study shows that, by including the chordal bending force in the model, the closure dynamics of the valve are improved significantly. Unless we include leaflet bending stiffness in our model, however, the valve leaflets remain overly flexible. Specifically, without such bending-resistant forces, the valve over-opens during the initial portion of the diastolic phase of the cardiac cycle, resulting in a valve orifice that is significantly larger than observed in corresponding experiments. Much better agreement in valve orifice size is achieved when we include the valve leaflet bending force. In addition, non-physical oscillations that occur upon valve closure are greatly reduced when such forces are included in the model. These findings highlight the importance of accounting for the bending stiffness in the dynamic simulation of the mitral valve.

The current model has been improved from our previous mitral valve models Griffith et al. [2009]; Watton et al. [2007, 2008]; Yin et al. [2010] in several important aspects. Pressure boundary conditions are imposed, and the mechanical representation has been improved by accounting for the bending rigidity of the leaflets and the chordae. In addition, the model predictions are much closer to experimental data throughout the cardiac cycle, including both the opening and closing phases. We have also performed a quantitative verification of the present IB method for a challenging problem in collapsible channel flow.

The present work also has several limitations. First, the mechanical structure of the mitral valve is modelled quite simply as a mesh of elastic fibres, and the bending stiffness is only provided along each fibre. This may contribute to the discrepancy between the predicated results and the experimental data, a discrepancy

that is reduced but not eliminated by the present model; see Figure 3.9, Figure 3.10 and Figure 3.13. To better model the non-linear mechanical behaviour of the mitral valve leaflets, it may be important to use a modelling approach that permits more sophisticated elasticity models. One approach would be to employ a finite element discretization of the valve, and to use experimentally characterised strain-energy functionals to describe the elasticity of the valve leaflets. Extensions of the immersed boundary method that permit such FE-based elasticity models have been developed over the past decade Boffi et al. [2008]; Griffith and Luo [2012]; Liu et al. [2006]; Zhang and Gay [2007]; Zhang et al. [2004], and one such extension of the IB method is already implemented within the IBAMR software used to perform the simulations described in chapter 5 Griffith and Luo [2012]. Second, although more realistic pressure boundary conditions are implemented in the present simulations, these boundary conditions do not include any feedback mechanisms that are able to adjust the flow and pressure resulting from compliances in the experimental set-up. We believe that the lack of realistic compliance in the loading conditions is the principal reason for the oscillations seen after t = 0.5 s in our simulations. Future work on incorporating more realistic loading conditions is clearly required. Third, the annular ring in our model is assumed to be planar and fixed in space, whereas in case of a native valve, it is saddle shaped and deformable. In fact, in the real valve prosthesis, even though is not strictly planar,the annulus is rigid, accounting for this in the model may not be required to obtain realistic chordal force distributions and leaflet stresses Prot et al. [2009]. Finally, although the mitral valve is generally described as a passive structure, Prot and Skallerud [2009] found that their finite element mitral valve model yields unrealistic deformations when the active muscle fibres of the anterior

leaflet are neglected. A passive model of the mitral valve leaflets is appropriate in the present setting, in which we are modelling a passive polyurethane mitral valve prosthesis; however, the results of Prot and Skallerud suggest that our model may be of limited use if applied to interpret the behaviour of a native mitral valve.

In summary, we have successfully simulated the dynamic behaviour of a chorded mitral valve prosthesis and, in doing so, highlighted the importance of accounting for the bending stiffness of the leaflets and artificial chordae tendineae of the valve prosthesis. Although our observations are drawn from an immersed boundary model of the mitral valve prosthesis that describes the elasticity of the valve in terms of systems of elastic fibres, we believe these findings would apply equally to native mitral valve with more traditional continuum-based descriptions. That is to say, we expect that a valve leaflet model that does not account for bending stiffness is unlikely to perform adequately in the dynamic setting. Therefore, constructing the realistic, dynamical models of the cardiac valves that are needed to improve clinical outcomes for the large number of patients suffering from valvular heart diseases will require either a shell-type formulation, like that used in the present work, or a fully three-dimensional description of the elasticity of the cardiac valves.

Chapter 4

Image-based fluid-structure interaction model of the human mitral valve

The human mitral valve (MV) consists of a large anterior-medial leaflet and a smaller posterior-lateral leaflet, which are both connected to the left ventricular papillary muscles via multiple fibrous chordae tendineae. As cardiovascular diseases are the leading cause of death worldwide, an understanding of mitral valve bio-mechanics is pivotal for optimization of surgical procedures aimed at restoring normal mitral valve function in pathological subjects. Computational models can realistically capture the main anatomical and functional features of the mitral valve, hence provide detailed spatial and temporal data that may not be easily obtained experimentally. In this chapter, an in-vivo human mitral valve geometry model is derived from magnetic resonance imaging (MRI) data, and then solved using the Immersed Boundary Method with Adaptive Mesh Refine-

ment (IBAMR) Griffith et al. [2009] under a physiological left-atrium-ventricle pressure loading.

High resolution anatomical imaging was performed on a healthy 28-year-old volunteer using a 3T MRI system (Siemens). A stack of MR images (3-mm slice thickness) were obtained in an apical long-axis left ventricular outflow tracts (LVOT) view to cover the entire mitral valve. A MATLAB-based GUI interface was developed to load, interpolate and assemble the coordinates of segmentation landmarks, which was then put into the CUBIT tool suite for reconstructing the in-vivo 3D mesh. Using the immersed boundary method, we have simulated the dynamics of the patient-specific mitral valve model under realistic left-atrium pressure loading. Analysis shows that the patient-specific mitral valve geometry has a significant influence on the simulation results. We quantitatively validate the computed orifice area, opening configuration and flow with clinical measurements. Our framework of the integrated human mitral valve simulations may be developed to provide further tools for mitral valve therapy planning.

4.1 Introduction

Comprehensive assessment of mitral valve physiology and patho-physiology requires detailed modelling of patient anatomy and dynamics, and for such assessments to be clinically useful, they must be based on noninvasive imaging data. Dynamic modelling of mitral valve biomechanics is made challenging by the large deformations experienced by the leaflets, the anisotropic nonlinear elastic behaviour of the valvular tissue, and the pulsatile haemodynamic loads during the cardiac cycle. In addition, there is large inter-subject variability in the anatomy

of the mitral valve apparatus. Imaging techniques such as magnetic resonance (MR) imaging and echocardiography Gabriel et al. [2005] allow the visualisation of the cardiac valves and provide data needed to link anatomy to valvular function, but such imaging modalities do not yield information on the loads applied to the valve that arise from the coupled fluid and structural dynamics of the valve and the blood Lau et al. [2010]. Numerical simulation has the potential to provide detailed biomechanical data, such as in vivo loads and tissue stresses, that may not be easily determined by standard clinical or experimental techniques. Therefore, imaging-derived computational models that account for the observed physiological conditions are an avenue to further quantitative and qualitative insight into valvular function. Such data could be used to develop quantitative methods for determining patient-specific medical and surgical strategies for the treatment of valvular heart diseases.

Computational studies of the mitral valve have been performed by a number of groups, many of whom have used structural modelling to study mitral valve biomechanics Lim et al. [2005]; Prot et al. [2010]; Skallerud et al. [2011]; Votta et al. [2006, 2007]. Because of the strong interaction between the blood flow with the mitral valve leaflets and the left ventricular wall, models of the full dynamic behaviour of the mitral valve require the description of fluid-structure interaction (FSI) Lau et al. [2010]. Kunzelman, Einstein, and co-workers were the first to use a three-dimensional fluid-coupled computational model to simulate normal and diseased mitral function Einstein et al. [2003, 2005]; Kunzelman et al. [1993, 1997, 1998]; A limitation of most of these studies is that the valve geometries have typically been taken to be symmetric about the mid-line of the anterior and posterior leaflets Lim et al. [2005]; however, the mitral valve is a fully three-

dimensional structure.

In chapter 3, we have developed a fully three-dimensional FSI model of a prosthetic mitral valve Luo et al. [2012], in which the dynamic behaviour of a chorded polyurethane mitral prosthesis was modelled using the immersed boundary (IB) method, which accounts for the fluid-structure interaction between the blood flow and the mitral valve leaflets. We also demonstrated the effects of incorporating a model of the bending rigidity of the valve leaflets and chordae, which are needed to obtain accurate flow rates and open configurations, despite the fact that mitral valve leaflets are extremely thin structures. However, unlike the natural valve, this prosthesis is in fact symmetric about the mid-lines of the leaflets.

In this chapter, we exploit the same immersed boundary method as described in chapter 2 and chapter 3, and describe dynamic modelling of the human mitral valve that uses patient-specific anatomy derived from MR imaging data along with physiological loading conditions. In our simulations, the image-derived mitral valve model is mounted in a semi-rigid tube, and dynamic boundary conditions are imposed at the inlet and outlet of this tube to produce physiological transvalvular pressure differences. The equations of fluid-structure interaction are solved using a staggered-grid version Griffith [2012a,b] of a formally second-order accurate IB method Griffith and Peskin [2005]; Lai and Peskin [2000]. We use families of elastic fibres that resist extension, compression, and bending to model the thin mitral valve leaflets and the chordae tendinae, using measured human mitral valve material properties Clark [1973]; Clark and Butterworth [1971]; Ghista and Rao [1972]; Kunzelman et al. [1993]; Lim et al. [2005]; McDonald et al. [2002]. We use a physiological driving pressure waveform Levick [2012] to simulate a complete cardiac cycle.

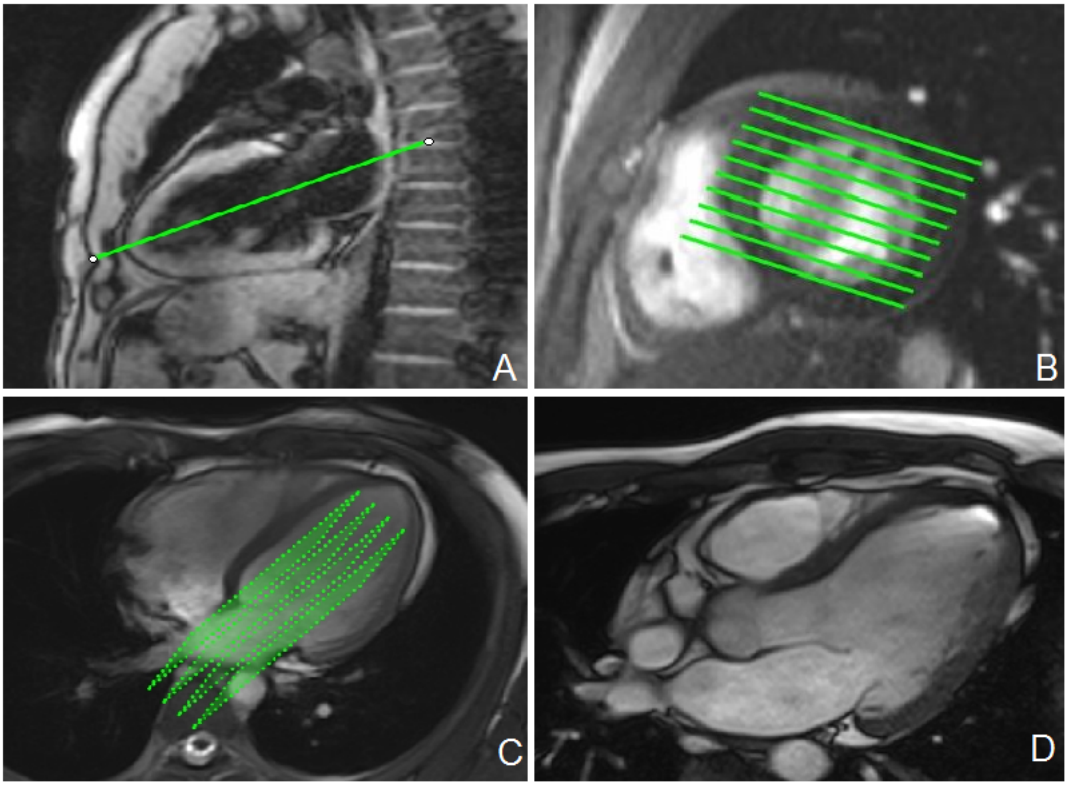

Figure 4.1: Magnetic resonance images of the mitral valve. (a) Illustration of the image coordinate defining the valve position; (b) Illustration of the image plane positioned to cover the whole valve (top view from left atrium along long axis); (b)Illustration of the image plane positioned to cover the whole valve (4 chamber view);(d) Left ventricle outflow tract of the mitral valve MR image showing the anterior and posterior leaflets

4.2 Human mitral valve model

4.2.1 Geometry reconstruction from magnetic resonance images

A cine MR scan was performed on a healthy 28-year-old male volunteer using a 3-Tesla MRI system (Verio, Siemens, Germany). Thirteen planes including the left ventricular outflow tract (LVOT) were used for mitral valve imaging to cover

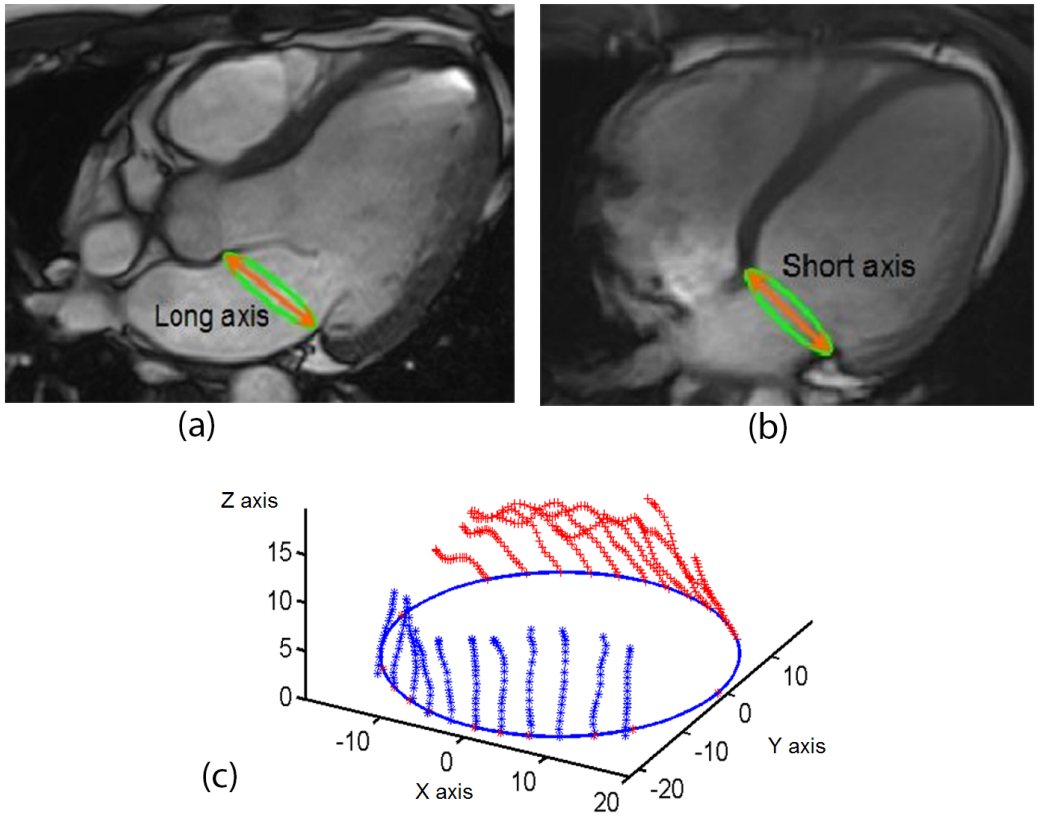

Figure 4.2: Mitral valve reconstruction. (a) Mitral annulus measurement from a long-axis slice of the valve. (b) Mitral annulus measurement from a short-axis four-chamber view. (c) The final manual segmentation determined from images assembled along the annulus ring.

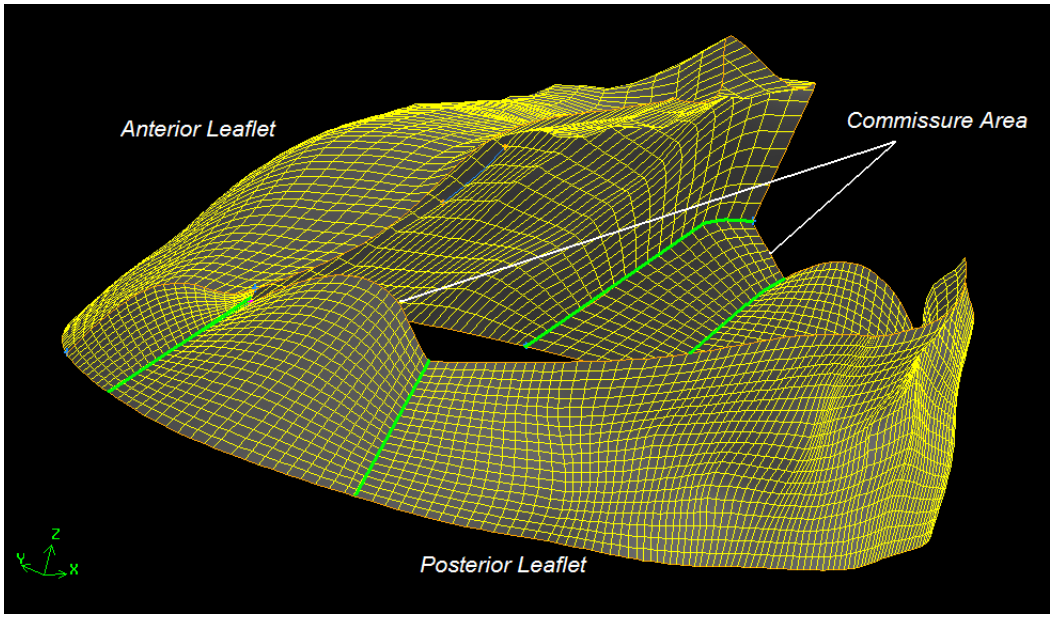

Figure 4.3: Anterior and posterior leaflet meshes.

the entire mitral valve, as shown in Figure 4.1(a), indicated by the green lines superimposed on the two-chamber view. The parameters for the mitral valve MRI scan were: slice thickness: 3 mm with 0 mm gap; matrix size: 432×572; pixel size: $0.7 \times 0.7\ mm^2$; frame rate: 25 per cardiac cycle. The mitral valve was reconstructed at the middle of diastole when the mitral valve is opened fully using an in-house graphic user interface implemented in MATLAB (The MathWorks Inc., Natick,MA,United States), see detailed process in Appendix A.

The general steps for mitral valve reconstruction included:

- *Annulus ring reconstruction.* For simplicity, the annulus ring was assumed to be an ellipse projected on a plane defined by the mitral valve long axis and short axis shown in Figure 4.2(a, b).

- *Two-dimensional leaflet segmentation.* Mitral valve leaflets were manually segmented on LVOT views using two detached lines to represent the anterior

and posterior leaflets. MR images for the same views at other times were also used to help identify mitral valve boundaries.

- *Leaflet assembly.* Mitral valve leaflet segmentations from the stack of images were assembled along the reconstructed annulus rings as shown in Figure 4.2(c).

- *Mesh generation.* The assembled leaflet were imported into CUBIT to construct the final three-dimensional mesh.

Figure 4.3 Shows the final mesh obtained from the CUBIT mesh generation software. The leaflet surfaces are very irregular, with a concave surface in the front of the anterior leaflet and a convex face close to the annulus when facing the left ventricle.

4.2.2 Material properties of the mitral leaflets

It has been reported that the modulus of elasticity of the mitral valve leaflets does not vary significantly with deformation Miller et al. [1981]. We therefore model the mitral valve leaflets as a linear isotropic material with a Young's modulus of 0.8 MPa following previous studies on sheep mitral valve Kunzelman et al. [1993]; Lim et al. [2005]. Lim et al. also assumed that the thickness of the leaflets is uniform Lim et al. [2005]. In this approach, we consider two approaches to determine the thickness of the leaflets, following the measurements on a human mitral valve McDonald et al. [2002]. One approach assumes that both leaflets have the same uniform thickness of 0.94 mm, and the other sets the thickness of the anterior leaflet to be 0.97 mm and the thickness of the posterior leaflet to be 0.92 mm McDonald et al. [2002].

4.2.3 Chordae tendinae

We include descriptions of only the primary chordae tendineae. In our model, these are attached to the free margin of the leaflet and run through the leaflets to the annulus ring. The number and location of the chordae are based on anatomical descriptions Muresian [2009]; Sakai et al. [1999]. Each of the chordae is attached to one of two points positioned in a plane 40 mm above the annular plane that are taken to represent the papillary muscle groups. A total of 22 evenly distributed marginal chordae are defined and between the papillary tips and leaflet free edges Hammer et al. [2008]; Votta et al. [2008], with 14 associated with the posterior leaflet and 8 with the anterior leaflet; see Figure 4.4. Both the mitral annulus and the papillary tips are fixed in space. The resting lengths of the chordae are set to be longer than their initial lengths to provide slack that permits the leaflets to close when subjected to a realistic systolic pressure load. Each of the chordae was assumed to have a uniform cross-sectional area of 1.15 mm^2 and an elastic modulus of 22 MPa Kunzelman et al. [1997].

4.2.4 Driving and loading conditions

We simulate the valve dynamics for a complete cardiac cycle of 0.7 s, starting at mid-diastole, which was the time at which the MR images used to construct the leaflet geometry were obtained. It is convenient to specify the pressure difference between the inlet and outlet of the tube in which the mitral valve is mounted. Because subject-specific transvalvular pressure data were not available, we instead use a typical physiological pressure profile based on human clinical data Levick [2012]. A similar approach was adopted in previous mitral valve models Prot

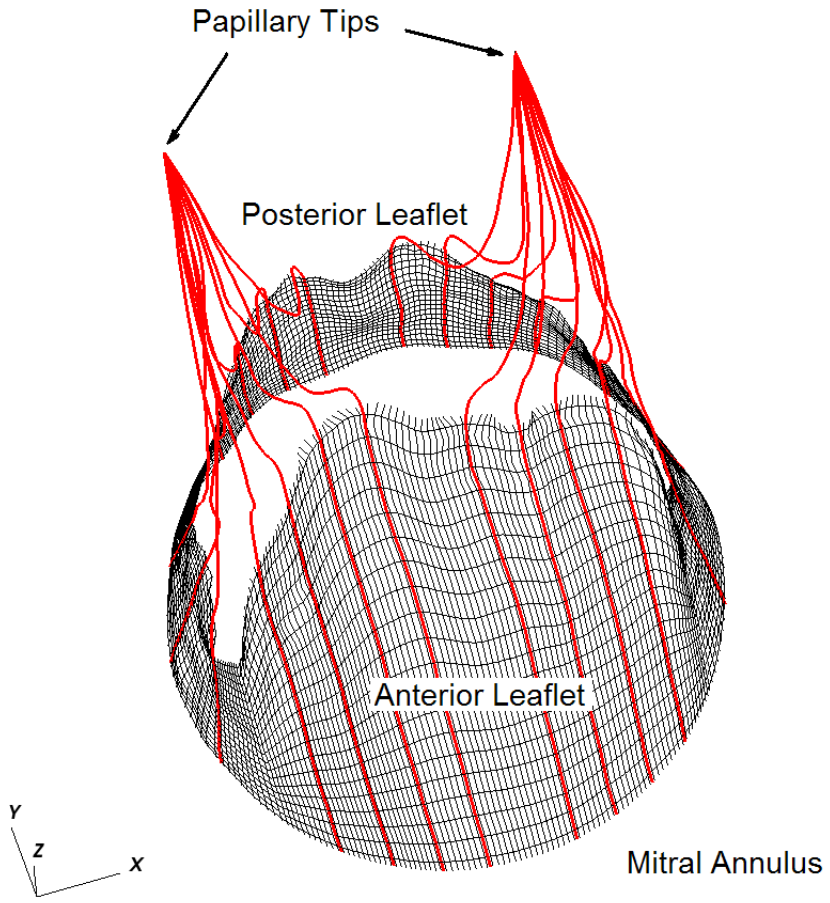

Figure 4.4: A total of 22 marginal chordae are defined between the papillary tips and leaflet free edges. In our simulations, the papillary tips and the mitral annulus are fixed in place.

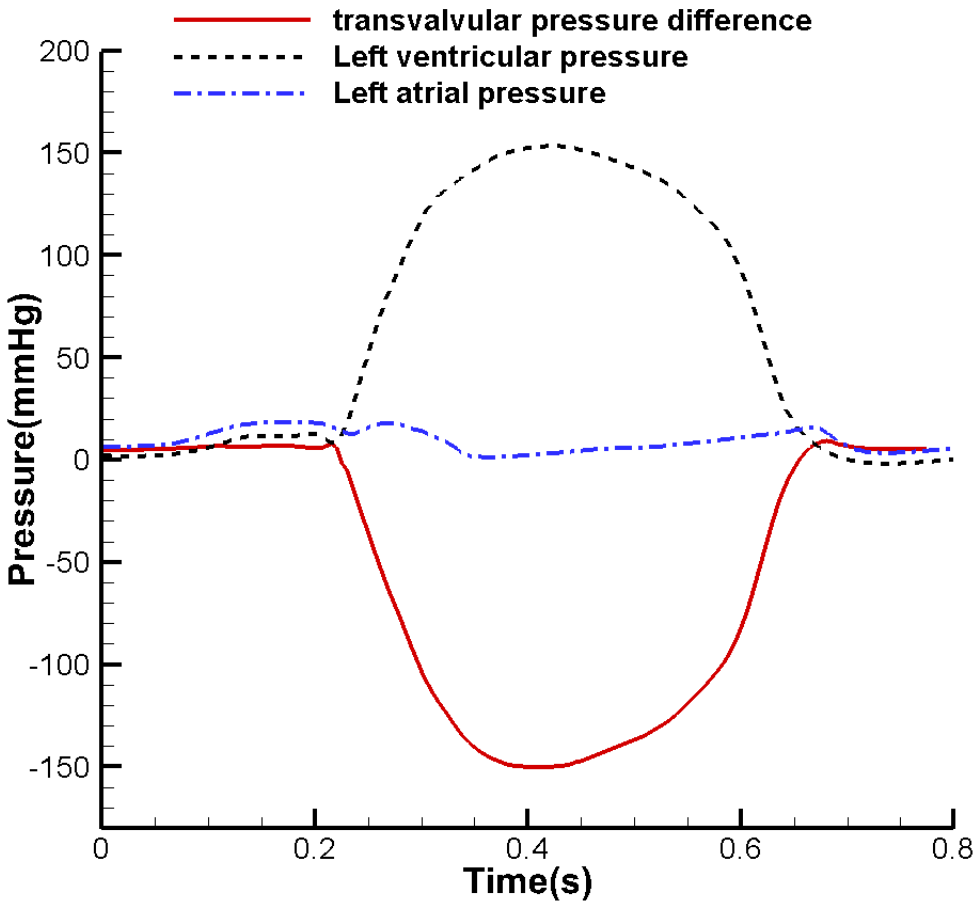

Figure 4.5: Typical time courses of the left ventricular (green) and left atrial (blue) pressures. The left ventricular pressure has scaled to match the peak systolic pressure of the volunteer. The difference between these curves is the transvalvular pressure difference (dash-dot) imposed in the simulations. In our simulation, we particularly assume that the complete cardiac cycle is from 0 to 0.7 s

et al. [2009]; Stevanella et al. [2011b]. Here we have rescaled the data so that the peak systolic pressure is 150 mmHg, matching that of the volunteer; see Figure 4.5.

4.3 Computational results

In the simulations, the mitral valve annulus is fixed to a housing disc that is mounted in a semi-rigid circular tube that is immersed in a 16 cm $\times$ 8 cm $\times$ 8 cm fluid box, as shown in Figure 4.6. A transvalvular pressure gradient is prescribed across the length of the tube, and zero-pressure boundary conditions are employed along the remainder of the domain boundary Griffith et al. [2009]. The fluid pressure and instantaneous streamlines generated by the model are shown in Figure 4.7 when the valve is fully open and is fully closed. The valve opens at a driving pressure of approximately 10 mmHg and is subject to a physiological downstream pressure load of 150 mmHg when fully closed. Our simulations use a formally second-order accurate staggered-grid IB method Griffith [2012a,b]; Griffith et al. [2009]. In our simulation, the time step size was set to be $\triangle t = 1.25 \times 10^{-5}$ s, with 42576 elements in total. This time step size was empirically determined to be approximately the largest stable time step size permitted by the model. Therefore, computing a complete 0.7 s cardiac cycle requires 5.6 million time steps, which required approximately 6 days on a Dell Unix workstation (8-cores Intel Xeon X5450 3.0 GHz processors).

The closed and open configurations of the model valve are shown in Figure 4.8 along with the corresponding MR images. Notice that in the septilateral direction, the MR image shows that the anterior leaflet surface was convex (with

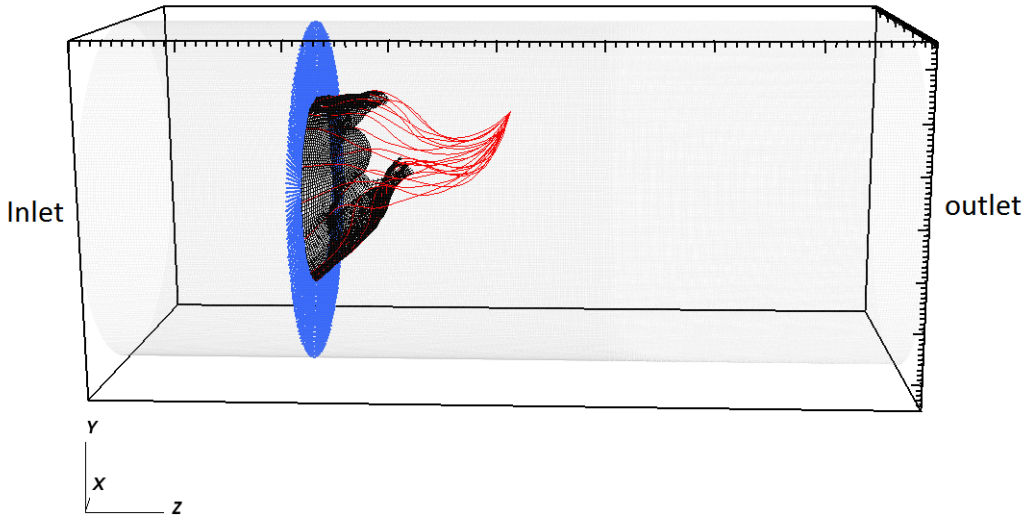

Figure 4.6: The mitral annulus is fixed to a housing disc and mounted at the location of $z = 4$ cm in a semi-rigid circular tube of length 16 cm. The valve apparatus, including the valve leaflets and chordae tendinae, are attached to the annulus. These structures are all immersed in a 16 cm $\times$ 8 cm $\times$ 8 cm rectangular fluid box.

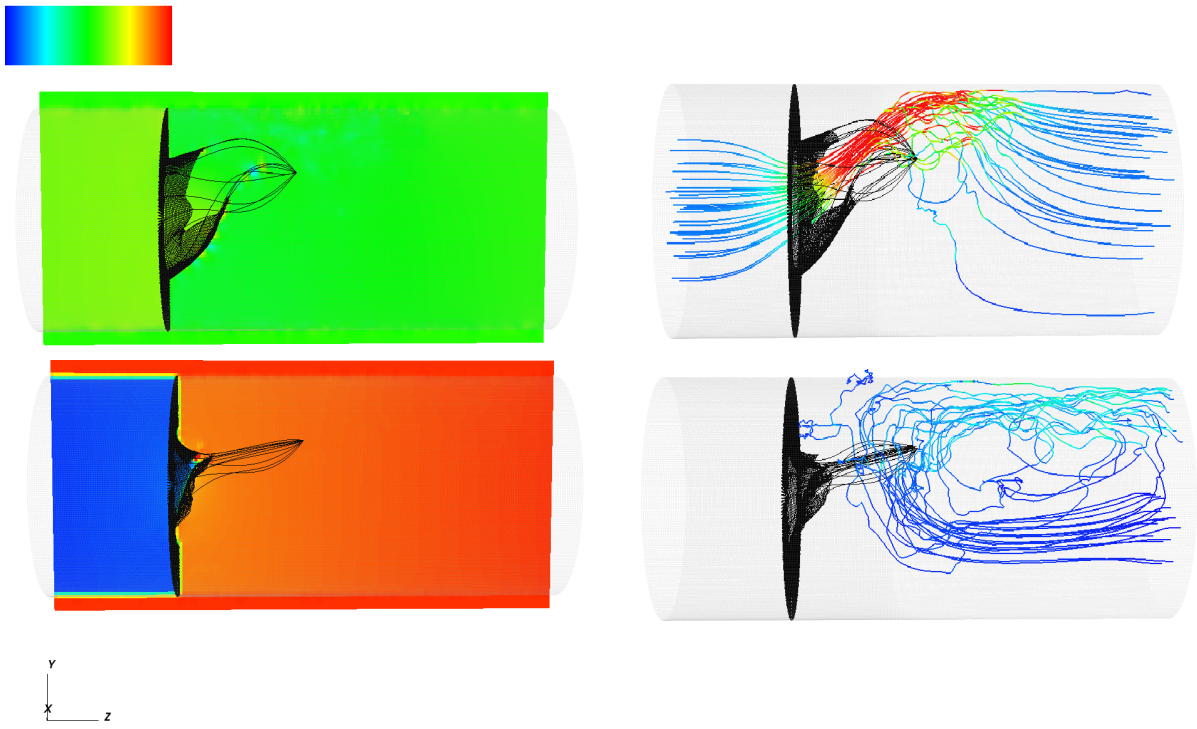

(a) (b)

Figure 4.7: (a) The fluid pressure field along a plane bisecting the mitral valve, shown when the mitral valve is fully open (top), plotted from -1.5 mmHg to 5.6 mmHg, and fully closed (bottom), plotted from -150 mmHg and -0.75 mmHg. (b) The corresponding instantaneous streamlines of the flow, coloured by the velocity magnitude (top: from 0 to 2.3 m/s , originated from inlet, and bottom: from 0 to 0.35 m/s , originated from outlet).

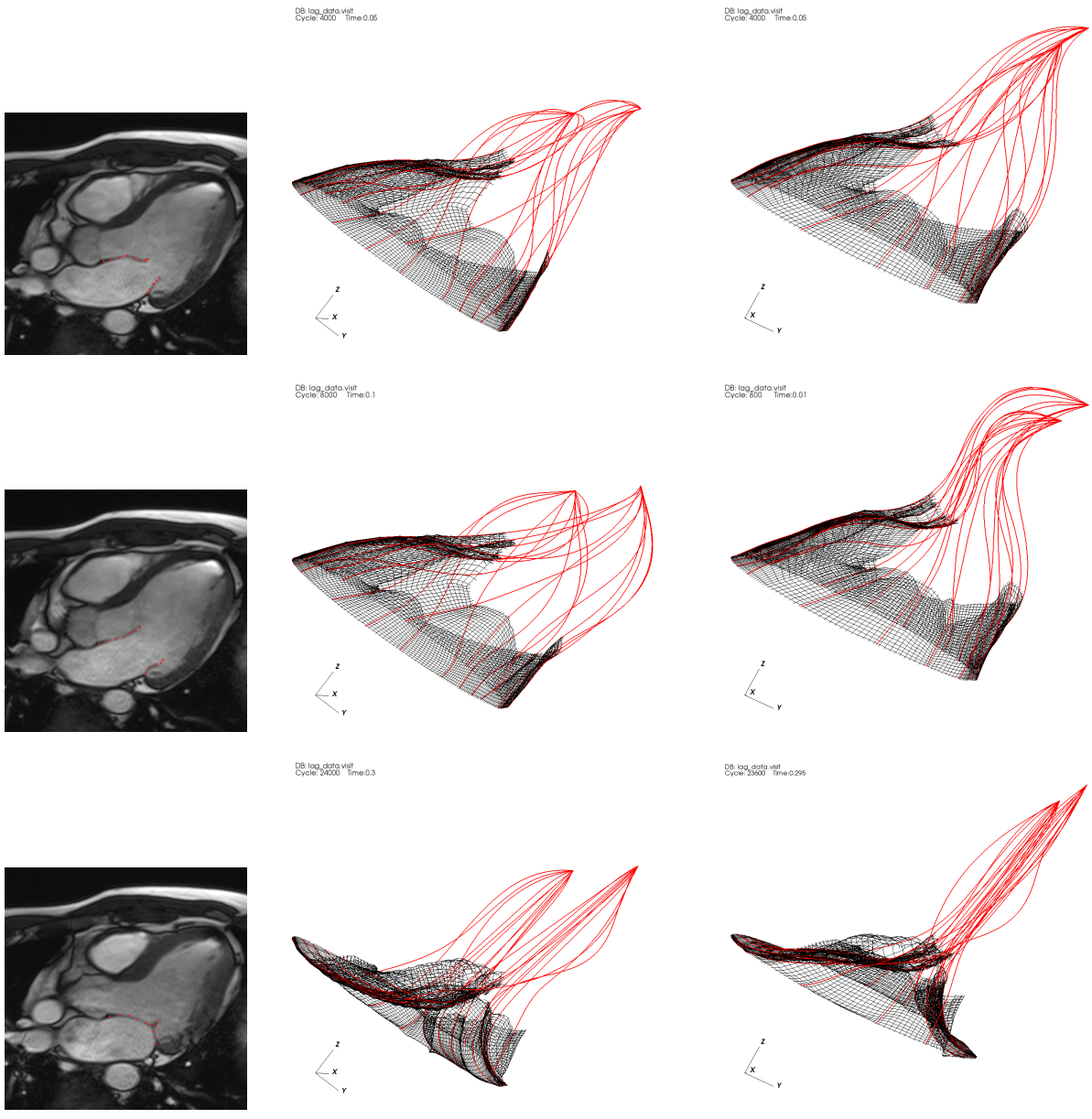

Figure 4.8: Side view of the mitral valve at the end of diastole ($t = 0.005$ s, top); fully opened ($t = 0.1$ s, middle); and early systole ($t = 0.3$ s, bottom). (a) MR imaging data; (b) model results obtained when using a uniform thickness for the two leaflets; and (c) model results obtained when using different thickness for the anterior and posterior leaflets. Notice the model that includes differences in the thickness of the leaflets is in better agreement with the clinical data.

respect to the left ventricle) near the annulus and concave near the free edge throughout systole and diastole. Such a pattern is consistent not only with reports from animal models Karlsson et al. [1998]; Kvitting et al. [2010] but also with experimental observations in human Ryan et al. [2008]. In our simulations, the aforementioned curvature pattern can be seen in diastole when we use either a uniform leaflet thickness or different thicknesses for the anterior and posterior leaflets, but is only observed in systole when we use different thicknesses for the leaflets. A more detailed comparison of results obtained when using these different assumptions is shown in Figure 4.9, where the chordae embedded in the anterior leaflets are used to show the shape of the leaflet. These results make it clear that when we assume that both leaflets have same thickness, the stiffness of the anterior leaflet is underestimated and stiffness of posterior leaflet is overestimated.

The flow rate through the valve is shown in Figure 4.10. It again demonstrates that the model that uses different thickness for the anterior and posterior leaflets leads to a closer agreement to the measurements, and also reduces the oscillations that occur when the valve is closing. We remark that the second peak in the measured flow rate is due to regurgitant flow that occurs at the onset of atrium systole. This additional ventricular loading is not considered in our simulation.

4.4 Discussion and conclusions

In this study, we described the development of an anatomically realistic human mitral valve model based on in vivo MR imaging data, and we presented fully three-dimensional FSI simulations using this model under physiological, dynamic

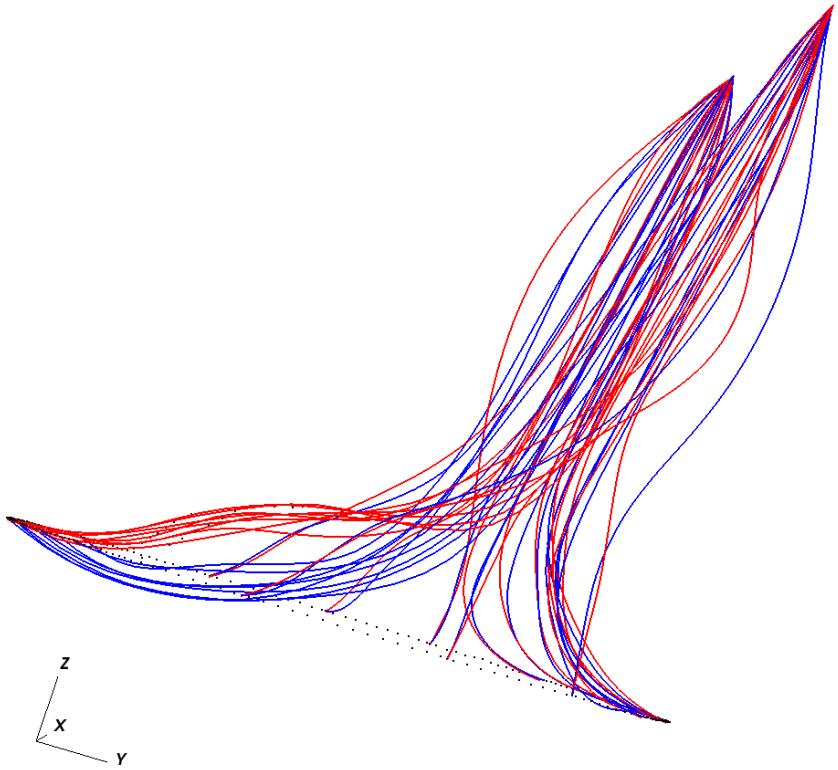

Figure 4.9: The shape of the mitral valve in the closed configuration as shown by fibres embedded in the leaflets for the cases in which different thickness are used for the leaflets (red-solid) and the case in which the same thickness is used for both leaflets (blue-dotted). This view shows that the anterior leaflet is convex near the annulus and concave near the free edge only when we use different thickness for the two leaflets.

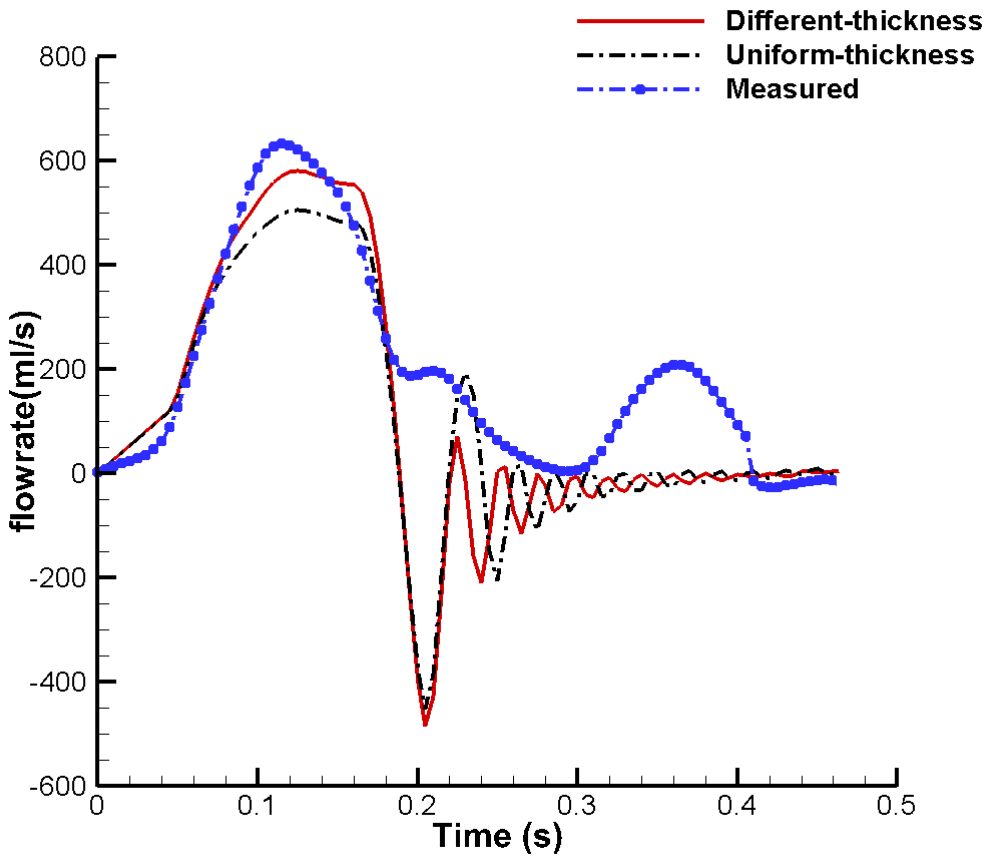

Figure 4.10: Flow rates produced by the mitral valve models along with clinical flow data obtained from phase contrast cine MRI measured across the mitral valve orifice. Agreement between the model results and the experimental data is best when the model includes different thickness for the anterior and posterior leaflets. We don't compare the flow rate after 0.45 s for the mitral valve is fully closed and the flow rate converges to 0.

transvalvular pressure loads. An initial validation of the model is provided by comparing the computed opening shape and flow rates to clinical measurements from the volunteer who provided the anatomical data used to construct the model. Recent in vivo studies have highlighted the importance of anterior leaflet shape in mitral valve closure Stevanella et al. [2011b]. The anterior leaflet was observed clinically to be convex (with respect to the LV) near the annulus, and concave close to the free edges in the septilateral direction Karlsson et al. [1998]; Kvitting et al. [2010]; Ryan et al. [2008]. This shape is observed in our simulations, but only when we assign physiological thickness McDonald et al. [2002] to the two leaflets. These results suggest that differences in the thickness of the leaflets play an important role in maintaining the physiological curvature of the mitral valve. Accounting for the difference in the thickness of the leaflets also reduces the effective resistance of the valve and increases the flow rate during diastole, yielding better agreement between the computed flow rate and the clinical data. The flow rate is proportional to the opening orifice of the mitral valve Gorlin and Gorlin [1951a], which is one of the key aspects in mitral valve performance. These results highlight that these thickness differences also have an important functional role.

We note, however, that there still exists some degree of discrepancy between the computed and the measured flow rate, particularly at the flow decelerating phase - much greater oscillations are seen in the computed flow rate compared to the measured one. We comment that this is primarily due to the lack of realistic compliance in the loading condition in our model Luo et al. [2012]. In this model, we also assumed the uniform thickness within each leaflet. In the real valve, however, the thickness is not spatially uniform McDonald et al. [2002]. All these

could have additional impacts in the shape changes but have not been taken into account in this work. Another improvement need to be done is that the annulus ring constructed in this chapter is an ellipse orifice projected on the annulus plane, whereas in case of a native valve, it is saddle shaped and deformable. In chapter 5, we improve the mitral valve geometry for incorporating saddle shaped annulus and then compare the differences in valve opening and closing between case with planar annulus and case with saddle shaped annulus.

It was convenient to develop the initial geometrical model of the mitral valve leaflets from a fully open configuration. We also kept the mitral annulus and papillary muscle tips fixed in space. Doing so required us to set the resting lengths of the chordae to be longer than their initial lengths to allow the valve to close when subjected to a physiological pressure load. A more realistic approach, not considered here, would be to consider the kinematics of the papillary tips, as done previously Watton et al. [2008]; Yin et al. [2010].

Another limitation of this work is the relatively simple isotropic material model that is used to describe the mitral valve leaflets. The real valve is anisotropic, with collagen fibres distributed along the circumferential direction. In chapter 5, we overcome this problem by replacing the present fibre-based elasticity model by a non-linear finite element model using a recent extension of the immersed boundary method Griffith and Luo [2012] that accounts for biological material anisotropy within the context of the hypo-elastic mitral valve constitutive laws.

.

Chapter 5

Finite element patient-specific FSI modelling of the human mitral valve

The patient-specific human mitral valve geometry model is improved by incorporating spatial annulus ring by integrating physical information from in vivo cardiac magnetic resonance imaging data for finite element mesh reconstruction. This mitral valve model is then simulated under a physiological left-atrium-ventricle pressure loading using a finite element version of the immersed boundary method that allows us to discretize the structure via standard finite element methods. Unlike most other extensions of the immersed boundary method to use finite element elasticity Boffi et al. [2008]; Liu et al. [2006]; Zhang and Gay [2007]; Zhang et al. [2004], however, this approach retains a Cartesian grid finite difference discretization of the incompressible Navier-Stokes equation. One advantage of this numerical scheme is that it significantly improves computational efficiency as it

enables us to use Lagrangian meshes that are much coarser than the background Eulerian grid as compared to the traditional approach. A transversely isotropic material constitutive model is used for characterizing the mechanical behaviour of the mitral valve tissue based on recent mechanical tests of healthy human mitral leaflet Wang et al. [2012]. Simulation results exhibit better agreement in flow rate and reduced oscillations when compared to experiment measurements and previous simulation Ma et al. [2012]. The stresses in posterior leaflet are found to be lower than in the anterior leaflet, as the posterior leaflet is smaller and carries less load. In the anterior leaflet, the maximum stresses are observed close to the annulus trigones and free edges of the valve leaflets. These areas are located where the leaflet has the highest curvature. Comparison case eliminating the chordae tendineae in material model is established and valve prolapse occur in such case. We also observe unrealistic high jet flow in diastole without chordae in the model. These studies show that the existence of chordae tendinea plays an important role in regulating the flow through mitral orifice when valve is opening; both chordae and collagen fibres distributed along the circumferential direction help prevent regurgitation and valve prolapse when valve is closing. Our simulation results also shows that the methodology in this study could generate a patient-specific finite element mitral valve model that closely replicates the in vivo mitral valve dynamic motion during middle diastole and systole.

5.1 Introduction

Dysfunction of the mitral valve causes significant mortality and remains a major medical problem worldwide. In order to assess pathologies, an improved un-

derstanding of healthy valve and its tissues is highly demanded. Nowadays, the diagnostics obtained using MRI have matured to a level showing very good details of valve motion and blood flow velocities in vivo. However, such imaging modalities do not yield information on the loads applied to the valve that arise from the coupled fluid and structural dynamics of the valve and the blood Lau et al. [2010]. Therefore, imaging-derived computational models, especially finite element models that account for the observed physiological conditions are an avenue to further quantitative and qualitative insight into valvular function. Such data could be used to develop quantitative methods for determining patient-specific medical and surgical strategies for the treatment of valvular heart diseases.

In chapter 4, we developed a patient-specific three-dimensional fluid structure interaction model of native mitral valve Ma et al. [2012]. In our study, we described dynamic modelling of the human mitral valve that used patient-specific anatomy derived from MR imaging data along with physiological loading conditions. Analysis showed that the patient-specific mitral valve geometry has a significant influence on the simulation results and we validated the computed opening height and flow with clinical measurements. One major limitation of this work is the relatively simple isotropic fibre-aligned model that is used to describe the mitral valve leaflets. The real valve is anisotropic, with collagen fibres distributed along the circumferential direction. To better model this non-linear mechanical behaviour of the mitral valve leaflets, a finite element model of the valve with experimentally characterised strain-energy functions to describe the elasticity of the valve leaflets are highly required.

In this chapter, we use a newly developed finite element version of immersed boundary method described in chapter 2 that combines a Cartesian grid finite

difference method for incompressible fluid dynamics with a nodal finite element method for non-linear elasticity. The mathematical formulation and numerical method require only the specification of a Lagrangian stress tensor to describe the material response of the immersed structure. An improved patient specific mitral valve model is simulated under a physiological left-atrium-ventricle pressure loading with spatial annulus geometry incorporated from in vivo cardiac magnetic resonance imaging data. A hypo-elastic transversely isotropic material constitutive model is used for characterizing the mechanical behaviour of the mitral valve tissue based on a recent mechanical tests of healthy human leaflets Wang et al. [2012]. Simulation results shows that the methodology in this study could generate a patient-specific finite element mitral valve model that could replicate the in vivo mitral valve dynamics during diastole and systole.

5.2 Patient-specific mitral valve model

5.2.1 Mitral valve geometrical model

A cine MR scan was performed on the same healthy 28-year-old male volunteer as described in chapter 4 using a 3-Tesla MRI system (Verio, Siemens, Germany). The study was approved by the ethics committee at the University of Glasgow, and written informed consent was obtained before the scan. Twelve planes including the left ventricular outflow tract (LVOT) were used for mitral valve imaging to cover the entire mitral valve, with typical parameters as follows: slice thickness: 3 mm with 0 mm gap; matrix size: 432×572; pixel size: $0.7 \times 0.7\ mm^2$; frame rate: 25 per cardiac cycle. The mitral valve was reconstructed at the

middle of diastole when the mitral valve is fully opened using an in-house MATLAB (The MathWorks Inc., Natick, MA, United States) graphic user interface implementation, see detailed process in Appendix A.

The general steps for mitral valve reconstruction is similar to the previous work in Chapter 4 except a spatial annulus ring is constructed rather than to use an ellipse projected on the orifice plane Ma et al. [2012] and we assume the valve leaflets have uniform thickness of 1 mm:

- *Leaflet segmentation:* Valvular structures were manually defined on LVOT views in each cut-plane: multiple points defining anterior and posterior profile were selected and connected through cubic splines, assuming a uniform thickness of 1 mm, as shown in Figure 5.1(a);

- *Annulus ring:* In each cut-plane, physical position of the points that connect mitral leaflet and ventricle wall were identified as annulus landmarks, see Figure 5.1(b). Annulus spatial geometry was then reconstructed by joining those landmarks together in SolidWorks, as shown in Figure 5.3(a);

- *Papillary attachment points:* Two papillary attachment points were identified from LVOT and short axis view, as shown in Figure 5.1(b);

- *Vavular substructure assembly:* Three-dimensional coordinates of the points defining anterior, posterior, papillary attachment points were reconstructed and assembled from the position of the image lattice to the real physical position as shown in Figure 5.2;

- *Geometry reconstruction:* The segmented leaflets, papillary attachment points were imported into SolidWorks (Dassault Systèmes SolidWorks Corp.,

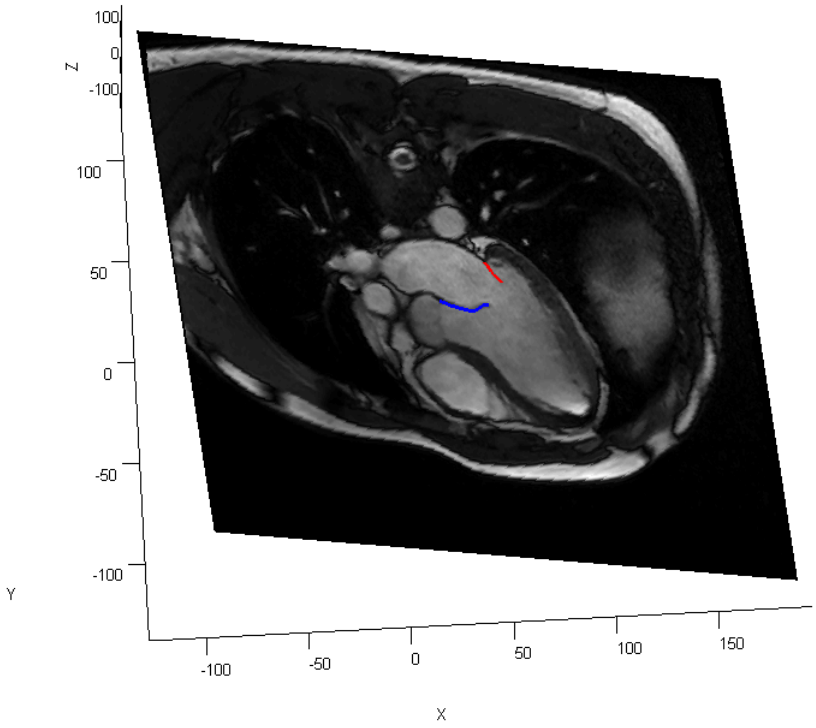

(a)

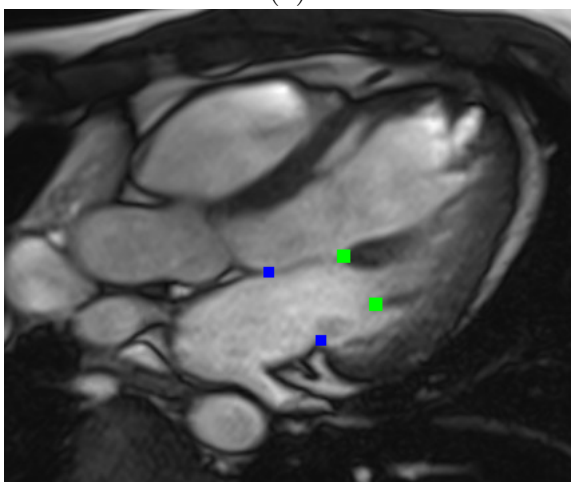

(b)

Figure 5.1: (a) Mitral valve leaflets were manually segmented on left ventricular outflow tract (LVOT) views using two detached lines to represent the anterior and posterior leaflets. (b) Three-dimensional position of two papillary muscle attachment points were identified from LVOT view (*greensquare*); In each LVOT cut-plane, physical position of the points that connect mitral leaflet and ventricle wall were identified as annulus benchmarks, which then imported to SolidWorks to generate spatial annulus ring geometry (*blue square*).

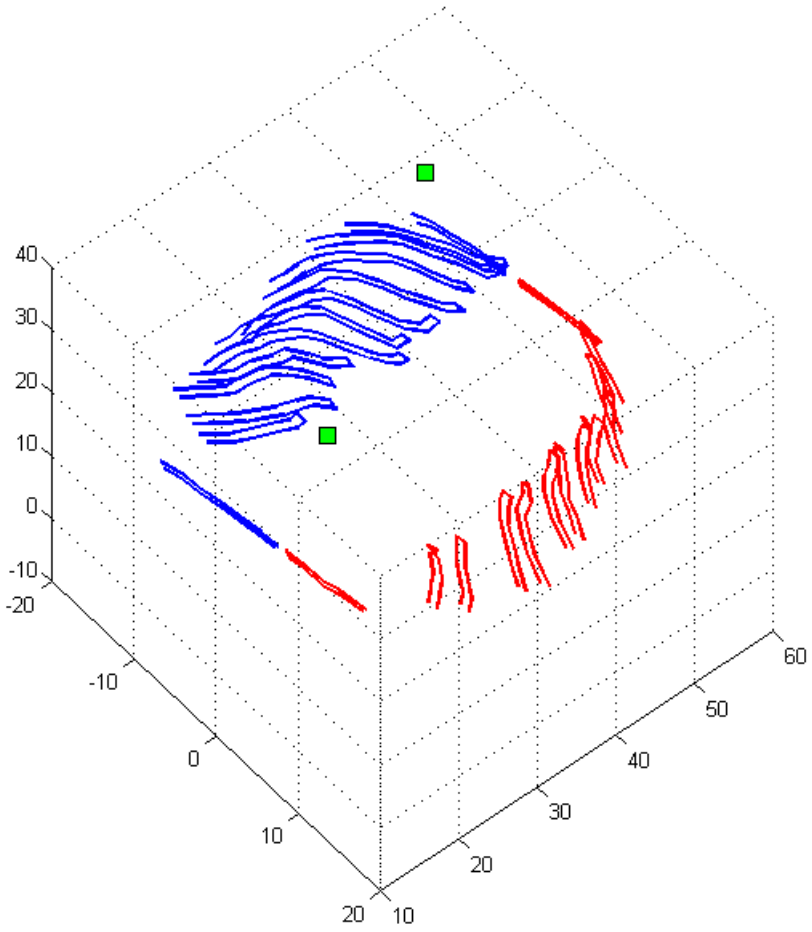

Figure 5.2: Mitral valve geometry reconstructed and assembled using an in-house MATLAB graphic user interface implementation, where anterior leaflet (*blue*), posterior leaflet (*red*) and papillary muscle attachment points (*green square*) were mapped together

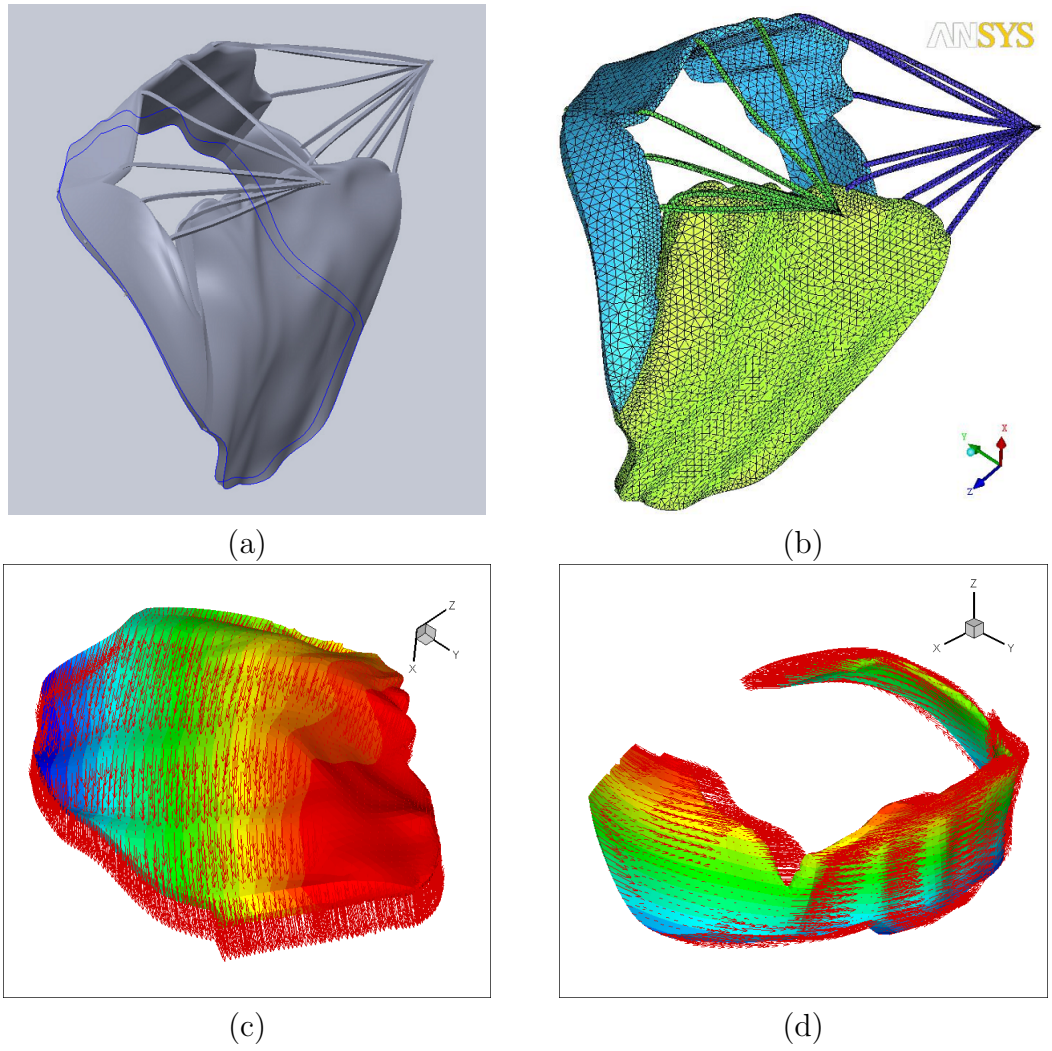

Figure 5.3: (a) The final 3D mitral valve model generated by SolidWorks (Dassault Systèmes SolidWorks Corp., Waltham, MA, USA) with anterior, posterior and chordae; The spatial annulus ring by connecting annulus landmarks using cubic spline is shown in *blue line*; (b) The mitral vale model geometry was then imported into ICEM (ANSYS Inc. PA, USA) for tetrahedral FE mesh generation. The anterior leaflet has 31,708 elements, the posterior leaflet has 18,486 elements, the chordae has 11,164 elements ; (c) The circumferential fibre orientation in anterior; (d) The circumferential fibre orientation in posterior;

Waltham, MA, USA) for geometrical reconstruction using the 'surface loft' method. The final 3D mitral valve model geometry was reconstructed by stitching surfaces together with respect to the anterior and posterior leaflets, see Figure 5.3(a);

- *Chordae tendinae:* A total of 16 evenly distributed marginal chordae were defined based on anatomical descriptions, with 10 associated with the posterior leaflet and 6 with the anterior leaflet, each connected to one of the two papillary attachment points as shown in Figure 5.3(a); Noticed that here we use 16 chordae compared to 22 chordae in chapter 4 as for simplicity. As they all evenly spread into the leaflets, the total contribution of the chordae should remain the same.

- *Mesh generation:* The mitral vale geometry model was then imported into ICEM (ANSYS Inc. PA, USA) for tetrahedral finite element mesh generation. There are 97,931 elements in total: the anterior leaflet has 31,708 elements, the posterior leaflet has 18,486 elements, the chordae has 11,164 elements and the housing disc has 28,253 elements, as shown in Figure 5.3(b);

- *Collagen fibre architecture:* Mitral valve collagen fibres directions oriented in the circumferential direction (parallel along annulus) May-Newman and Yin [1998] were constructed within each element using MATLAB to account for the transversely isotropic material properties of the mitral valve leaflets, as shown in Figure 5.3(c) and Figure 5.3(d). These initial fibre directions will then be put into the main program for calculating Piola-Kirchhoff stress in each time step.

5.2.2 Mitral valve material model

Biaxial testing of anterior leaflet and posterior leaflet May-Newman and Yin [1995, 1998] revealed that both leaflets exhibit large deformations and behave anisotropically, being stiffer along the circumferential direction with the collagen fibres oriented predominantly parallel to the annular muscle shelf. Therefore, we assume that mitral valve tissue is a transversely isotropic material characterized by a strain energy function W derived from Holzapfel [2000] with strain invariants I_1, I_f:

$$W(I_1, I_f) = W_{iso}(I_1) + W_{aniso}(I_f) \tag{5.1}$$

$W_{iso}(I_1)$ is associated with isotropic mechanical response of the non-collagenous matrix of the tissue:

$$W_{iso}(I_1) = C_1(I_1 - 3) \tag{5.2}$$

and $W_{aniso}(I_f)$ associated with anisotropic deformations correspondent to circumferential collagen fibres:

$$W_{aniso}(I_f) = \frac{a_f}{2b_f}\left(exp^{b_f(I_f-1)^2} - 1\right) \tag{5.3}$$

in which $I_1 = \mathrm{tr}(\mathbb{C})$ and $I_f = \mathbf{f}_0 \cdot (\mathbb{C}\mathbf{f}_0)$, in which $\mathbb{C} = \mathbb{F}^\top \cdot \mathbb{F}$ is the right Cauchy-Green tensor, $\mathbf{f}_0$ denoting the unit vector that defines the preferential direction of the fibres in the material in the reference configuration. $\mathbb{F}$ is the deformation gradient tensor, defined as $\mathbb{F} = \frac{\partial \mathbf{X}}{\partial \mathbf{X}}$. Due to the crimp structure of collagen fibres that they do not support compressive stresses which implies that they are inactive in compression. Hence the relevant part of the anisotropic function in Eqs.(5.3) is omitted when $I_f \leq 1$, then the mitral valve responds similarly to a

purely isotropic material described by the energy function in Eqs.(5.2). However, in extension, that is when $I_f > 1$, the collagen fibres are active and energy is stored in the fibre. Specifically, if we eliminate the anisotropic part of strain energy function, this will become Neo-Hookean material. $C_1 > 0$, $a_f > 0$ are the stress-like material parameters, and $b_f > 0$ is dimensionless material parameter. The second Piola-Kirchhoff stress tensor $\mathbb{S}$ is derived as

$$\mathbb{S} = 2\frac{\partial W}{\partial \mathbb{C}} = 2\frac{\partial W}{\partial I_1}\frac{\partial I_1}{\partial \mathbb{C}} + 2\frac{\partial W}{\partial I_f}\frac{\partial I_f}{\partial \mathbb{C}} \tag{5.4}$$

then

$$\mathbb{S} = 2C_1 + 2a_f\left(I_f - 1\right) exp^{b_f(I_f-1)^2}\mathbf{f}_0 \otimes \mathbf{f}_0 \tag{5.5}$$

in which $\mathbb{C} = \mathbb{F}^\top\mathbb{F}$ is the right Cauchy-Green stress tensor. In the finite element version of immersed boundary method, the first Piola-Kirchhoff stress tensor $\mathbb{P} = \mathbb{F}\mathbb{S}$ is used to describe material properties that

$$\mathbb{P} = 2C_1\mathbb{F} + 2a_f\left(I_f - 1\right) exp^{b_f(I_f-1)^2}\mathbb{F}\mathbf{f}_0 \otimes \mathbf{f}_0 \tag{5.6}$$

The material parameters C_1, a_f and b_f were fitted to equal-biaxial in vitro tests on a healthy human mitral valve carried out by Wang et al. [2012] as show in Table 5.1 and Figure 5.4. Notice that in our study, we assume leaflets have only one fibre family along circumferential direction. Therefore, in mitral valve axial direction, the material behaviour is isotropic which yields differences in axial measurements with Wang's equal-biaxial results. In the present model, the fibres are oriented parallel to the annulus (circumferential direction).

Table 5.1: Material parameter values for the strain-energy function

MV	C_1 (dyne/ cm^2)	a_f(dyne/ cm^2)	b_f
Anterior leaflets	$1.7370e^5$	$3.1275e^5$	55.9258
Posterior leaflets	$1.0217e^5$	$5.0011e^5$	63.4814

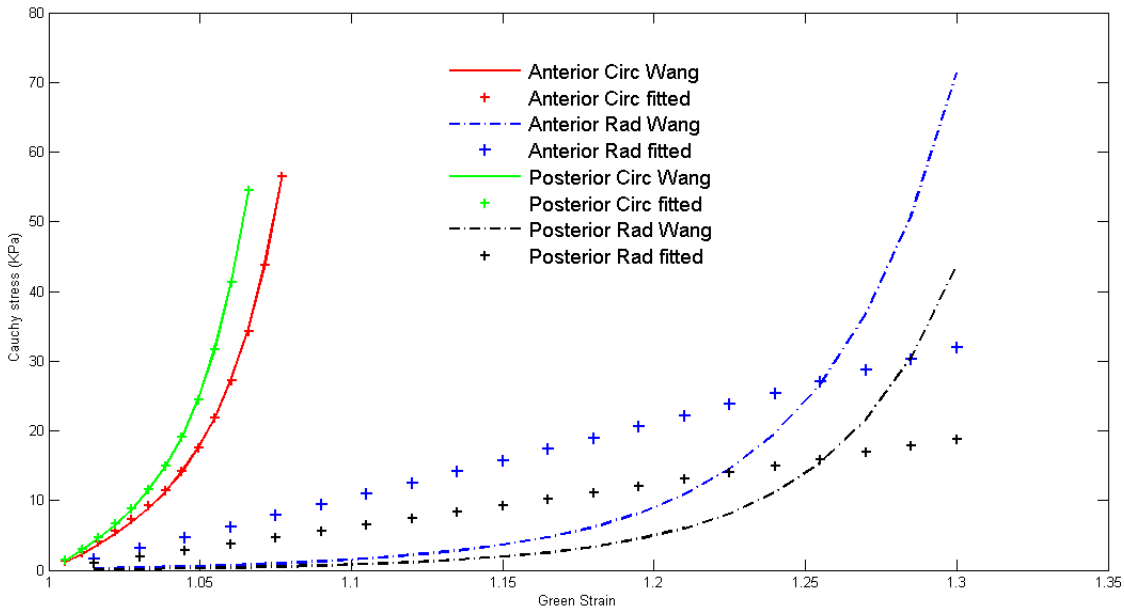

Figure 5.4: Material parameter fitted from Wang's measurements on healthy human mitral leaflets using least square method. Notice that in our study, we assume leaflets have only one fibre family along circumferential direction. Therefore, in mitral valve axial direction, the material behaviour is isotropic.

5.2.3 Chordae tendineae

A total of 16 evenly distributed marginal chordae are defined based on anatomical descriptions, with 10 associated with the posterior leaflet and 6 with the anterior leaflet, each connected to one of the two papillary attachment points. Both the mitral annulus and the papillary tips are fixed in space. The chordae tendineae is assumed to be isotropic and modelled as a Neo-Hookean material:

$$W(I_1) = C\,(I_1 - 3) \tag{5.7}$$

with material parameter C =9 Mpa from measurements of human mitral valve chordae tendinae by Casado et al. [2012] in systole period (from 0.2 s to 0.55 s). However, the chordae are in fact bundles of collagen fibres which should be stiffer in systole when papillary muscle contracts and valve is closing, and softer in diastole when papillary muscle relax and valve is opening. Therefore, we select a smaller chordae tendineae material parameter value that the converged system allows in diastole: C=0.54 MPa. Each of the chordae is assumed to have a uniform cross-sectional area of 1.6 mm^2.

5.2.4 Loading and boundary conditions

In the simulations, the mitral valve annulus is fixed to a housing disc that is mounted in a semi-rigid circular tube immersed in a 16 cm$\times$8 cm$\times$8 cm fluid box, as shown in Figure 5.5. The same transvalvular physiological pressure difference is applied at the inlet and outlet of the tube (see figure.4.5) and zero-pressure boundary conditions are employed along the remainder of the domain boundary. Ma et al. [2012]. We simulate the valve dynamics for a complete cardiac cycle

of 0.7 s, starting from mid-diastole, which is the time when the MR images were used to construct the mitral valve geometry. In our simulation, the total element number is 97931, and the largest stable time step size was set to be $\triangle t = 2.5 \times 10^{-5}$ s. Therefore, computing a complete 0.7 s cardiac cycle requires 2.8 million time steps, which required approximately 5 days on a Dell Unix workstation (24-cores Intel Xeon X5650 2.67 GHz processors).

5.3 Results

5.3.1 Leaflet opening and closing

The fluid pressure and corresponding velocity field generated by the model are shown in Figure 5.6 when the valve is fully open at $t = 0.1$ s and is fully closed at $t = 0.3$ s. The valve opens at a realistically small driving pressure and closes subject to the physiological downstream pressure loading of 150 mmHg.

In the simulation, complete closure of leaflets occurs at a low value of transvalvualar pressure drop: when an approximate of 50 mmHg value was reached, the valve leaflets is closed. Before reaching 150 mmHg of transvalvular pressure drop, the valve undergoes only minor further deformations. The deformed shape of the cross-sectional mitral valve leaflets compared to the corresponding MRI recordings cutting through apex in LVOT view are shown in figure 5.7. The opening and closing configuration of simulated mitral valve shows good agreement with MRI measurements. As observed from both MRI and simulation, the anterior leaflet is convex (with respect to the LV) near the annulus, and is concave close to the free edges in the septilateral direction. Notice that, the gap between the leaflets

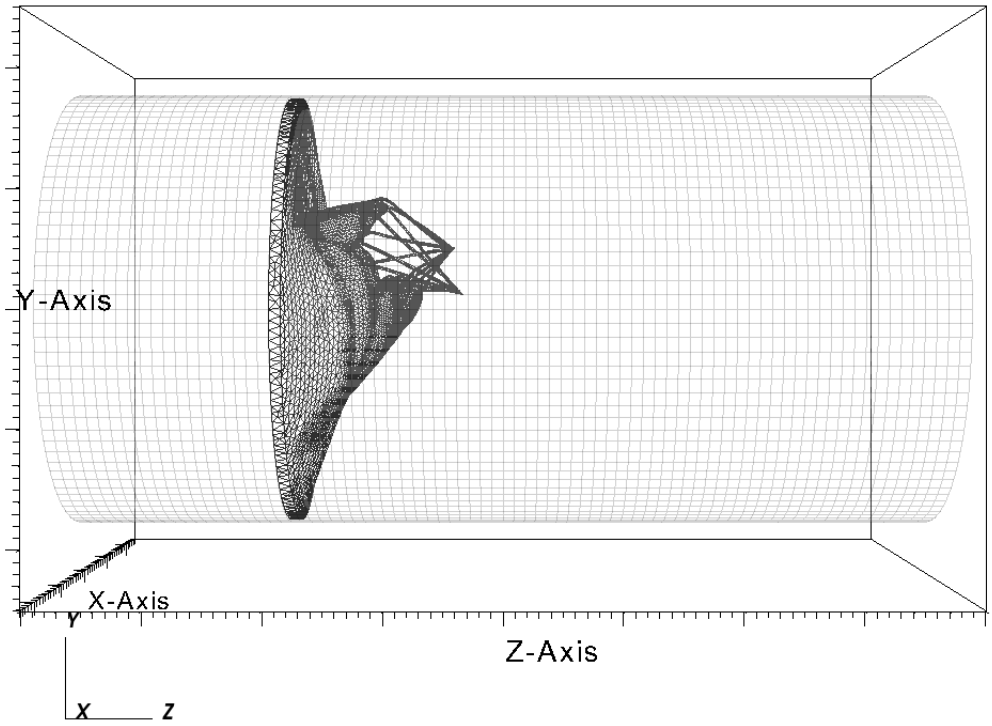

Figure 5.5: The saddle shaped mitral annulus is fixed to a non-planar rigid housing disc which gradually extended to and mounted at the location of $z = -4$ cm in a semi-rigid circular tube of length 16 cm. The valve apparatus, including the valve leaflets and chordae tendinae, are attached to the annulus. The chordae are anchored to two fixed papillary attachment points which are located downstream of the valve. These structures are all immersed in a 16 cm $\times$ 8 cm $\times$ 8 cm rectangular fluid box.

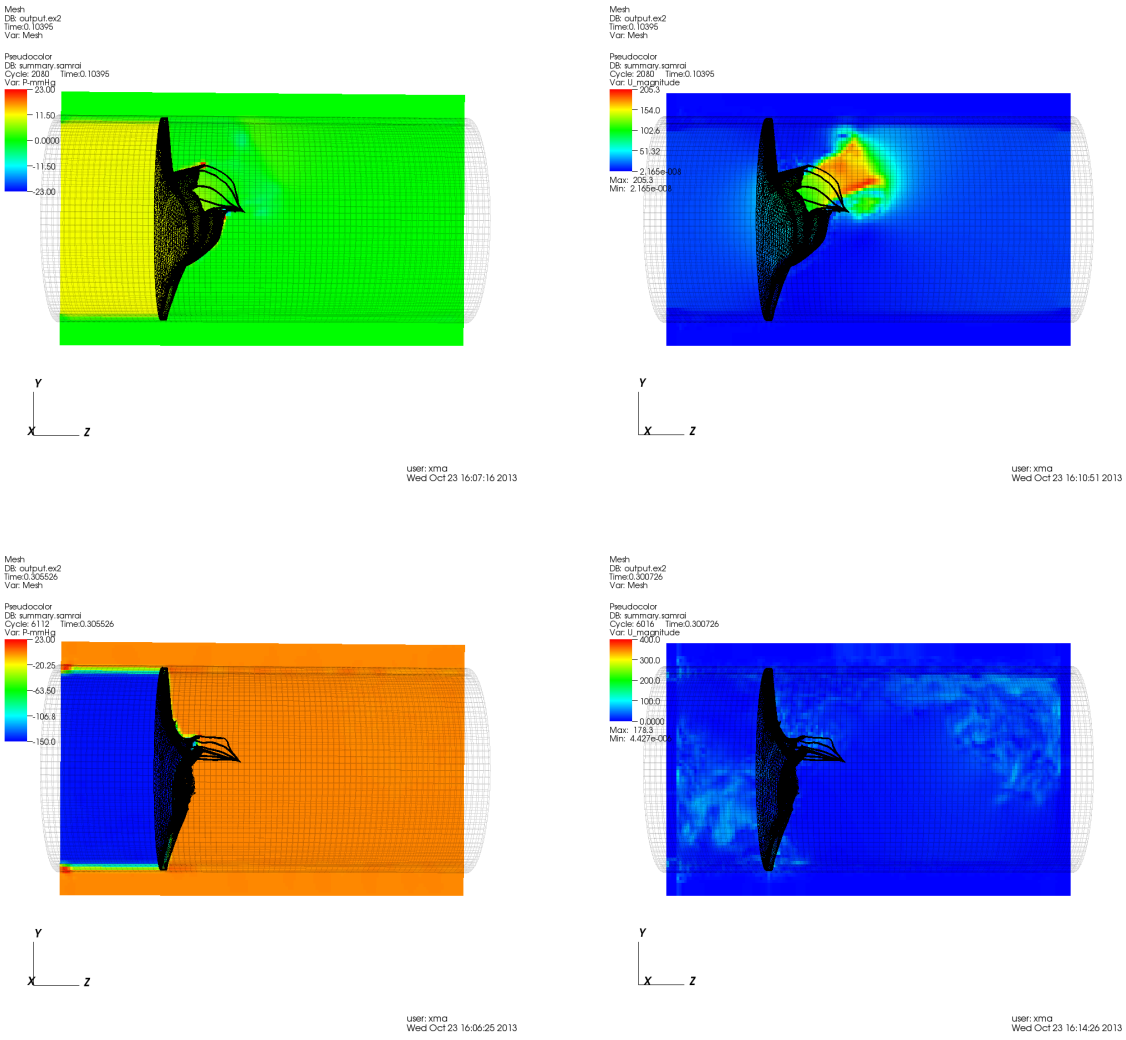

(a) (b)

Figure 5.6: (a) The fluid pressure field along the plane orthogonal to z axis, shown at $t = 0.1$ s when the mitral valve is fully open (top), plotted from -23 mmHg to 23 mmHg, and $t = 0.3$ s when the valve is fully closed (bottom), plotted from -150 mmHg to 23 mmHg. (b) The corresponding fluid velocity field bisecting the mitral valve, top panel: plotted from 0 to 205 cm/ s, and bottom panel: plotted from 0 to 400 cm/ s.

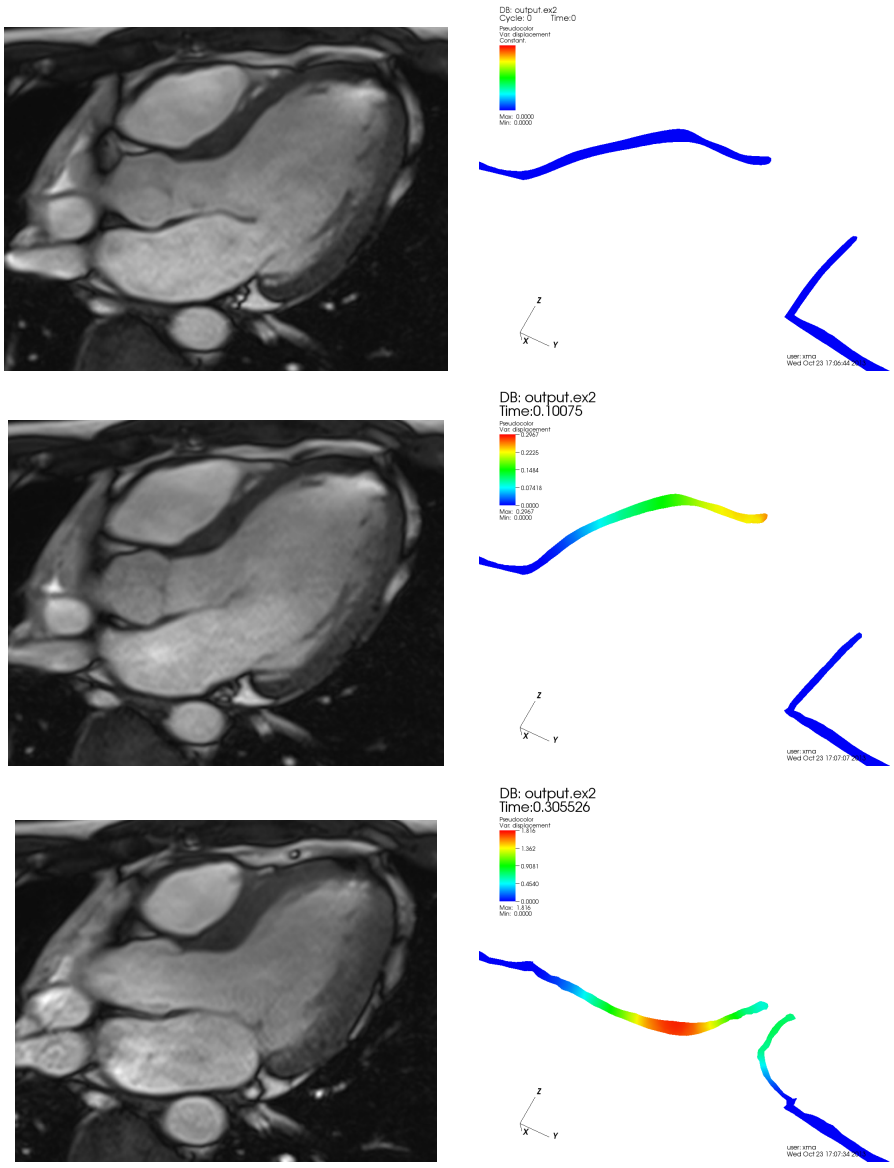

(a) (b)

Figure 5.7: (a) The MRI recordings in LVOT long axis view which bisecting the central line of mitral valve through apex showing the opening and closing sequences in diastole and systole; (b) The different stages of cross-sectional mitral valve in a whole cycle from a plane bisecting the middle-line of anterior and posterior leaflet; the leaflets were coloured according to the total displacements, the top row shows the initial configuration of the valve at $t = 0$ s; the middle and the bottom row shows the opening and closing configuration of the leaflet at $t = 0.1$ s when valve is fully open and at $t = 0.3$ s when valve is fully closed.

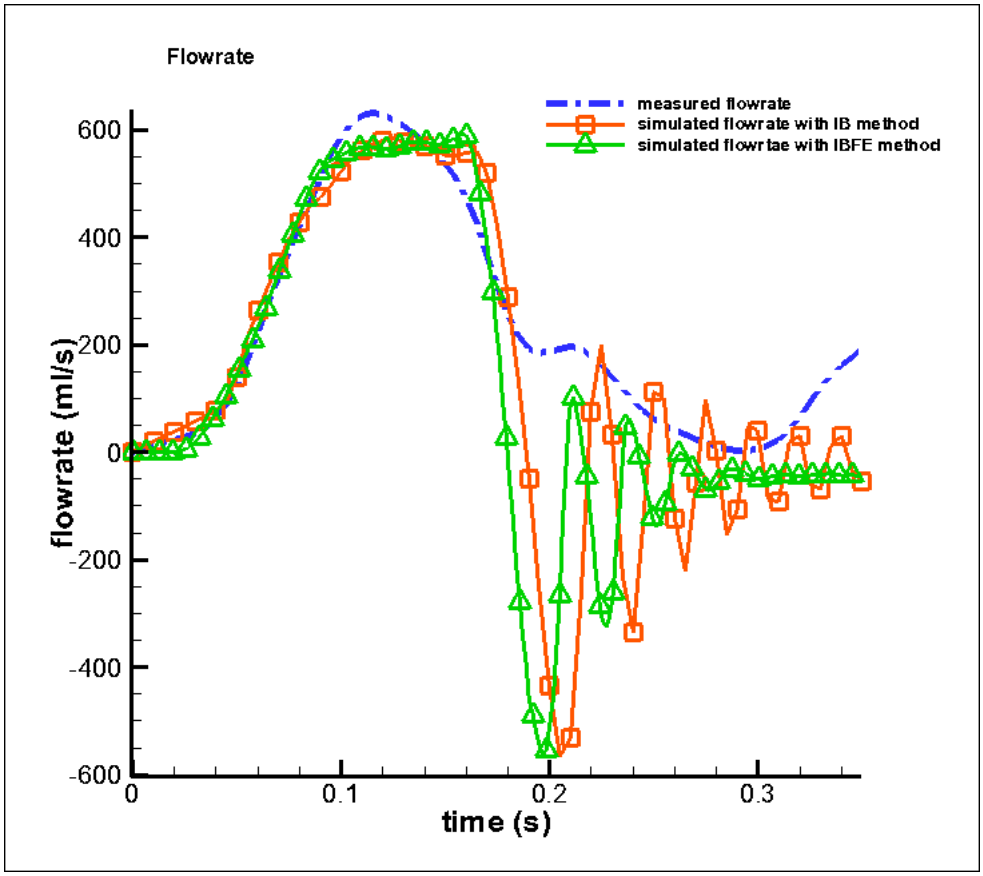

Figure 5.8: Flow rates produced by the mitral valve models with immersed boundary method (*Orange* line with square) which is calculated and figured in 4.10 and with finite element version of immersed boundary method (*Green* line with triangle)along with measured flow data (*Blue* Dashdot)obtained from phase contrast cine MRI. Both results from immersed boundary method and from finite element version of immersed boundary method have good agreement to the experimental measurement at the peak valve of the flow, but the oscillation time and range was reduced when using finite element immersed boundary method.

in the models is due to the numerical limitation related to immersed boundary method.

The flow rate through the valve orifice is shown in Figure 5.8. A comparison to the flow rate obtained from previous work Ma et al. [2012] has shown that by adding experiment-based collagen-fibre-reinforced material properties into the leaflet the oscillation time and magnitude of the flow are largely reduced when valve is closed. It again demonstrates that this fluid-structure interaction simulation of the mitral valve models under physiological pressure loading can provide close prediction to the in vivo mitral valve dynamics. We remark that the second peak in the measured flow rate is due to contraction of the left atrium. This additional ventricular loading is not considered in our simulation.

5.3.2 Leaflet stress and strain

The collagen fibre orientation and the maximum principal strain and stress orientation (view from left ventricle) are plotted in Figure 5.9 at a systole pressure of 150 mmHg. In the anterior and posterior leaflets, the fibre direction and the maximum principal stress and strain direction are nearly aligned. This shows that the maximum principal stress and strain are carried by the collagen fibres in the mitral leaflets.

The maximum principle stress and strain distribution of the mitral valve leaflets at a systole pressure of 150 mmHg is shown in Figure 5.10. Stress in the mitral leaflets shows an asymmetric and anisotropic distribution. The stress in the anterior was found to be higher than that in the posterior leaflet. Highest stress occur at the region close to the fibrous trigones along annulus and close to the tip

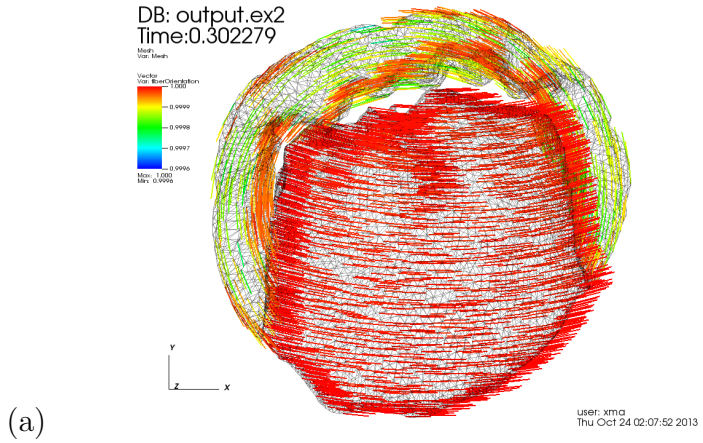

(a)

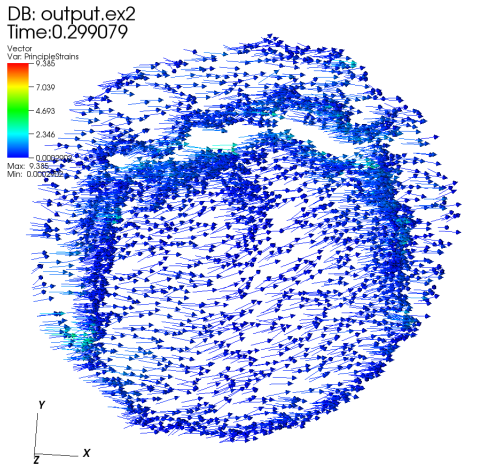

(b)

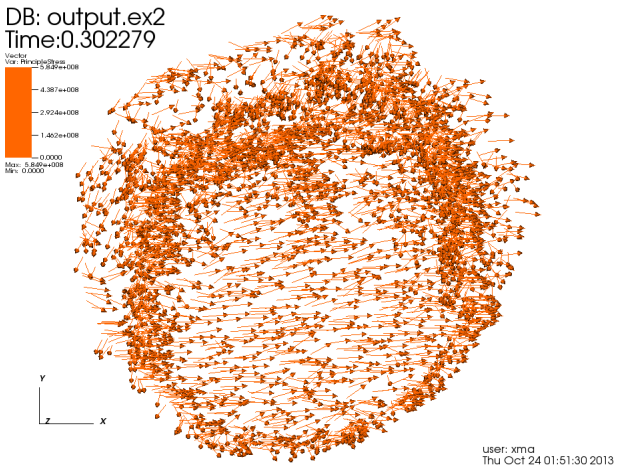

(c)

Figure 5.9: (a) The collagen fibre orientation plotted at a systole pressure of 150 mmHg; (b) the maximum principle strain orientation in the leaflets plotted at a systole pressure of 150 mmHg; (c) the maximum principle stress orientation in the leaflets plotted at a systole pressure of 150 mmHg

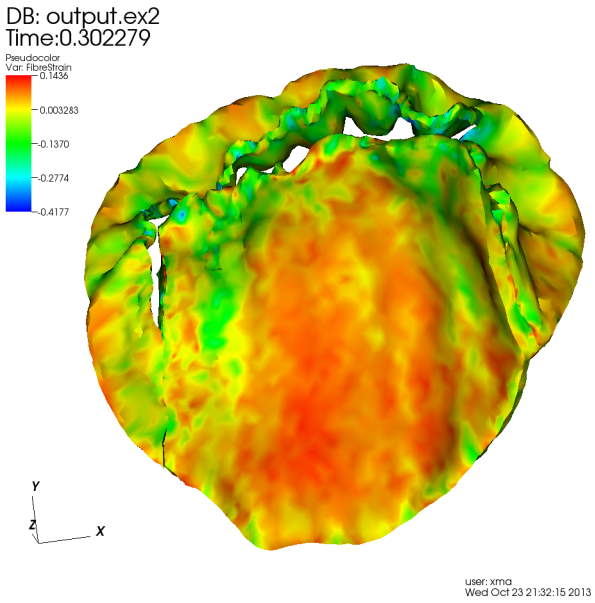

(a)

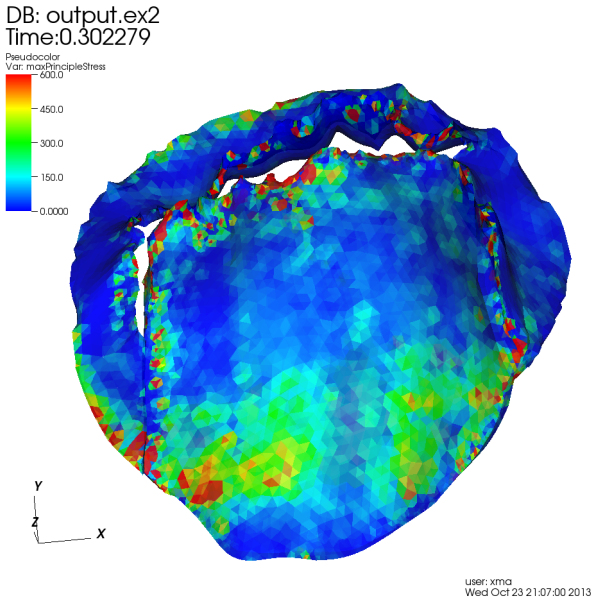

(b)

Figure 5.10: (a) The distribution of maximum principle strains (atrial view) at a systole pressure of 150 mmHg; (b) The distribution of maximum principle stress (atrial view) at a systole pressure of 150 mmHg;

of mitral valve free edge and commissure edge. The maximum principal strain of the mitral leaflets was 0.1463 in the circumferential directions and the maximum principal stress of the mitral leaflets was 58.6 MPa.

5.3.3 Effect of chordae tendineae

A chordal effect analysis is conducted to compare the mitral valve systolic deformations with two cases: one with chordae tendineae in the model, and one without. Unrealistic high speed jet flow through the mitral valve orifice when opening is observed in the latter case in Figure 5.11(b). The anterior leaflets bulge into the left atrium at a systolic pressure of 57 mmHg, shown in Figure 5.11(b) when chordae tendineae is excluded in the model. This demonstrates that the chordae tendineae plays an important role in valve opening during diastole and in valve closing during systole. Without a proper construction of chordae tendineae may lead to incomplete closure and prolapse of the mitral valve during systole and high blood velocity through orifice in diastole.

5.3.4 Shape of annulus ring

A comparison of the valve closure configuration (colored by deformation) between the mitral valve model with elliptical annulus orifice, which is used in simulations in chapter 4, and the improved mitral valve model with saddle shaped annulus orifice is shown in Figure 5.12(a) and 5.12(b). It is obvious that with spatial annulus the mitral valve leaflets close better when compared to model with elliptical annulus. Unrealistic jet flow through the leaflet orifice during valve opening and big oscillations with slight back flow is also observed in the case with elliptical

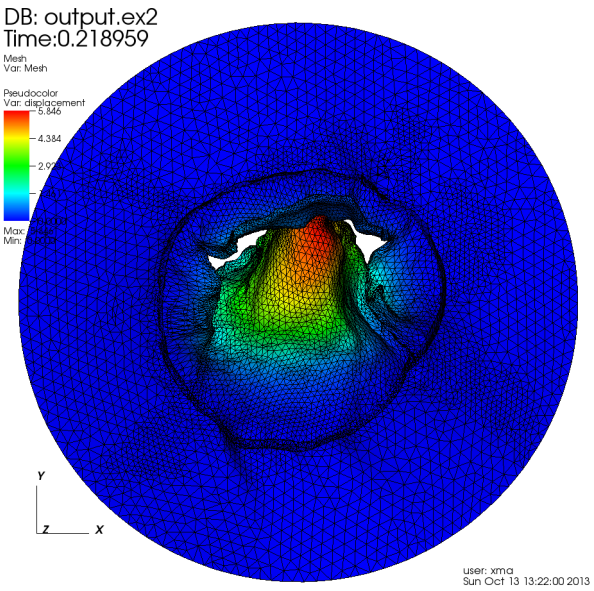

(a)

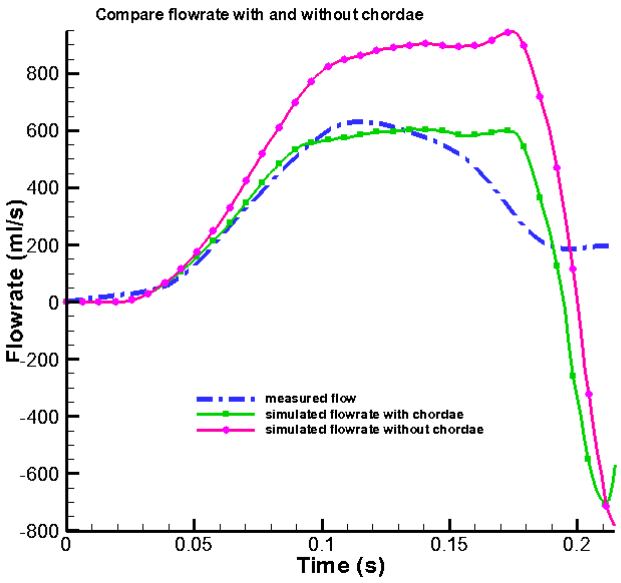

(b)

Figure 5.11: (a) Mitral valve leaflets prolapse at a systolic pressure of 57 mmHg when chordae was not included in the model; (b) Flow rates comparison produced by the mitral valve models with (*Green* line with square)and without chordae (*Pink* line with circle) along with measured flow data (*Blue* Dashdot)obtained from phase contrast cine MRI.

annulus as shown in Figure 5.12. These all illustrate that realistic spatial annulus shape will help valve closure and maintain proper flow pattern during systole, which prove the importance of capturing the nature geometry of mitral valve in dynamic simulation.

5.4 Conclusions and future work

In this paper,we use a finite element version of immersed boundary method that combines a Cartesian grid finite difference method for incompressible fluid dynamics with a nodal finite element method for non-linear elasticity. In conventional immersed boundary method (Griffith et al. [2009]; Luo et al. [2012]; Ma et al. [2012]), regularized delta functions are used by the immersed boundary method both to spread forces generated by the structure directly from the nodes of the Lagrangian mesh to the Eulerian grid and also to interpolate velocities from the Eulerian grid directly to the nodes of the Lagrangian mesh. A significant limitation of this approach is that if the physical spacing of the Lagrangian nodes is too large in comparison to the background Eulerian grid, severe "leaks" will develop at fluid-structure interfaces. An empirical rule that generally prevents such leaks is to require the Lagragian mesh to be approximately twice as fine as the Eulerian grid Peskin [2002]. As high Eulerian resolution is needed to capture the thin boundary layers characteristic of flows, therefore, following the empirical rule will result in dense Lagrangian meshes that may generate significant numerical stiffness in the discretized equations and excessively small timesteps. Moreover, when an initially "watertight" structure exhibit large deformations, the structure mesh may ultimately yields leaks as the simulation progresses.

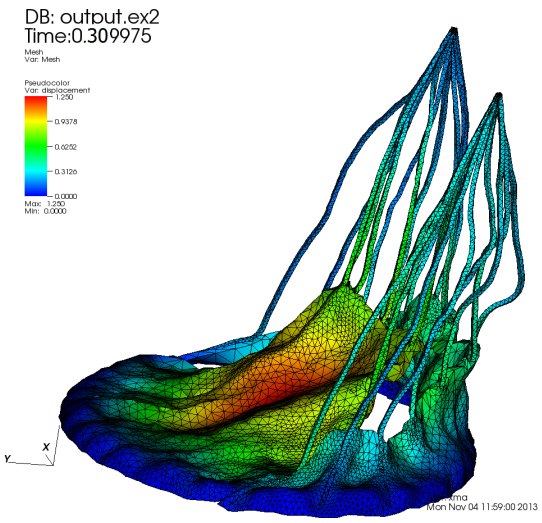

(a)

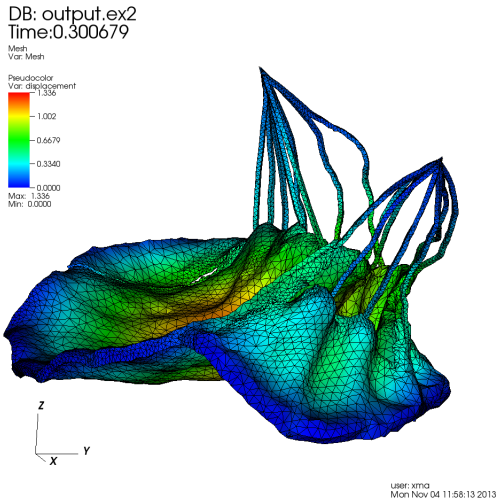

(b)

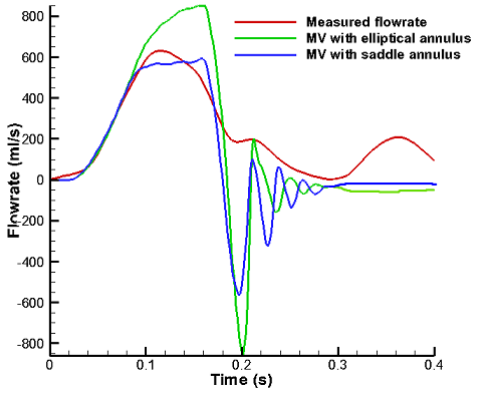

(c)

Figure 5.12: (a) Mitral valve model with elliptical annulus at time=0.3 s; this model is used in simulations in chapter 4 as shown in Figure 4.3; (b) Improved mitral valve model with saddle shaped annulus at time=0.3 s (c) Flow rates comparison produced by the mitral valve model with elliptical annulus and with saddle annulus along with measured flow data from phase contrast cine MRI

One advantage of using the finite element version of immersed boundary method is to discretize the equations of Lagrangian-Eulerian interaction that overcomes this long existing limitation. Specifically, rather that spreading forces from and interpolating velocities to the nodes of the Lagrangian mesh, we instead spread forces from and interpolating velocities to quadrature points within the interiors of the Lagrangian finite element mesh. This takes advantage of the additional geometrical information provide by the finite element description of the structure which provides information not only on the nodes of the Lagrangian mesh, but also on the material points within the mesh. Therefore, any mesh that have a quadrature scheme with sufficiently many quadrature points can prevent leaks effectively. Numerical examples from Griffith and Luo [2012] demonstrate that this approach permits the use of Lagrangian meshes that are at least four times as coarse as the background Eulerian grid without leaks, which enables the analysis tailored to requirements of the structure rather than restricted by the background Eulerian mesh. In our simulations, we have twice dense finite element meshes as compared to the previous work in chapter 4 that used conventional immersed boundary method, but the largest stable time step is twice as large as the previous one that allowing for shorter computation time in total. These show that by adopting finite element spatial discretization the computational efficiency is significantly improved.

In this study, a hypo-elastic transversely isotropic material model is incorporated to account for the different constituents and fibre direction in the mitral valve. An initial validation of the model is provided by comparing the computed opening and closing configuration and flow rates to clinical measurements from the volunteer who provided the anatomical data used to construct the model. Compared

to our previous study Ma et al. [2012], much smaller oscillations and convergence time are seen in the computed flow rate at the flow decelerating phase. This shows that the circumferential stiffening by adding collagen fibre into the mitral valve leaflets can help valve closure. The maximum principal strain and stress orientation plotted in Figure 5.9 at a systole pressure of 150 mmHg closely align to the fibre orientation, which shows that the maximum principal stress and strain under the peak systole pressure are carried by the collagen fibres in the mitral leaflets. The stress distribution in posterior leaflet are found to be lower than in the anterior leaflet. This is because the posterior leaflet is smaller and carry less load. The maximum stress in anterior are observed close to the fibrous trigones along the annulus and free edges of the leaflets as these areas are located where the surfaces has the highest curvature. The deformation of leaflet edges is unstable corresponding to strong correlation with the fluid and thus have higher stress concentration.

An chordal effect analysis is conducted to compare the mitral valve systolic deformations with two cases: one with chordae tendineae in the model, and one without. Unrealistic hight speed jet flow through the mitral valve orifice when opening and valve prolapse is observed in the latter case. This demonstrates that the chordae tendineae also plays an important role in valve opening during diastole and in valve closing during systole. Without a proper construction of chordae tendineae may lead to incomplete closure and prolapse of the mitral valve during systole and high blood velocity through orifice in diastole. A comparison of the deformation and flow rates between the mitral valve model also shows that patient-specific saddle annulus will help in valve closure and maintain proper flow through the orifice. It might because the native geometry of human

body always tends to preserve the minimum loss of efficiency and functions in optimal, which proves the importance in obtaining patient-specific modelling in mitral valve analysis.

However, there are several limitations in our model: First, chordae are actually bundles of collagen fibres with highly fibre reinforcement along the collagen direction in systole. In our model, we assume chordae as an isotropic Neo-Hookean material having stiffer material properties in systole and softer material properties in diastole. This need to be improved by adding fibre direction and anisotropicity to chordae tendinae in our future work. Second, in our study, the patient-specific mitral valve geometries at middle diastole were obtained from MRI scan of a 28 year old male volunteer. However, the material model used for the mitral valve leaflets was based on biaxial tests on a 61 year old male Wang et al. [2012]. As the stiffness of soft biological tissue increases with age, this may explain the excessively large principal stress and strain in the leaflet when we use the rescaled pressure data that matches with the volunteer in the MRI images. Ideally, material properties of the same patient should be determined inversely from cardiac images Liu et al. [2009b], but this method may be difficult in obtaining enough spatial resolutions for strain measurement on such small structure as mitral valve. In present, the model data should be tuned inversely somehow to match the pressure state of the patient in the images. Third, although more realistic pressure boundary conditions are implemented in the present simulations, these boundary conditions do not include any feedback mechanisms that are able to adjust the flow and pressure resulting from compliances of left ventricle and left atrium. We believe that the lack of realistic compliance in the loading conditions is the principal reason for the oscillations seen after $t = 0.5$ s in our simulations. Future

work on incorporating heart ventricle is clearly required. As we simulate valve dynamic in a tube rather than in left ventricle, the annular ring in our model was assumed to be fixed in space, whereas in case of a native valve, it is deformable and moving upward and downward in diastole and systole. The study of the movement of annulus ring should also be included in as we incorporate left ventricle in our model. One also need to be pointed out is the discontinuities in stress map. We have refined the structure mesh by twice but such discontinuities still occur, which shows that the discontinuity might be introduced by the fluid grid. However, in our model the Cartesian fluid mesh can't be refined further at the moment due to numerical instabilities and computational efficiency. This also need to be improved in future.

Chapter 6

Conclusions and future work

From chapter 3 to chapter 5 we focus on constructing mitral valve fluid-structure interaction models with immersed boundary method, in which the blood is described as a viscous incompressible fluid, and the mitral valve and its substructures are described as elastic or hypo-elastic solid structures.

In chapter 3, we first model the dynamics of a prosthetic mitral valve using a staggered-grid version Griffith [2012a,b]; Griffith et al. [2009] of a formally second-order accurate immersed boundary method Griffith [2005]; Lai and Peskin [2000] under a realistic pressure loading during a cardiac cycle. In this work, we demonstrate that when bending rigidity are both included in the mitral leaflets and chordae, the computational flow rate has better agreements with experimental measurements with less oscillations during valve closure. These findings highlight the importance of accounting for the bending stiffness in the dynamic simulation of the mitral valve prosthesis.

As the final goal of the research in mitral valve prosthesis is to provide better treatment for patients, we then carry out the patient-specific mitral valve dynamical modelling under physiological left-atrium-ventricle pressure loading in chapter 4. A Matlab based GUI interface package is developed to capture the

physical information of human mitral valve and to construct mitral valve geometry model from magnetic resonance imaging (MRI) data. An initial validation of the model is provided by comparing the computed opening shape and flow rates to clinical measurements from phase contrast MRI of the volunteer. The convex (with respect to the left ventricle) shape near annulus and concave shape near free edge of valve are observed in our simulation during diastole and systole when assigning physiological thickness McDonald et al. [2002] to the anterior leaflet and posterior leaflet, which match perfectly with clinical observations Karlsson et al. [1998]; Kvitting et al. [2010]; Ryan et al. [2008]. These results suggest that differences in the thickness of the leaflets play an important role in maintaining the physiological curvature of the mitral valve Ma et al. [2012], which bring out a question that is the relatively simple isotropic material fibre model sufficient to describe the mitral valve leaflets as the real valve is anisotropic, with collagen fibres distributed along the circumferential direction.

To better model this non-linear mechanical behaviour of the mitral valve leaflets, we then simulate the mitral valve model under a physiological pressure loading with a finite element version of the immersed boundary method that is able to incorporate experimentally oriented constitutive laws for elasticity models Griffith and Luo [2012] in chapter 5. In this chapter we also improve the patient-specific mitral valve model by incorporating realistic saddle shaped annulus ring rather than ellipitical annulus orifice. A hypo-elastic transversely isotropic material constitutive law is constructed for characterizing the mechanical behaviour of the mitral valve tissue based on recent biaxial tests on healthy human leaflets by Wang et al. [2012]. Simulation results exhibit better agreement and more reduced oscillations in flow rate with phase contrast MRI measurements compared

to previous simulations Ma et al. [2012] and show that the maximum principal stress and strain is carried by the collagen fibres in the mitral leaflets in deep systole. Effect of chordae and shape of annulus are also discussed in chapter 5, emphasizing the importance of patient-specific geometry for dynamic modelling. These results show that the methodology in this study could generate a patient-specific finite element mitral valve model with transversely isotropic material constitutive model that closely replicate the in vivo mitral valve dynamic motion during diastole and systole, which might bring insight of the treatment of the patient valvular heart diseases.

As far as I know, this is the first patient-specific fluid-structure interaction mitral valve model that be able to capture and replicate the in vivo mitral valve dynamics during a cardiac cycle. However, to make the mitral valve modelling be more accurate and clinical useful, there are still a lot of future work need to be done: First, there still exists some degree of discrepancy between the computed and the measured flow rate, particularly at the flow decelerating phase - much greater oscillations are seen in the computed flow rate compared to the measured one. We comment that this is primarily due to the lack of realistic compliance in the loading condition when we research on the dynamic motions of mitral valve in a tube. By incorporating heart ventricle such oscillations might be greatly reduced. This can also solve another problem that when we simulate valve dynamic in a tube rather than in left ventricle, the annular ring in our model was assumed to be fixed in space, whereas in case of a native valve, it is deformable and moving upward and downward in diastole and systole. The study of the movement of annulus ring should also be included in as we incorporate left ventricle in our model. Second, in our study, we prove the importance of incorporating the anisotropic

material properties in our mitral valve model. However, the material model used for the mitral valve leaflets was based on biaxial tests on a 61 year old male Wang et al. [2012] whereas the patient-specific mitral valve geometries at middle diastole were obtained from MRI scan of a 28 year old male volunteer. As the stiffness of soft biological tissue increases with age, this may explain the excessively large principal stress and strain in the leaflet when we use the rescaled pressure data that matches with the volunteer in the MRI images. Ideally in future, material properties of the same patient should be determined inversely from cardiac images Liu et al. [2009b]. This method may be restricted in obtaining enough spatial resolutions for strain measurement on such small structure as mitral valve, but following the rapid development of clinical imaging methodologies such future is not that far. Third, as we initial this research for better treatment of the patient heart valve disease, we also need to establish analysis not only on healthy people but patients who suffer from valvular diseases. In fact, the framework of mitral valve dynanic modelling we established in this thesis can also be applied to patient study. Furthermore, the numerical scheme should still be improved for reduced computational time. As from clinical point of view, quick diagnose and high computational efficiency is always of great importance.

Appendix A:

A MATLAB based GUI for patient-specific MV modelling

A.1 Design considerations

The present work consists of a graphic user interface (GUI) implementation based on MATLAB able to integrate physical information from in vivo real time cardiac magnetic resonance imaging data for patient-specific mitral valve (MV) finite element mesh construction. The mitral valve FE meshes were then used in chapter 4 and chapter 5 to simulate the mitral valve dynamics in a whole cardiac cycle using immersed boundary method. This patient-specific mitral valve model captured the real anterior and posterior leaflet geometry that was observed clinically to be convex (with respect to the LV) near the annulus, and concave close to the free edges in the septilateral direction Karlsson et al. [1998]; Kvitting et al. [2010]; Ryan et al. [2008] and saddle shape spatial annulus geometry. Specifically, we also obtained the positions of papillary muscle attachment points from high resolution MRI.

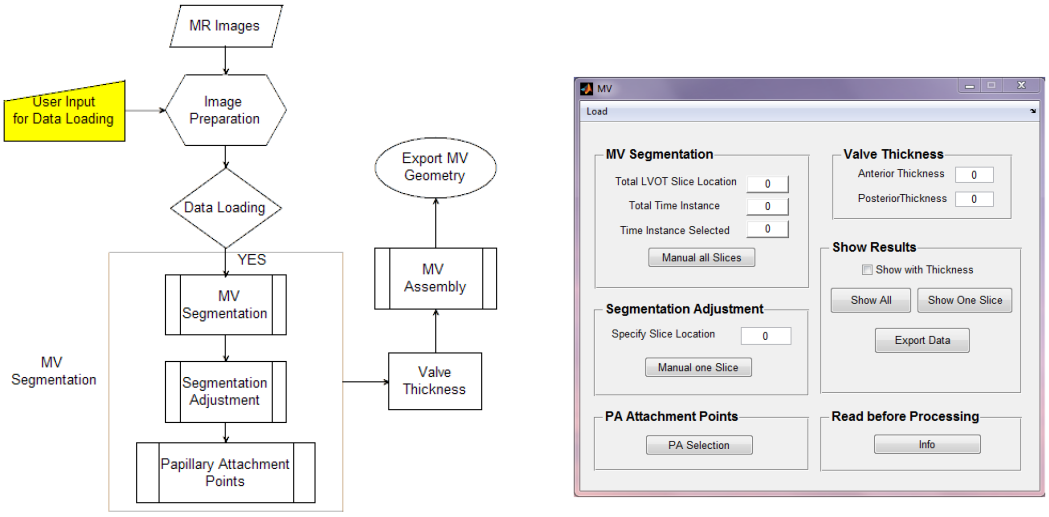

Figure A.1.1: (Left) The design diagram of the GUI interface for patient-specific MV modelling: Image preparation, MV segmentation and MV assembly are the three main blocks in the code (Right) The GUI interface for patient-specific MV modelling which can capture the geometry of anterior, posterior leaflets, the spatial annulus and the papillary attachment points

The main process of the GUI interface consists of three main blocks, shown in Figure.A.1.1: Image preparation, MV segmentation and MV assembly.

A.2 Image preparation

A cine MR scan was performed on a healthy 28-year-old male volunteer using a 3-Tesla MRI system (Verio, Siemens, Germany). Twelve planes including the left ventricular outflow tract (LVOT) were used for MV reconstruction to cover the entire mitral valve, as shown in Figure A.2.1, indicated by the green lines superimposed on the two-chamber view. The parameters for the MV MRI scan were: slice thickness: 3 mm with 0 mm gap; matrix size: 432×572; pixel size: 0.7×0.7 mm^2; frame rate: 25 per second. The MV was reconstructed at the

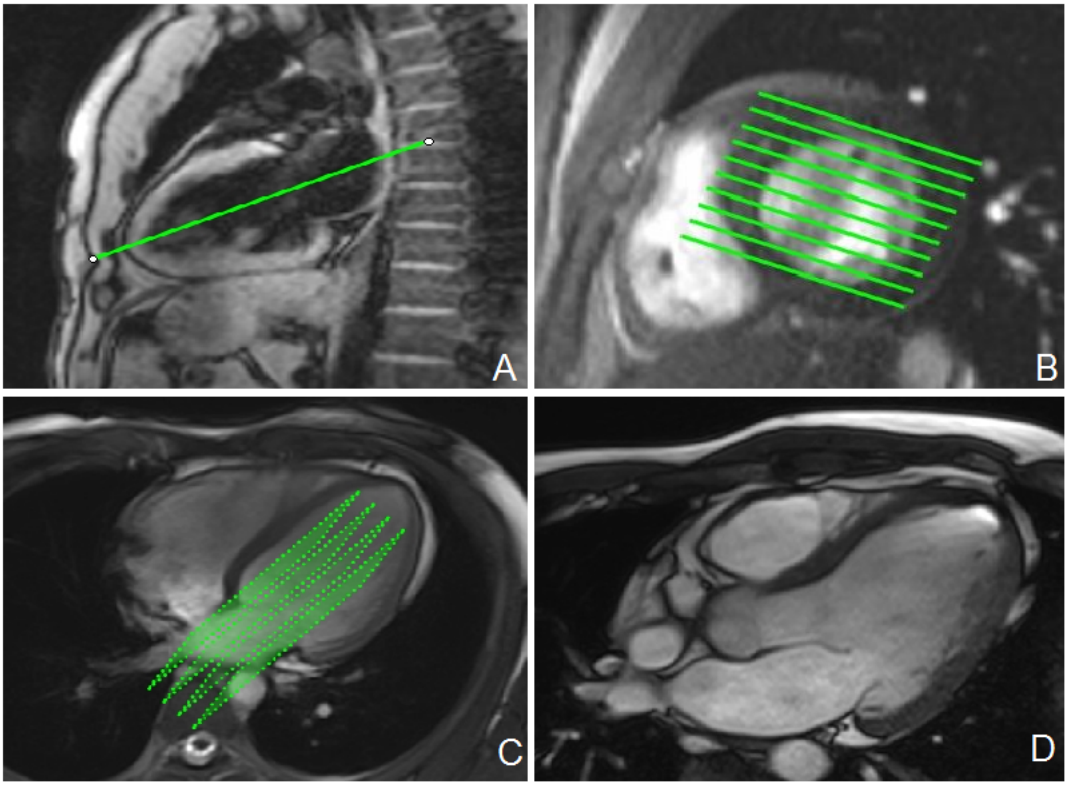

Figure A.2.1: Magnetic resonance images of the mitral valve. (a) Illustration of the image coordinate defining the valve position; (b) Illustration of the image plane positioned to cover the whole valve (top view from left atrium along long axis); (b)Illustration of the image plane positioned to cover the whole valve (4 chamber view);(d) Left ventricle outflow tract of the mitral valve MR image showing the anterior and posterior leaflets

middle of diastole when the MV was fully opened.

During the Data preparation, the image data information are set and loaded by setting the directory path containing patient MR image files, providing the image sequence number that we can identify the mitral valve position, identifying the series time that we select to construct mitral valve geometry, and providing information of the short axis image for identifying papillary muscle attachment points.

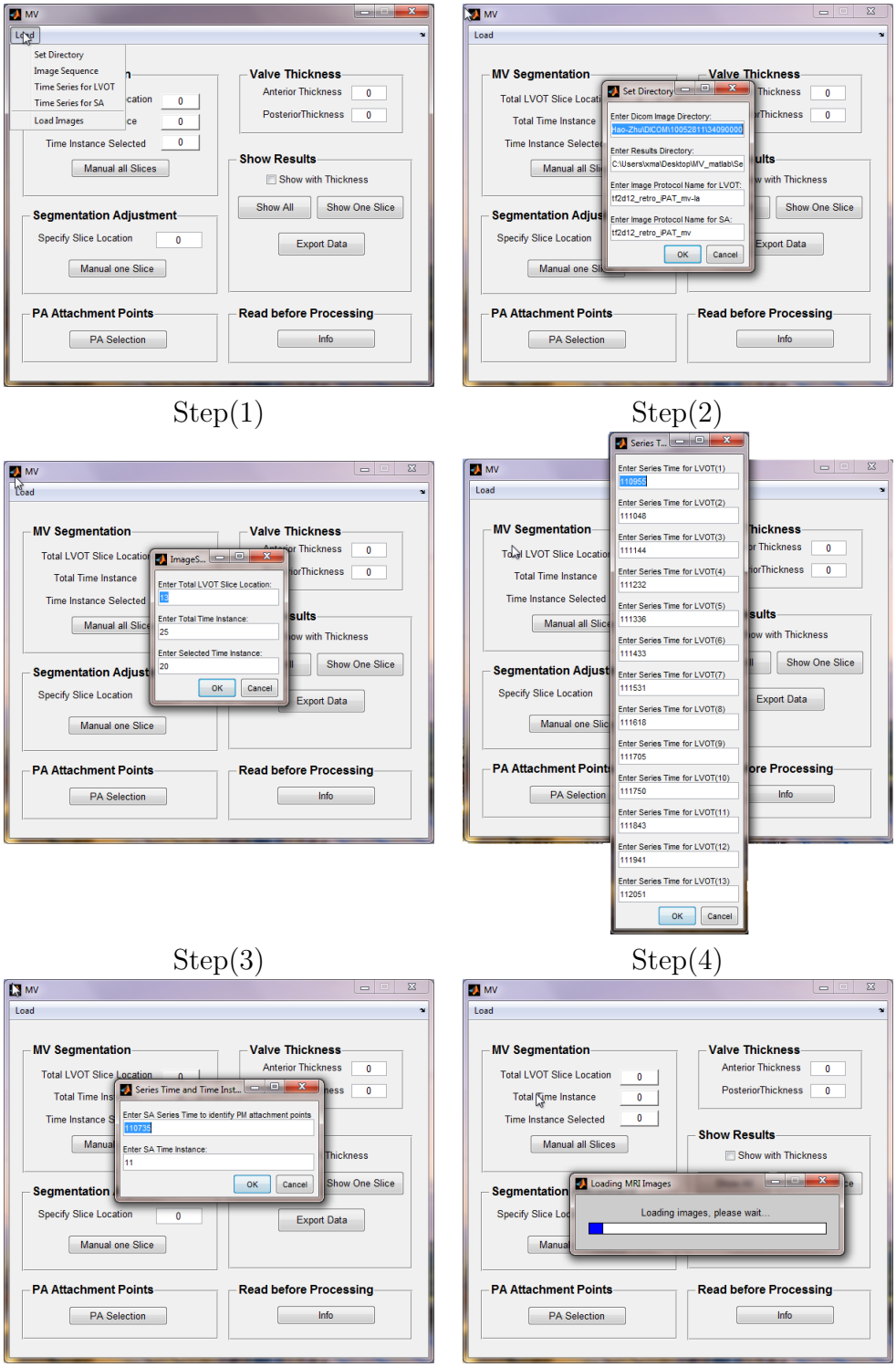

Figure A.2.2: Data preparation–set the directory path containing MR image files of patient, provide the image information that we can identify the mitral valve position, set the series time that we select to construct mitral valve geometry, and provide information of the image for identifying papillary muscle attachment points

- *Load:* Left click "Load" at the up-left corner of the GUI surface to start the data preparation, see Figure.A.2.2 Step(1);

- *Set Directory:* Select "Set Directory" for setting the path and providing MRI image information: "Enter Dicom Image Directory" for MR images used for mitral valve geometry construction; "Enter Results Directory" for directory that restore the final geometry files; "Enter Image Protocol Name for LVOT" for dicom protocol name for Left ventricle outflow track view showing leaflets detail; "Enter Image Protocol Name for SA" for dicom protocol name for short axis view showing papillary muscle attachment points postion; see Figure.A.2.2 Step(2);

- *Image Sequence:* Select "Image Sequence" for setting image data information: "Enter Total LVOT slice Location" to set the total LVOT slice number that cover the whole mitral valve, in our case it's 13 slices; "Enter Total Time Instance" for the image frame number that cover the whole heart cycle in one MRI scan, in our case it's 25 frames; "Enter Selected Time Instance" for the time when we construct mitral valve geometry. We build up our mitral valve geometry from mid-diastole when the valve is fully open, and select 20, see Figure.A.2.2 Step(3);

- *Time Series for LVOT:* Select "Enter Series for LVOT" to enter the series time for each LVOT slices. Each series time corresponds to a LVOT slice position. There are 13 in total, see Figure.A.2.2 Step(4);

- *Time Series for SA:* Select "Time Series for SA" to identify the short axis image information that we use to get papillary muscle attachment points,

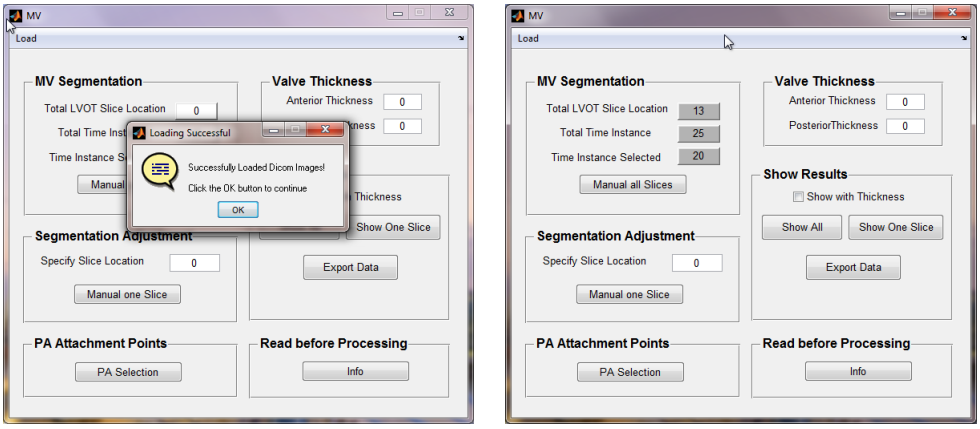

Step(7) Step(8)

Figure A.3.1: Step(7) Data preparation finished: A pop up dialogue showing "Successfully loaded Dicom Images!" will occur if data loading is finished. Step(8) Left click the MV segmentation area at up left of the GUI interface will show the number of total LVOT slice, total time instance and selected time instance for geometry construction.

see Figure.A.2.2 Step(5);

- *Load Images:* Select "Load Images" and wait until data loading be finished, see Figure.A.2.2 Step(6);

A.3 MV segmentation

The objective of the MV segmentation is the geometrical identification of the mitral sub-structures, including the annulus, the papillary muscle attachment points, the anterior and posterior leaflets. The GUI interface allow us to manually partitioned the anterior and posterior leaflet position slice-by-slice in a set of nodes in "MV Segmentation" and examine and modify specified segmentation in "Segmentation Adjustment" section.

- *Manual all Slices:* Select "Manual all Slice", the LVOT view of mitral valve

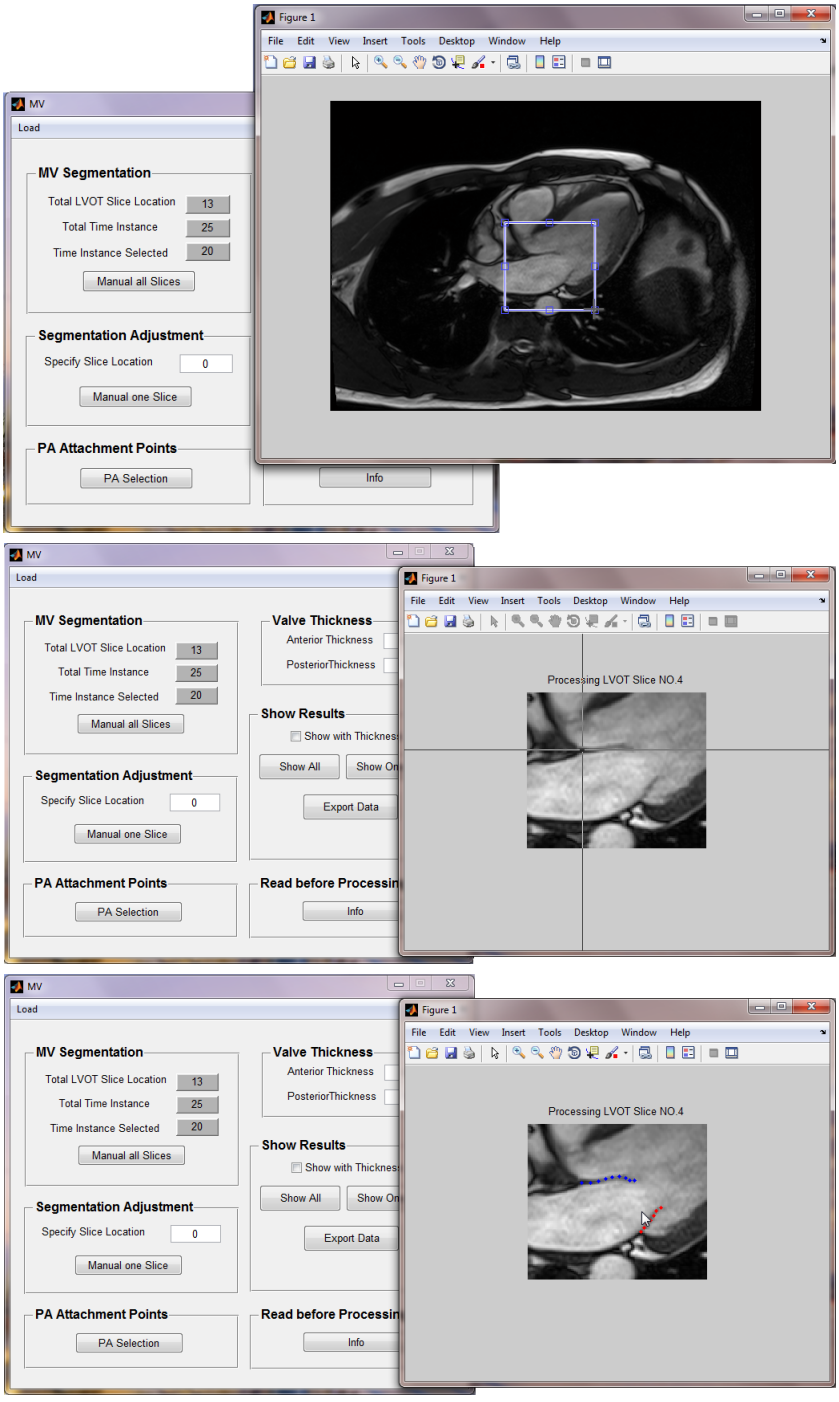

Figure A.3.2: Select "Manual all Slices": Step(9) Crop select an area including anterior leaflet and posterior leaflet in LVOT view; Step(10) Select the anterior and posterior landmarks from annulus position to leaflet free edge; Step(11) The selected anterior landmarks will shown in *blue* and selected posterior landmarks will shown in *red*.

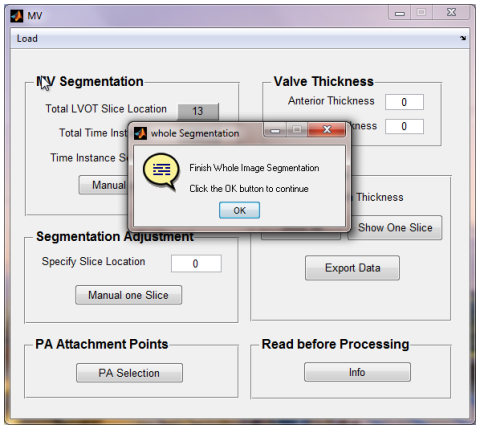

Step(12)

Figure A.3.3: Step(12) The pop up dialogue showing the MV segmentation completed.

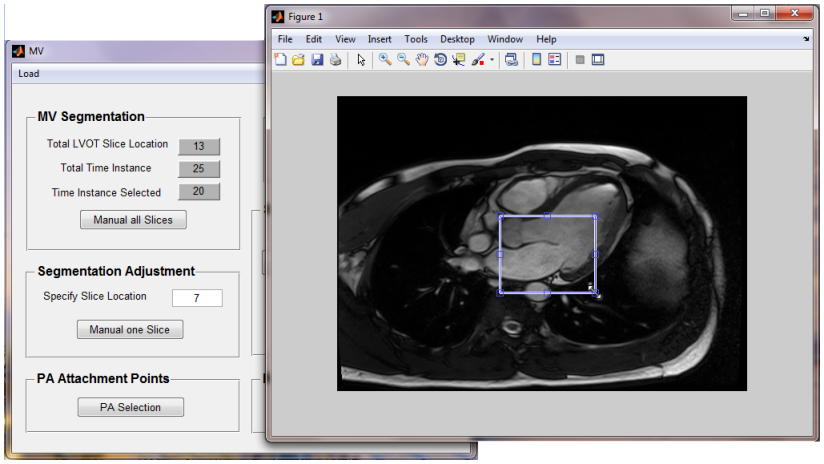

Step(13)

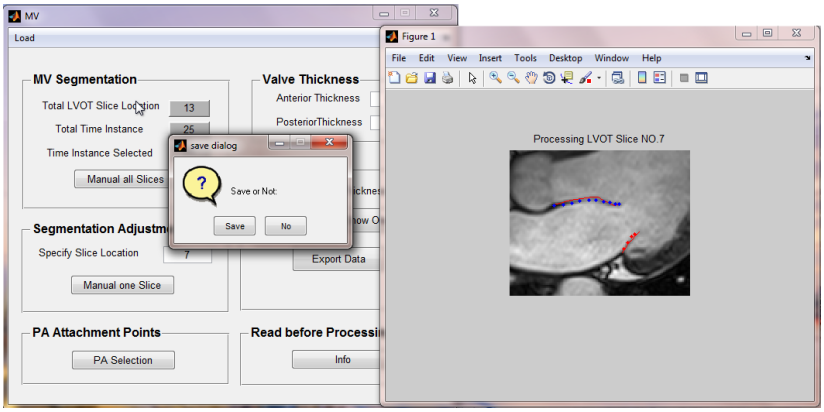

Step(14)

Figure A.3.4: Step(13) Specify the slice location number to examine and modify the segmentation for specified LVOT slice ; Step(14) Examine and modify the selected segmentation.

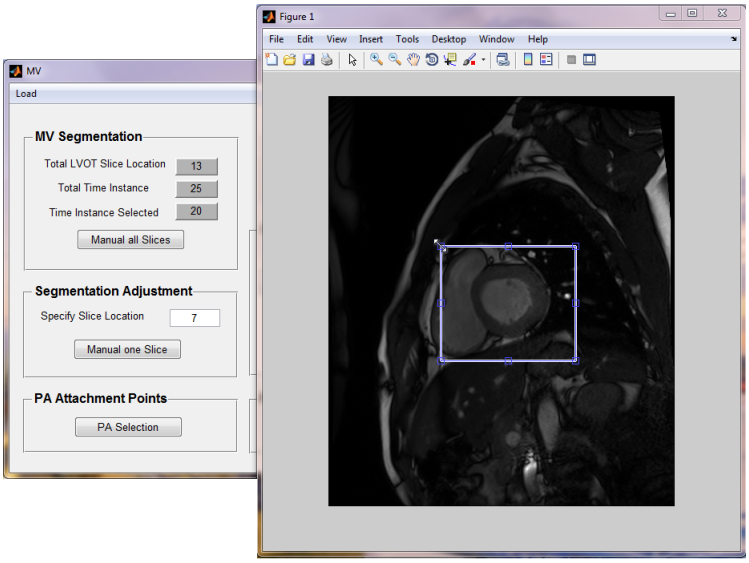

Step(15)

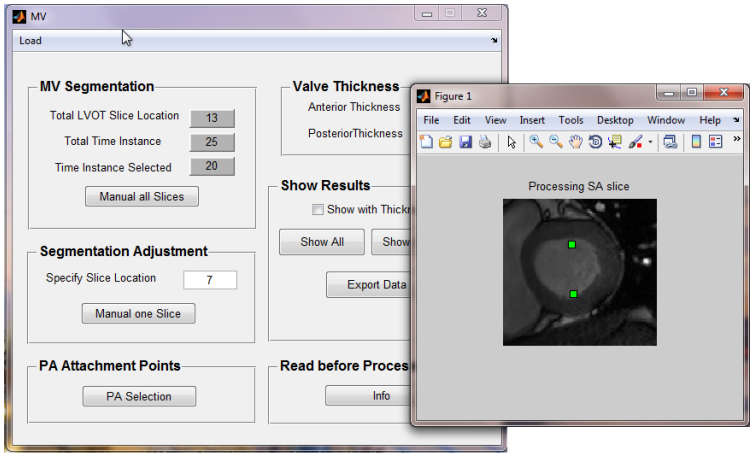

Step(16)

Figure A.3.5: Select "PA selection": Step(15) Crop select the area including left ventricle and double-click it to enlarge; Step(16) Select the papillary muscle attachment points (in *green square*) by left-click the mouse;

will appear. Use mouse to crop select an area including anterior leaflet and posterior leaflet as shown in Figure.A.3.2 Step(9). Double-click the centre of cropped area, the enlarged selected area will show and we can process with leaflet segmentation as shown in Figure.A.3.2 Step(10). Select the anterior landmarks from annulus position to leaflet free edge by left-click the mouse, and right-click the mouse to switch to posterior selection from posterior annulus to posterior leaflet tip. Then right-click the mouse to finish landmarks selection. The selected anterior landmarks will shown in *blue* and selected posterior landmarks will shown in *red*, see Figure.A.3.2 Step(11). Repeat above steps until all the anterior and posterior leaflet landmarks covering the whole mitral valve are selected, and a pop up dialogue showing segmentation completed, see Figure.A.3.3 Step(12).

- *Specify Slice Location:* Input the slice location number to examine and modify the segmentation for specified LVOT slice, see Figure.A.3.4 Step(13).

- *Manual one Slice:* The selected LVOT slice will show on the screen. Use mouse to crop select an area including anterior leaflet and posterior leaflet and double-click it. Then the previous segmentation will show with enlarged cropped area. If we want to modify it, then repeat Step(11). A save message dialog will appear to ask if you want to save the new segmentation, if choose "No" the new segmentation will not be saved, see Figure.A.3.4 Step(14).

- *PA Attachment Points:* Select "PA Selection" for identifying papillary muscle attachment points from short axis view which bisecting the left ventricle. Crop select the area including left ventricle and double-click it to enlarge (see Figure.A.3.5 Step(15)),and select the two papillary muscle attachment

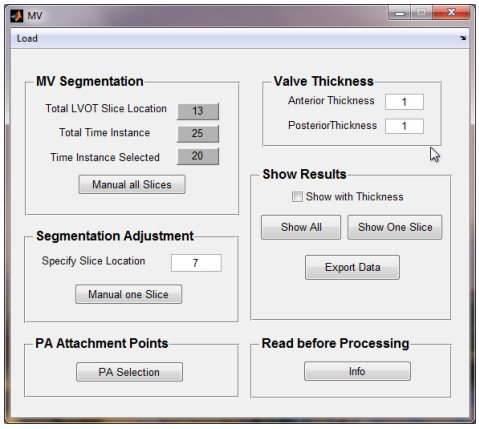

Step(17)

Figure A.3.6: Step(17) Identify the thickness for anterior leaflets and posterior leaflets. Herein we use 1 mm for both mitral leaflets.

points (see Figure.A.3.5 Step(16)) by mouse. The selected papillary muscle attachment points will shown in *green square*.

- *Valve Thickness:* Input the valve thickness for anterior and posterior leaflets; Herein we assume that both leaflets have identical thickness that is equal to 1 mm.

A.4 MV assembly

Finally, the mitral valve geometry is reconstructed and visualized in "Show Results". Annulus profile is reconstructed in all frames by interpolating the points detected on the leaflets-left ventricle wall boundary. Papillary muscle attachment points are identified as two single points, and their position are from short axis view bisecting left ventricle. Leaflets geometry are identified by spline the selected nodes from MV segmentation. Users can modify the leaflet thickness and visualize it by ticking "Show with Thickness".

- *Show All:* Tick "Show with Thickness" and select "Show All" , the anterior (in *blue*) , posterior leaflets (in *red*) with thickness identified in each LVOT slice and two papillary muscle attachment points will assembled and show by physical position, see Figure.A.4.1 Step(18). Un-tick "Show with Thickness" and select "Show All", the anterior (in *blue*), posterior (in *red*) and two papillary muscle attachment points will show together without thickness, see Figure.A.4.1 Step(19).

- *Show One Slice:* Tick "Show with Thickness" and select "Show One Slice", the anterior (in *blue*) and posterior leaflets (in *red*) with thickness in LVOT slice selected by "Specify Slice Location" will show with corresponding MR image, see Figure.A.4.1 Step(20). Un-tick "Show with Thickness" and select "Show One Slice", the anterior (in *blue*) and posterior (in *red*) without thickness will show with corresponding MR image, see Figure.A.4.1 Step(21) .

- *Export Data:* Write out the mitral valve geometry data in the format of SolidWorks macro data file.

A.5 Conclusion

The present work shows the process for patient-specific mitral valve geometry modelling through a GUI interface implementation developed based on MATLAB. This implementation also allows to shrink the time consumption for mitral valve geometry acquisition and potentially permits the access to any non expert user who don't have to acquire much knowledge in medical imaging segmentation.

Step(18)

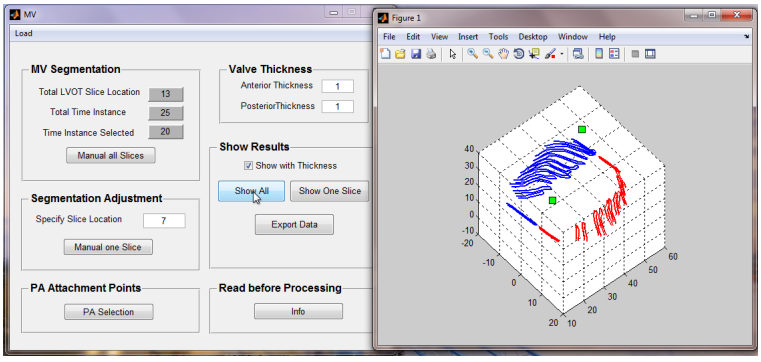

Step(19)

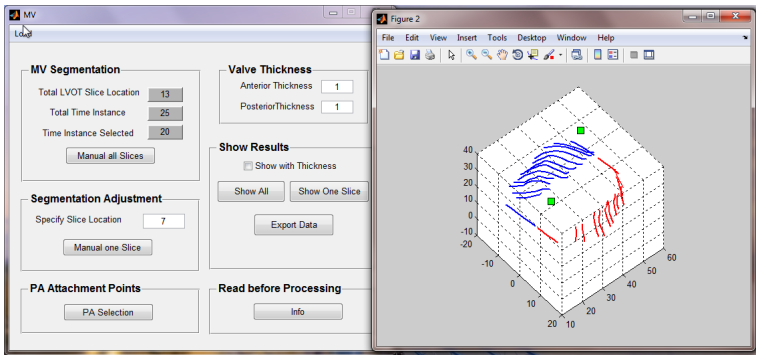

Step(20)

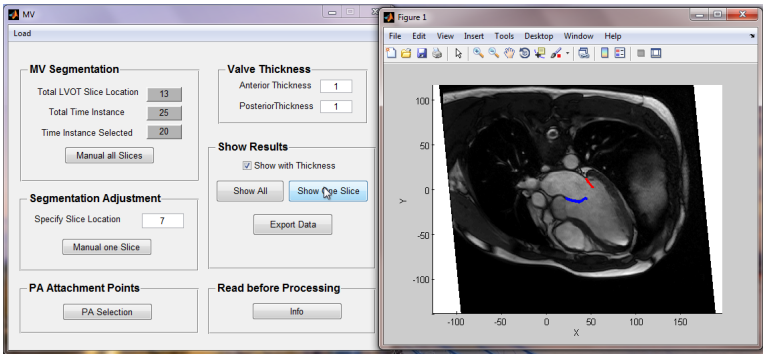

Step(21)

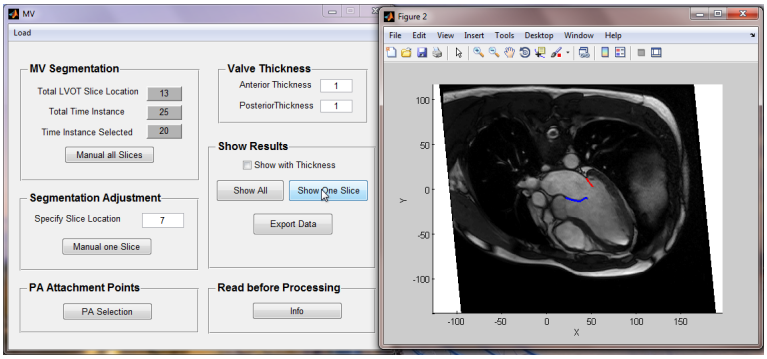

Figure A.4.1: "Show Results": Step(18) shows the anterior (in *blue*), posterior leaflets (in *red*) with thickness and two papillary muscle attachment points; Step(19) shows the anterior, posterior without thickness and two papillary muscle attachment points ; Step(20) shows the anterior and posterior leaflets with thickness in LVOT slice selected by "Specify Slice Location" with corresponding MR image; Step(21) shows the anterior and posterior without thickness with corresponding MR image

References

Khaled Alfakih, Scott Reid, Tim Jones, and Mohan Sivananthan. Assessment of ventricular function and mass by cardiac magnetic resonance imaging. *European radiology*, 14(10):1813–1822, 2004. 5

A Arnoldi, A Invernizzi, Raffaele Ponzini, E Votta, Enrico G Caiani, and Alberto Redaelli. Mitral valve models reconstructor: a python based gui software in a hpc environment for patient-specific fem structural analysis. In *Innovations and Advances in Computer Sciences and Engineering*, pages 215–219. Springer, 2010. 7, 9

Denis Berdajs and MarkoI. Turina. Mitral valve. In *Operative Anatomy of the Heart*, pages 289–356. Springer Berlin Heidelberg, 2011. ISBN 978-3-540-69227-0. doi: 10.1007/978-3-540-69229-4_6. URL http://dx.doi.org/10.1007/978-3-540-69229-4_6. vii, 2, 3

Daniele Boffi, Lucia Gastaldi, Luca Heltai, and Charles S Peskin. On the hyper-elastic formulation of the immersed boundary method. *Computer Methods in Applied Mechanics and Engineering*, 197(25):2210–2231, 2008. 11, 56, 78

Wolfgang Bothe, John-Peder Escobar Kvitting, Julia C Swanson, Sigurd Hartnett, Neil B Ingels Jr, and D Craig Miller. Effects of different annuloplasty

rings on anterior mitral leaflet dimensions. *The Journal of thoracic and cardiovascular surgery*, 139(5):1114–1122, 2010a. 5

Wolfgang Bothe, John-Peder Escobar Kvitting, Julia C Swanson, Serdar Göktepe, Kathy N Vo, Neil B Ingels, and D Craig Miller. How do annuloplasty rings affect mitral leaflet dynamic motion? *European Journal of Cardio-Thoracic Surgery*, 38(3):340–349, 2010b. 5

ZX Cai and XY Luo. A fluid–beam model for flow in a collapsible channel. *Journal of fluids and structures*, 17(1):125–146, 2003. 35

JA Casado, S Diego, D Ferreño, E Ruiz, I Carrascal, D Méndez, JM Revuelta, A Pontón, JM Icardo, and F Gutiérrez-Solana. Determination of the mechanical properties of normal and calcified human mitral chordae tendineae. *Journal of the Mechanical Behavior of Biomedical Materials*, 13:1–13, 2012. 90

R. E. Clark. Stress-strain characteristics of fresh and frozen human aortic and mitral leaflets and chordae tendineae. implications for clinical use. *Journal of Thoracic and Cardiovascular Surgery*, 66(2):202, 1973. 61

R. E. Clark and G. A. Butterworth. Characterization of the mechanics of human ortic and mitral valve leaflets. *Surgical Forum*, 22:134, 1971. 61

P. Colella and P. R. Woodward. The piecewise parabolic method (ppm) for gas-dynamical simulations. *Journal of Computational Physics*, 54(1):174–201, 1984. 19

F Dal Pan, G Donzella, C Fucci, and M Schreiber. Structural effects of an innova-

tive surgical technique to repair heart valve defects. *Journal of biomechanics*, 38(12):2460–2471, 2005. 7

D. R. Einstein, P. Reinhall, M. Nicosia, R. P. Cochran, and K. Kunzelman. Dynamic finite element implementation of nonlinear, anisotropic hyperelastic biological membranes. *Computer Methods in Biomechanics and Biomedical Engineering*, 6(1):33–44, 2003. 6, 60

D. R. Einstein, K. S. Kunzelman, P. G. Reinhall, M. A. Nicosia, and R. P. Cochran. Non-linear fluid-coupled computational model of the mitral valve. *Journal of Heart Valve Disease*, 14(3):376–385, 2005. 6, 60

Daniel R Einstein, Facundo Del Pin, Xiangmin Jiao, Andrew P Kuprat, James P Carson, Karyn S Kunzelman, Richard P Cochran, Julius M Guccione, and Mark B Ratcliffe. Fluid–structure interactions of the mitral valve and left heart: comprehensive strategies, past, present and future. *International Journal for Numerical Methods in Biomedical Engineering*, 26(3-4):348–380, 2010. 4, 8, 28

J Fisher, GR Jack, and DJ Wheatley. Design of a function test apparatus for prosthetic heart valves. initial results in the mitral position. *Clinical Physics and Physiological Measurement*, 7(1):63, 1986. ix, 43, 45

Frank A Flachskampf, Shalabh Chandra, Ajeetkumar Gaddipatti, Robert A Levine, Arthur E Weyman, Walter Ameling, Peter Hanrath, and James D Thomas. Analysis of shape and motion of the mitral annulus in subjects with and without cardiomyopathy by echocardiographic 3-dimensional reconstruction. *Journal of the American Society of Echocardiography*, 13(4):277–287, 2000. 9

V. Gabriel, O. Kamp, and C. A. Visser. Three-dimensional echocardiography in mitral valve disease. *European Journal of Echocardiography*, 6(6):443–454, 2005. 5, 60

D. N. Ghista and A. P. Rao. Structural mechanics of the mitral valve: stresses sustained by the valve; non-traumatic determination of the stiffness of the in vivo valve. *Journal of Biomechanics*, 5(3):295–296, 1972. 61

R. Gorlin and S. G. Gorlin. Hydraulic formula for calculation of the area of the stenotic mitral valve, other cardiac valves, and central circulatory shunts. *American Heart Journal*, 41(1):1–29, 1951a. 76

R Gorlin and SG Gorlin. Hydraulic formula for calculation of the area of the stenotic mitral valve, other cardiac valves, and central circulatory shunts. i. *American heart journal*, 41(1):1–29, 1951b. 54

G Randall Green, Paul Dagum, Julie R Glasson, George T Daughters, Ann F Bolger, Linda E Foppiano, Gerald J Berry, Neil B Ingels, and D Craig Miller. Mitral annular dilatation and papillary muscle dislocation without mitral regurgitation in sheep. *Circulation*, 100(suppl 2):II–95, 1999. 9

B. E. Griffith. Simulating the blood-muscle-valve mechanics of the heart by an adaptive and parallel version of the immersed boundary method. *PhD thesis*, 2005. 10, 29, 33, 107

B. E. Griffith. An accurate and efficient method for the incompressible Navier-Stokes equations using the projection method as a preconditioner. *Journal of Computational Physics*, 228(20):7565–7595, 2009. 16

B. E. Griffith. Immersed boundary model of aortic heart valve dynamics with physiological driving and loading conditions. *International Journal of Numerical Methods in Biomedical Engineering*, 28:317–345, 2012a. 10, 16, 18, 29, 46, 61, 69, 107

B. E. Griffith. On the volume conservation of the immersed boundary method. *Communications in Computational Physics*, 12:401–432, 2012b. 10, 15, 16, 29, 46, 61, 69, 107

B. E. Griffith and X. Luo. Hybrid finite difference/finite element version of the immersed boundary method. *(submitted)*, 2012. 11, 12, 25, 26, 56, 77, 103, 108

B. E. Griffith and C. S. Peskin. On the order of accuracy of the immersed boundary method: higher order convergence rates for sufficiently smooth problems. *Journal of Computational Physics*, 208(1):75–105, 2005. 33, 61

B. E. Griffith, X.Y. Luo, D. M. McQueen, and Peskin C.S. Simulating the fluid dynamics of natural and prosthetic heart valves using the immersed boundary method. *International Journal of Applied Mechanics*, 1(1):137–177, 2009. 10, 25, 29, 33, 41, 42, 46, 55, 59, 69, 101, 107

Boyce E Griffith, Richard D Hornung, David M McQueen, and Charles S Peskin. An adaptive, formally second order accurate version of the immersed boundary method. *Journal of Computational Physics*, 223(1):10–49, 2007. 33

P. E. Hammer, N. V. Vasilyev, D. P. Perrin, P. J. Del Nido, and R. D. Howe. Fast image-based model of mitral valve closure for surgical planning. *MIDAS Journal, Computational Biomechanics for Medicine (MICCAI 2008 Workshop)*, pages 15–26, 2008. 66

Gerhard A Holzapfel. Nonlinear solid mechanics: a continuum approach for engineering. 2000. 87

Somsupha Kanjanauthai. Mitral valve anatomy. vii, 3

Starr R Kaplan, Gerard Bashein, Florence H Sheehan, Malcolm E Legget, Brad Munt, Xiang-Ning Li, Murali Sivarajan, Edward L Bolson, Merrilinn Zeppa, M Archa, et al. Three-dimensional echocardiographic assessment of annular shape changes in the normal and regurgitant mitral valve. *American heart journal*, 139(3):378–387, 2000. 9

M. O. Karlsson, J. R. Glasson, A. F. Bolger, G. T. Daughters, M. Komeda, L. E. Foppiano, D. C. Miller, and N. B. Ingels Jr. Mitral valve opening in the ovine heart. *American Journal of Physiology-Heart and Circulatory Physiology*, 274 (2):H552–H563, 1998. 11, 73, 76, 108, 111

Hee Sun Kim. Nonlinear multi-scale anisotropic material and structural models for prosthetic and native aortic heart valves. 2009. 7

Hyunggun Kim, Krishnan B Chandran, Michael S Sacks, and Jia Lu. An experimentally derived stress resultant shell model for heart valve dynamic simulations. *Annals of biomedical engineering*, 35(1):30–44, 2007. 7

Hyunggun Kim, Jia Lu, Michael S Sacks, and Krishnan B Chandran. Dynamic simulation of bioprosthetic heart valves using a stress resultant shell model. *Annals of biomedical engineering*, 36(2):262–275, 2008. 7

Gaurav Krishnamurthy, Akinobu Itoh, Wolfgang Bothe, Julia C Swanson, Ellen Kuhl, Matts Karlsson, D Craig Miller, and Neil B Ingels Jr. Stress–strain

behavior of mitral valve leaflets in the beating ovine heart. *Journal of biomechanics*, 42(12):1909–1916, 2009. 7

K. S. Kunzelman, R. P. Cochran, C. Chuong, W. S. Ring, E. D. Verrier, and R. D. Eberhart. Finite element analysis of the mitral valve. *Journal of Heart Valve Disease*, 2(3):326–40, 1993. 2, 6, 60, 61, 65

K. S. Kunzelman, M. S. Reimink, and R. P. Cochran. Annular dilatation increases stress in the mitral valve and delays coaptation: a finite element computer model. *Cardiovascular Surgery*, 5(4):427–434, 1997. 6, 60, 66

K. S. Kunzelman, M. S. Reimink, and R. P. Cochran. Flexible versus rigid ring annuloplasty for mitral valve annular dilatation: a finite element model. *Journal of Heart Valve Disease*, 7(1):108–116, 1998. 6, 60

Karyn S Kunzelman and R. Cochran. Stress/strain characteristics of porcine mitral valve tissue: parallel versus perpendicular collagen orientation. *Journal of cardiac surgery*, 7(1):71–78, 1992. 8

J. P. E. Kvitting, W. Bothe, S. Gktepe, M. K. Rausch, J. C. Swanson, E. Kuhl, N. B. Ingels Jr, and D. C. Miller. Anterior mitral leaflet curvature during the cardiac cycle in the normal ovine heartclinical perspective. *Circulation*, 122 (17):1683–1689, 2010. 11, 73, 76, 108, 111

M. C. Lai and C. S. Peskin. An immersed boundary method with formal second-order accuracy and reduced numerical viscosity. *Journal of Computational Physics*, 160(2):705–719, 2000. 10, 29, 61, 107

K. D. Lau, V. Diaz, P. Scambler, and G. Burriesci. Mitral valve dynamics in structural and fluid-structure interaction models. *Medical Engineering & Physics*, 32(9):1057–1064, 2010. 6, 60, 80

J. R. Levick. *An Introduction to Cardiovascular Physiology 5E*. Hodder Education, 2012. 61, 66

Jun Liao and Ivan Vesely. A structural basis for the size-related mechanical properties of mitral valve chordae tendineae. *Journal of biomechanics*, 36(8): 1125–1133, 2003. 8

K. H. Lim, J. H. Yeo, and C. M. Duran. Three-dimensional asymmetrical modeling of the mitral valve: a finite element study with dynamic boundaries. *Journal of Heart Valve Disease*, 14(3):386–392, 2005. 6, 60, 61, 65

HF Liu, XY Luo, ZX Cai, and TJ Pedley. Sensitivity of unsteady collapsible channel flows to modelling assumptions. *Communications in Numerical Methods in Engineering*, 25(5):483–504, 2009a. 34

HF Liu, XY Luo, and ZX Cai. Stability and energy budget of pressure-driven collapsible channel flows. *Journal of Fluid Mechanics*, 705:348–370, 2012. 33

Wing Kam Liu, Yaling Liu, David Farrell, Lucy Zhang, X Sheldon Wang, Yoshio Fukui, Neelesh Patankar, Yongjie Zhang, Chandrajit Bajaj, Junghoon Lee, et al. Immersed finite element method and its applications to biological systems. *Computer Methods in Applied Mechanics and Engineering*, 195(13):1722–1749, 2006. 11, 56, 78

Yi Liu, Han Wen, Robert C Gorman, James J Pilla, Joseph H Gorman, Gerald

Buckberg, Shawn D Teague, and Ghassan S Kassab. Reconstruction of myocardial tissue motion and strain fields from displacement-encoded mr imaging. *American Journal of Physiology-Heart and Circulatory Physiology*, 297(3): H1151–H1162, 2009b. 105, 110

X. Y. Luo, W. G. Li, and J. Li. Geometrical stress-reducing factors in the anisotropic porcine heart valves. *Journal of Biomechanical Engineering*, 125: 735, 2003. 33

X. Y. Luo, B. E. Griffith, X. S. Ma, M. Yin, T. J. Wang, C. L. Liang, P. N. Watton, and G. M. Bernacca. Effect of bending rigidity in a dynamic model of a polyurethane prosthetic mitral valve. *Biomechanics and Modeling in Mechanobiology*, page (in press), 2012. vii, 10, 25, 27, 32, 61, 76, 101

XY Luo, ZX Cai, WG Li, and TJ Pedley. The cascade structure of linear instability in collapsible channel flows. *Journal of Fluid Mechanics*, 600(1):45–76, 2008. 29, 34

Xingshuang Ma, Hao Gao, Boyce E Griffith, Colin Berry, and Xiaoyu Luo. Image-based fluid-structure interaction model of the human mitral valve. *Computers & Fluids*, 2012. 9, 11, 12, 25, 79, 80, 82, 90, 96, 101, 104, 108, 109

Francesco Maisano, Alberto Redaelli, Monica Soncini, Emiliano Votta, Lorenzo Arcobasso, and Ottavio Alfieri. An annular prosthesis for the treatment of functional mitral regurgitation: Finite element model analysis of a dog bone–shaped ring prosthesis. *The Annals of thoracic surgery*, 79(4):1268–1275, 2005. 7

K. May-Newman and F. C. Yin. Biaxial mechanical behavior of excised porcine mitral valve leaflets. *American Journal of Physiology-Heart and Circulatory Physiology*, 269(4):H1319–H1327, 1995. 8, 87

K. May-Newman and F. C. P. Yin. A constitutive law for mitral valve tissue. *Journal of Biomechanical Engineering*, 120:38, 1998. 6, 8, 86, 87

P. C. McDonald, J. E. Wilson, S. McNeill, M. Gao, J. J. Spinelli, F. Rosenberg, H. Wiebe, and B. M. McManus. The challenge of defining normality for human mitral and aortic valves: geometrical and compositional analysis. *Cardiovascular Pathology*, 11(4):193–209, 2002. 11, 61, 65, 76, 108

G. E. Miller, J. F. Hunter, and W. M. Lively. A note on mitral valve mechanics: A pre-stressed leaflet concept. *Journal of Biomechanics*, 14(5):373–375, 1981. 65

H. Muresian. The clinical anatomy of the mitral valve. *Clinical Anatomy*, 22(1): 85–98, 2009. 2, 66

C. S. Peskin. The immersed boundary method. *Acta Numerica*, 11:479–517, 2002. 15, 17, 19, 24, 25, 101

Charles S Peskin. Numerical analysis of blood flow in the heart. *Journal of Computational Physics*, 25(3):220–252, 1977. 13

V. Prot and B. Skallerud. An improved transverse isotropic hyperelastic material model for simulation of mitral valve response. *Journal of Biomechanics*, 39: S618–S618, 2006. 6, 8, 9

V. Prot and B. Skallerud. Nonlinear solid finite element analysis of mitral valves with heterogeneous leaflet layers. *Computational Mechanics*, 43(3):353–368, 2009. 6, 9, 56

V. Prot, R. Haaverstad, and B. Skallerud. Finite element analysis of the mitral apparatus: annulus shape effect and chordal force distribution. *Biomechanics and Modeling in Mechanobiology*, 8(1):43–55, 2009. 6, 9, 56, 66

V. Prot, B. Skallerud, G. Sommer, and G. A. Holzapfel. On modelling and analysis of healthy and pathological human mitral valves: Two case studies. *Journal of the Mechanical Behavior of Biomedical Materials*, 3(2):167–177, 2010. 7, 9, 60

V. E. Prot, Haaverstad R., and Skallerud B. Modelling and numerical analysis of the porcine and human mitral apparatus. 2008. 7, 9

E Rapaport. Calculation of valve areas. *European heart journal*, 6(suppl C): 21–23, 1985. 54

M. S. Reimink, K. S. Kunzelman, and R. P. Cochran. The effect of chordal replacement suture length on function and stresses in repaired mitral valves: a finite element study. *Journal of Heart Valve Disease*, 5(4):365, 1996. 6

W. J. Rider, J. A. Greenough, and J. R. Kamm. Accurate monotonicity- and extrema-preserving methods through adaptive nonlinear hybridizations. *Journal of Computational Physics*, 225(2):1827–1848, 2007. 19

Jennifer Ritchie, Jorge Jimenez, Zhaoming He, Michael S Sacks, and Ajit P Yoganathan. The material properties of the native porcine mitral valve chordae

tendineae: an in vitro investigation. *Journal of biomechanics*, 39(6):1129–1135, 2006. 8

C.J Chuong M.S Sacks R.C Eberhart R.P.Cochran, K.S Kunzelman. Nondestructive analysis of mitral valve collagen fiber orientation. *ASAIO Trans*, 37: M447M448, 1991. 8

R. Ryan, S. Abbara, R. R. Colen, S. Arnous, M. Quinn, R. C. Cury, and J. D. Dodd. Cardiac valve disease: spectrum of findings on cardiac 64-mdct. *American Journal of Roentgenology*, 190(5):W294–W303, 2008. 11, 73, 76, 108, 111

Michael S Sacks, W David Merryman, and David E Schmidt. On the biomechanics of heart valve function. *Journal of biomechanics*, 42(12):1804–1824, 2009a. 8

Michael S Sacks, Frederick J Schoen, and John E Mayer Jr. Bioengineering challenges for heart valve tissue engineering. *Annual review of biomedical engineering*, 11:289–313, 2009b. 8

T. Sakai, Y. Okita, Y. Ueda, T. Tahata, H. Ogino, K. Matsuyama, and S. Miki. Distance between mitral anulus and papillary muscles: anatomic study in normal human hearts. *Journal of Thoracic and Cardiovascular Surgery*, 118(4): 636, 1999. 66

Ivan S Salgo, Joseph H Gorman, Robert C Gorman, Benjamin M Jackson, Frank W Bowen, Theodore Plappert, Martin G St John Sutton, and L Henry Edmunds. Effect of annular shape on leaflet curvature in reducing mitral leaflet stress. *Circulation*, 106(6):711–717, 2002. 9

B. Skallerud, V. Prot, and I. S. Nordrum. Modeling active muscle contraction

in mitral valve leaflets during systole: a first approach. *Biomechanics and Modeling in Mechanobiology*, 10(1):1–16, 2011. 7, 60

M. Stevanella, G. Krishnamurthy, E. Votta, J. C. Swanson, A. Redaelli, and N. B. Ingels Jr. Mitral leaflet modeling: Importance of in vivo shape and material properties. *Journal of Biomechanics*, 44(12):2229–2235, 2011a. 7

M. Stevanella, F. Maffessanti, C. A. Conti, E. Votta, A. Arnoldi, M. Lombardi, O. Parodi, E. G. Caiani, and A. Redaelli. Mitral valve patient-specific finite element modeling from cardiac mri: Application to an annuloplasty procedure. *Cardiovascular Engineering and Technology*, 2(2):66–76, 2011b. 7, 9, 69, 76

Frederick A Tibayan, Filiberto Rodriguez, Mary K Zasio, Lynn Bailey, David Liang, George T Daughters, Frank Langer, Neil B Ingels, and D Craig Miller. Geometric distortions of the mitral valvular-ventricular complex in chronic ischemic mitral regurgitation. *Circulation*, 108(10 suppl 1):II–116, 2003. 9

Sandeep Abhay Urankar. *Modeling surgical interventions in the mitral valve with the finite element method*. PhD thesis, University of Pittsburgh, 2009. 7

Wanpen Vongpatanasin, L David Hillis, and Richard A Lange. Prosthetic heart valves. *New England Journal of Medicine*, 335(6):407–416, 1996. 4, 28

E. Votta, F. Maisano, O. Alfieri, F. M. Montevecchi, and A. Redaelli. Finite element models of newly shaped prosthetic rings for the correction of functional mitral regurgitation. *Journal of Biomechanics*, 39:S293–S293, 2006. 7, 60

E. Votta, F. Maisano, S. F. Bolling, O. Alfieri, F. M. Montevecchi, and

A. Redaelli. The geoform disease-specific annuloplasty system: A finite element study. *Annals of Thoracic Surgery*, 84(1):92–101, 2007. 7, 60

E. Votta, E. Caiani, F. Veronesi, M. Soncini, F. M. Montevecchi, and A. Redaelli. Mitral valve finite-element modelling from ultrasound data: a pilot study for a new approach to understand mitral function and clinical scenarios. *Philosophical Transactions of the Royal Society A: Mathematical, Physical & Engineering Sciences*, 366:3411–3434, 2008. 7, 66

Qian Wang, Eric Sirois, and Wei Sun. Patient-specific modeling of biomechanical interaction in transcatheter aortic valve deployment. *Journal of biomechanics*, 45(11):1965–1971, 2012. 4, 5, 8, 9, 12, 79, 81, 88, 105, 108, 110

P. N. Watton, X. Y. Luo, X. Wang, G. M. Bernacca, P. Molloy, and D. J. Wheatley. Dynamic modelling of prosthetic chorded mitral valves using the immersed boundary method. *Journal of Biomechanics*, 40(3):613–626, 2007. 29, 31, 41, 42, 47, 55

P. N. Watton, X. Y. Luo, M. Yin, G. M. Bernacca, and D. J. Wheatley. Effect of ventricle motion on the dynamic behaviour of chorded mitral valves. *Journal of Fluids and Structures*, 24(1):58–74, 2008. 29, 41, 47, 55, 77

Eli Weinberg. *Dynamic simulation of heart mitral valve with transversely isotropic material model*. PhD thesis, Massachusetts Institute of Technology, 2005. 7

Eli J Weinberg and Mohammad R Kaazempur Mofrad. A finite shell element for heart mitral valve leaflet mechanics, with large deformations and 3d constitutive material model. *Journal of biomechanics*, 40(3):705–711, 2007. 7

Eli J Weinberg, Danial Shahmirzadi, and Mohammad Reza Kaazempur Mofrad. On the multiscale modeling of heart valve biomechanics in health and disease. *Biomechanics and modeling in mechanobiology*, 9(4):373–387, 2010. 8

Jonathan F Wenk, Zhihong Zhang, Guangming Cheng, Deepak Malhotra, Gabriel Acevedo-Bolton, Mike Burger, Takamaro Suzuki, David A Saloner, Arthur W Wallace, Julius M Guccione, et al. First finite element model of the left ventricle with mitral valve: insights into ischemic mitral regurgitation. *The Annals of thoracic surgery*, 89(5):1546–1553, 2010. 7

David John Wheatley, John Fisher, and David Williams. Heart valve prosthesis, January 9 2001. US Patent 6,171,335. ix, 41, 43, 45

M. Yin, X. Y. Luo, T. J. Wang, and P. N. Watton. Effects of flow vortex on a chorded mitral valve in the left ventricle. *International Journal for Numerical Methods in Biomedical Engineering*, 26(3-4):381–404, 2010. 29, 55, 77

Ajit P Yoganathan, KB Chandran, and Fotis Sotiropoulos. Flow in prosthetic heart valves: state-of-the-art and future directions. *Annals of biomedical engineering*, 33(12):1689–1694, 2005. 4

Casey Jones S. Yoganathan AP, He Z. Fluid mechanics of heart valves. *Annu Rev Biomed Eng.*, 6:331–62, 2004. 28

LT Zhang and M Gay. Immersed finite element method for fluid-structure interactions. *Journal of Fluids and Structures*, 23(6):839–857, 2007. 11, 56, 78

Lucy Zhang, Axel Gerstenberger, Xiaodong Wang, and Wing Kam Liu. Im-

mersed finite element method. *Computer Methods in Applied Mechanics and Engineering*, 193(21):2051–2067, 2004. 11, 56, 78